SPACECRAFT FORMATION KEEPING
NEAR THE LIBRATION POINTS OF THE SUN-EARTH/MOON SYSTEM

A Thesis

Submitted to the Faculty

of

Purdue University

by

Belinda G. Marchand

In Partial Fulfillment of the

Requirements for the Degree

of

Doctor of Philosophy

August 2004

Para Mami y Brenda.

ACKNOWLEDGMENTS

> “At times our own light goes out and is rekindled by a spark from another person. Each of us has cause to think with deep gratitude of those who have lighted the flame within us.” *Albert Schweitzer*

As always, I thank God for all the blessings in my life and for granting me the many opportunities I have enjoyed throughout my academic career. I would also like to express my eternal gratitude to my mother, God bless her soul, for all her love and support. Although she has been gone now for eight years, I have always felt her presence very strongly and she will always be my guiding light, my guardian angel. I also owe a large debt of gratitude to my sister, Brenda Marchand. Through thick and thin, she has always been there for me and, to this date, her strength of character leaves me speechless. I hope some day, either through action or eloquent speech, I can properly express my gratitude and my love for her.

As my advisor will testify, we are all a product of our environment. Although many have contributed building blocks to that environment, the foundation was laid by two very special individuals. Kathleen Howell, my advisor, is probably the single most influential person in my life. If I had to compile all I have learned from her in writing I could publish an encyclopedia. She is the most amazing human being I have ever had the pleasure of working and interacting with. I still can’t figure out how she finds time to do all she does, and also manage to do it so well. My respect and admiration for her as a professional and a human being has only grown stronger with each passing year. As I reach the finish line of this long academic marathon I also look back and remember fondly it was Brian Barden who metaphorically spoke those famous words, “on your marks, get set, go!”. He has always been a source of great inspiration for me and an amazing mentor and friend. Thank you for starting me on the right path.

Of course, I have to thank my family away from home, Linda Flack, Lisa Crain and Terri Moore. I am richer today for knowing all of them. Their friendship and support has helped me through the good and the bad times. I'd also like to extend my gratitude to my friends Jose Guzman and Chris Patterson, my partners in crime, who were always there to lend a helping hand at one time or another. I further extend my gratitude to my examining committee, Professors Martin Corless, Terrence Weisshaar, and Bill Crossley and to Professors James Longuski and Mario Rotea for their invaluable advice throughout the course of my degree.

Finally, I wish to thank those institutions and organizations that have provided funding for my graduate studies. Primary support was provided by the National Aeronautics and Space Administration, Contract Number NCC5-727 and NAG5-11839. In addition, throughout the course of my doctoral degree I have been partially funded by the Henry Luce Foundation, the Department of Aeronautics and Astronautics at Purdue University, the Bill and Melinda Gates Foundation, and the Zonta International Foundation.

TABLE OF CONTENTS

LIST OF TABLES

LIST OF FIGURES

ABSTRACT

Marchand, Belinda G. Ph.D., Purdue University, August, 2004. Spacecraft Formation Keeping Near the Libration Points of the Sun-Earth/Moon System . Major Professor: Kathleen C. Howell.

Multi-spacecraft formations, evolving near the vicinity of the libration points of the Sun-Earth/Moon system, have drawn increased interest for a variety of applications. This is particularly true for space based interferometry missions such as Terrestrial Planet Finder (TPF) and the Micro Arcsecond X-Ray Imaging Mission (MAXIM). Recent studies in formation flight have focused, primarily, on the control of formations that evolve in the immediate vicinity of the Earth. However, the unique dynamical structure near the libration points requires that the effectiveness and feasibility of these methods be re-examined.

The present study is divided into two main topics. First, a dynamical systems approach is employed to develop a better understanding of the natural uncontrolled formation dynamics in this region of space. The focus is formations that evolve near halo orbits and Lissajous trajectories, near the L_1 and L_2 libration points of the Sun-Earth/Moon system. This leads to the development of a Floquet controller designed to simplify the process of identifying naturally existing formations as well as the associated stable manifolds for deployment. The initial analysis is presented in the Circular Restricted Three-Body Problem, but the results are later transitioned into the more complete Ephemeris model.

The next subject of interest in this investigation is non-natural formations. That is, formations that are not consistent with the natural dynamical flow near the libration points. Mathematically, precise formation keeping of a given nominal configuration requires continuous control.

Hence, a detailed analysis is presented to contrast the effectiveness and issues associated with linear optimal control and feedback linearization methods. Of course, continuous operation of the thrusters, may not represent a feasible option for a particular mission. If discrete formation keeping is implemented, however, the formation keeping goal will be subject to increased tracking errors relative to the nominal path. With this in mind, the final phase of the analysis presented here is centered on discrete formation keeping. The initial analysis is devoted to both linear state and radial targeters. The results from these two methodologies are later employed as a starting solution for an optimal impulsive control algorithm.

1. Introduction

Multi-spacecraft formations are often considered within the context of distributed measurement systems. For instance, NASA's Earth Observing-1 and Landsat 7 [1] are two independent imaging satellites currently flying an extended mission to accomplish enhanced land imaging. An Air Force concept, TechSat 21 [2], considers clusters of small satellites whose goal is to enable multi-mission capabilities by reconfiguring the relative position of the vehicles formation. Artist renditions of both Earth Observing-1/Landsat 7 (EO-1/LS-7) and TechSat 21 are depicted in Figure 1.1.

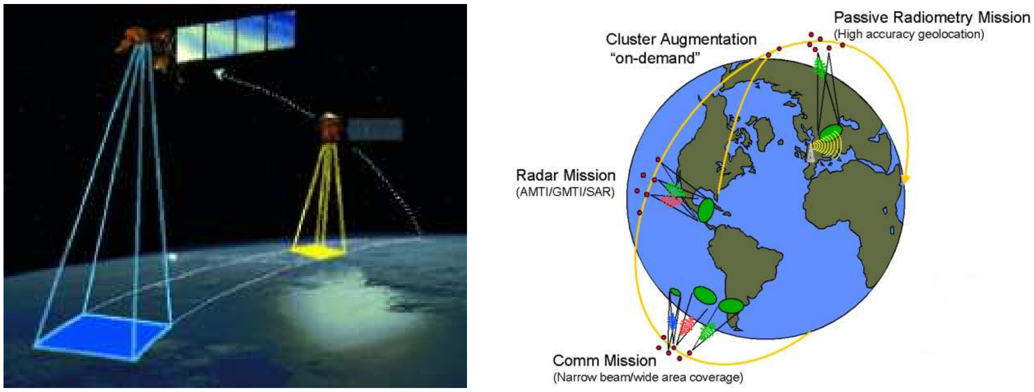

Figure 1.1. Examples of Near Earth Formations (EO-1/LS-7 and TechSat-21)

Another application of formation flight, one of particular interest in this study, is space based interferometry. Interferometry is the process of coupling two or more telescopes together to synthetically build an aperture equal to the separation of the telescopes. Today, interferometry relies on ground-based systems, such as the radio telescope array, or Very Large Array (VLA), in New Mexico and the Keck observatory in Hawaii, both illustrated in Figure 1.2. Naturally, the capabilities of ground based interferometers may be hindered by a number of sources that include, for instance, atmospheric distortions.

Figure 1.2. Ground Based Interferometers (VLA and Keck)

Removing these sources of error is one appealing aspect of space based interferometry. Furthermore, it is theorized that missions like TPF, MAXIM, and Stellar Imager, may offer resolutions greater than any single space based telescope could ever hope to achieve. That is because achieving such high resolutions requires a telescope that is physically enormous. Far greater in size than the Chandra X-Ray observatory ($> 10,000$ lbs), one of the largest vehicles ever launched into orbit. Aside from increased capabilities, a formation flight approach is potentially more cost effective in terms of launch requirements and upgrades. For instance, upgrading a space based interferometer may simply require phasing out individual vehicles in the formation.

The concept of formation flight is appealing for a variety of mission concepts, beyond space based interferometry. However, this particular application presents a number of unique technical challenges that must be addressed. The present study is focused on formation control for missions that evolve near the libration points of the Sun-Earth/Moon system. This includes the transfer into the nominal path and general formation keeping. The methods presented here do not include (a) the effects of modeling and measurement uncertainties or (b) relative attitude of the individual vehicles. The control methodologies developed are only concerned with maintaining the center of mass of each vehicle at the desired relative positions.

1.1 Previous Work

In this investigation, a formation of vehicles is characterized by one primary, or central, vehicle defined as the chief spacecraft. The remaining vehicles in the formation, then, are termed deputies. Within this context, "formation flight" is defined as a number of deputies that maintain a constant relative distance, and perhaps orientation, over extended periods of time relative to the chief spacecraft. Note that the chief spacecraft need not be an actual vehicle. It may also represent a generic reference point relative to which the deputy dynamics are measured.

In general, this type of dynamical configuration is not likely to exist as natural motion in either the two-body problem (2BP) or a multi-body regime. Much of the research to date refers to the control of constellations, clusters, and formations for Earth-orbiting missions [3–19] where the influence of other gravitational perturbations can be safely ignored. However, recent interest in formation flight near the L_1 and L_2 libration points of the Sun-Earth/Moon system requires an assessment of the effectiveness of the more commonly implemented control techniques.

The dynamical sensitivity that is characteristic of the region near the libration points associated with any three-body system, combined with the path constraints usually imposed on an envisioned configuration, makes formation keeping and deployment an interesting and challenging problem. Although some preliminary analyses have already been completed [20–34], a better understanding of natural and controlled formations in this region of space is still necessary. An added difficulty, inherent to this dynamical regime, is that no analytical solution for the reference path of a spacecraft exists. Although some approximations are available, any analysis involving formation flight in multi-body systems is still strongly dependent on numerical methods.

1.1.1 Near Earth Formations

In the 2BP, linear optimal control techniques, including linear quadratic regulators (LQR), are the most commonly encountered continuous controllers in the available literature on formation flight [3–12]. Many of these references reasonably assume that the formations are relatively small. Hence, the reference motion is modeled completely in terms of the linearized dynamics, as described by the Clohessy-Wiltshire equations in the 2BP. The controller is subsequently applied to the linear system but its effectiveness in the nonlinear model is often not explicitly demonstrated. Impulsive control schemes have also been implemented but are only applicable to formations that do not require constant tracking of a reference solution [13–15]. This approach is usually based on a Keplerian formulation of the two-body dynamics. Nonlinear methods, such as Lyapunov based control [16, 17] combined with adaptive control methods [18, 19] have also been successfully implemented for small formations in the two-body regime. Among these researchers, only de Queiroz et al. [18, 19] develop their control strategies based solely on the full nonlinear equations of motion.

1.1.2 Formations Near the Libration Points

Renewed interest in formations that evolve near the vicinity of the Sun-Earth/Moon libration points has inspired new studies regarding formation keeping in the three-body problem. Some of these investigations focus on the simplified circular restricted three-body problem (CR3BP) [20–22]. Scheeres and Vinh [20] develop a non-traditional yet innovative continuous controller, based on the local eigenstructure of the linear system, to achieve bounded motion near the vicinity of a halo orbit. Although the latter approach is not suitable for precise formation keeping, nor is it necessarily the optimal way of achieving boundedness, it does achieve other goals that may be more important for other types of missions.

In particular, the natural winding frequency of the spacecraft around the reference halo orbit is significantly increased. This is consistent with one of the stated requirements for TPF, where the formation is required to achieve a particular rotation rate that is not consistent with the natural dynamics near this region of space.

Other research efforts have also focused on the effectiveness of continuous control techniques in the general CR3BP, though not in the vicinity of the libration points. Gurfil and Kasdin consider both LQR techniques [21] and adaptive neural control [22] for formation keeping in the CR3BP. The second approach, described in [22], incorporates uncertainties introduced by modeling errors, inaccurate measurements, and external disturbances. Luquette and Sanner [35] apply adaptive nonlinear control to address the same sources of uncertainties in the nonlinear CR3BP. Formations modeled in the CR3BP do represent a good starting point. However, ultimately, any definitive formation keeping studies must be performed in the n-body EPHEM model, where the time invariance properties of the CR3BP are lost and, consequently, precisely periodic orbits do not exist near the libration points.

Hamilton [23] and Folta et al. [24] consider linear optimal control for formation flight relative to Lissajous trajectories, as determined in the EPHEM model. In their study, the evolution of the controlled formation is approximated from a linear dynamical model relative to the integrated reference orbit. Howell and Barden [25–28] also investigate formation flying near the vicinity of the libration points in the perturbed Sun-Earth/Moon system. A particularly unique aspect of their analysis is that it is performed in the full nonlinear EPHEM model. Initially, their focus is the determination of the natural behavior on the center manifold near the libration points and the first step of their study captures a naturally occurring six-satellite formation near L_1 or L_2 [25]. Further analysis considers strategies to maintain a planar formation of the six vehicles in an orbit about the Sun-Earth L_1 point [26–28], that is, controlling the deviations of each spacecraft relative to the initial formation plane. A discrete station keeping/control approach is devised to force the orientation of the formation plane to remain fixed inertially.

An alternate approach is also implemented by Gómez et al. [29] in a study of the deployment and station keeping requirements for the TPF nominal configuration. The latter analysis is initially performed in a simpler model but the simulation results are transitioned into the EPHEM model.

1.2 Scope of Present Work

In the present investigation, the effectiveness of conventional LQR techniques, as well as input and output feedback linearization (IFL and OFL) methods are applied to non-natural formations that evolve near the L_1 and L_2 collinear libration points of the Sun-Earh/Moon system. These three methods (LQR, IFL, and OFL) are successfully applied in both the simplified circular restricted three-body problem (CR3BP) and, ultimately, in the more complete n-body EPHEM model. Of course, continuous thruster operation may not always represent a feasible option. In such a case, the formation keeping task must rely on a discretized approach. The results of this investigation reveal that a state targeter approach can accomplish the goal to within a reasonable degree of accuracy, provided the nominal vehicle separations are on the order of meters. However, because these configurations are not consistent with the natural dynamics near the libration points, the error incurred between maneuvers grows rapidly as this nominal separation increases. This error is greatly reduced by implementing a radial targeter as an alternative. In this case, the impulsive control scheme targets the distance of the deputy relative to the chief, rather than the six elements of the state vector, at pre-specified times. This added dynamical flexibility reduces (a) the error incurred between maneuvers and (b) the need for frequent maneuvers in order to enforce the desired distance between the vehicles.

Although the mathematical implementation of continuous control laws is effective, the resulting control accelerations can be prohibitively small, depending on the desired configuration. For instance, near the libration points, formations that require the deputy vehicle to remain at a constant distance and orientation, relative to the chief spacecraft, are associated with thrust levels on the order of 0.81-3.21 nano-Newtons (nN), for a 10 meter separation and a 700 kg vehicle. Increasing the nominal separation by one order of magnitude also increases the cost by one order of magnitude. This indicates that a 10,000 km separation is required, for this type of formation, in order for the thrust level to exceed 1 micro-Newton (μN) of nominal thrust. The present state of propulsion technology allows for operational thrust levels on the order of 90-860 μN via pulsed plasma thrusters, such as those available for attitude control onboard Earth Observer-1 (EO-1) [36]. Increased interest in micro- and nano-satellites continues to motivate theoretical and experimental studies to further lower these thrust levels, as discussed by Mueller [37], Gonzalez [38] and Phipps [39]. Gonzalez [38] estimates that a lower bound of 0.3 nN is possible via laser induced ablation of aluminum. Aside from their immediate application to micro- and nano-satellite missions, these concepts are also potentially promising for formation flight near the libration points. However, the presently available technology may be sufficient to pursue other types of formation flight options. For instance, configurations that require the deputy vehicle to spin, relative to the chief, at some fixed rate, can quickly drive the thrust levels into the milli-Newton (mN) range.

Naturally, the science constraints on a particular mission may stipulate times when the thrusters cannot be in operation. With the understanding that highly precise formation keeping is not possible without at least nearly continuous control, the present study also considers two types of impulsive control. The first is a basic targeter approach that is, in concept, similar to that implemented by Howell and Barden [26–28] in the EPHEM model.

Also, the station keeping techniques previously implemented by Howell and Keeter [30] and Gómez et al. [31], based on a Floquet controller, are adapted here to the formation keeping problem. In particular, the Floquet controller is applied to study naturally existing formations near the libration points and the potential deployment into such configurations

This study is organized as follows:

- Chapter 2: In this chapter, the equations of motion of a spacecraft, as determined in the Circular Restricted Three-Body Problem (CR3BP) and the Ephemeris (EPHEM) model, are developed. These equations are then adapted for applications to formations near the libration points (L_i).
- Chapter 3: The natural formation dynamics near the libration points are carefully studied. The station keeping and deployment into these configurations is accomplished through the use of a modified Floquet controller. This chapter is dedicated to the development of the associated theory and the demonstration of its applications to formation flight.
- Chapter 4: Formation keeping, from the perspective of continuous control, is the subject of this chapter. The initial development is presented in the CR3BP. The dynamical symmetries that are characteristic of this mathematical model lead to a series of properties that are useful in simplifying the numerical implementation of this type of control in the CR3BP. Input and Output Feedback Linearization (IFL and OFL) techniques are also presented with applications to a set of sample configurations. The initial development is presented in the CR3BP although it is later transitioned into the EPHEM model.
- Chapter 5: As previously mentioned, a true formation flight mission may not allow for continuous thruster operation. In this section, a series of impulsive control techniques are presented, including a state targeter and a range targeter. Also, the theory associated with optimal nonlinear impulsive control is developed and implemented for a sample set of formations.

- Chapter 6: Some concluding remarks are presented to summarize the findings of this study. Also, future research topics, stemming from the results of the present investigation, are suggested.

2. Background

2.1 Dynamical Model

In the present investigation, two different representations are considered in modeling the dynamics of a spacecraft formation: the three-dimensional Circular Restricted Three-Body Problem (CR3BP) and the n-body Ephemeris model (EPHEM). Since no analytical solution is available in the n-body problem, for $n \geq 3$, any insight into the phase space must rely on numerical studies. In this respect, the CR3BP serves as a stepping stone on the path to a full n-body analysis. This simplified analysis enhances our understanding of the dynamical structure of the phase space, not only for one vehicle but also for the formation as a whole. Ultimately, however, any definitive mission analysis must be considered within the context of the EPHEM model.

2.1.1 Circular Restricted Three-Body Problem

In the CR3BP, the motion of a single spacecraft is influenced by the gravitational attraction of two primary bodies. The larger primary, in this investigation, is the Sun. The smaller primary, then, is the Earth/Moon barycenter (i.e., the center of mass). This is defined as the Sun-Earth/Moon (SEM) system. It is assumed that the mass of the vehicle is negligible compared to the two primaries. Hence, the primary motion is unaffected by the presence of the spacecraft. It is further assumed that the two primaries move in circular orbits about their common center of mass.

In the standard formulation of the CR3BP, the spacecraft state vector is defined in terms of a set of cartesian coordinates, relative to the synodic rotating frame. The origin of this frame is the barycenter of the system primaries. In the synodic frame, the x-axis is directed from the Sun towards the Earth/Moon barycenter.

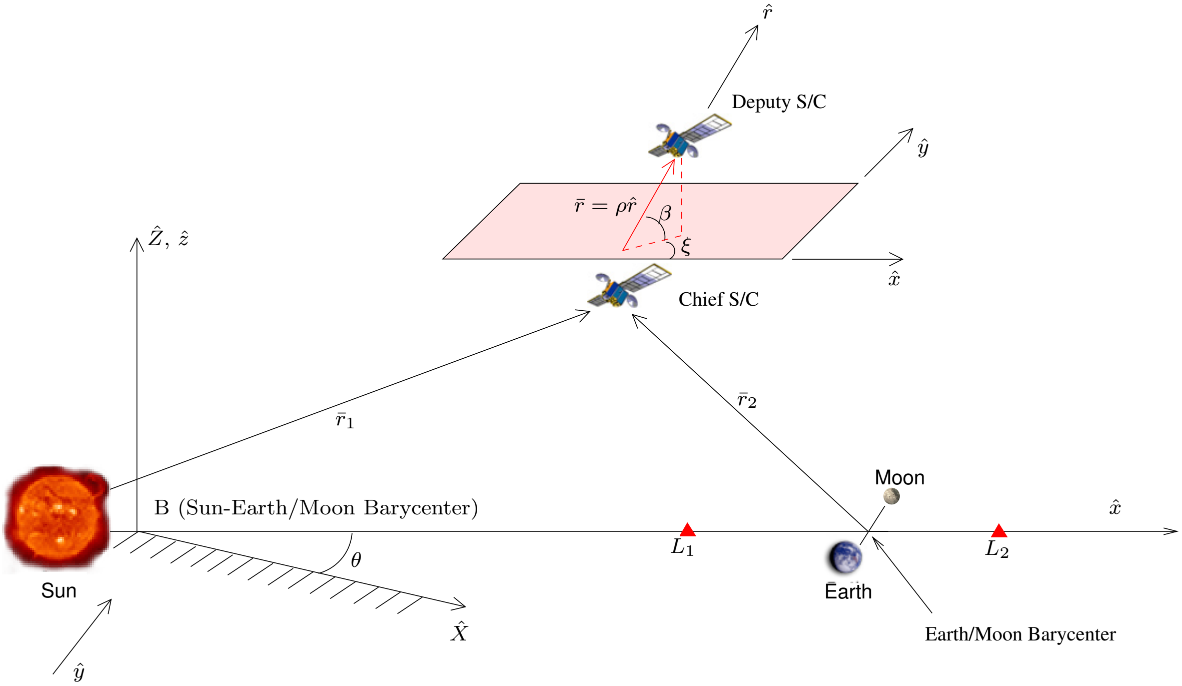

Figure 2.1. CR3BP Coordinate Frame Definitions

The z-axis is normal to the plane of motion of the primaries, and the y-axis completes the right-handed triad. A visual representation of these coordinate frame definitions is presented in Figure 2.1. In terms of synodic rotating coordinates, the non-dimensionalized equations of motion (EOMs) are determined as

$$\ddot{x}(t) = f_x(x(t), y(t), z(t)) + 2\dot{y}(t) + x(t) \ , \tag{2.1}$$

$$\ddot{y}(t) = f_y(x(t), y(t), z(t)) - 2\dot{x}(t) + y(t) \ , \tag{2.2}$$

$$\ddot{z}(t) = f_z(x(t), y(t), z(t)) \ , \tag{2.3}$$

where (x, y, z) denote the coordinates of the spacecraft relative to the barycenter B, and (f_x, f_y, f_z) represents the net gravitational force vector acting on the vehicle.

The force components are defined as

$$f_x(x,y,z) = -\frac{(1-\mu)}{r_1^3}(x+\mu) - \frac{\mu}{r_2^3}(x-1+\mu), \tag{2.4}$$

$$f_y(x,y,z) = -\left\{\frac{(1-\mu)}{r_1^3} + \frac{\mu}{r_2^3}\right\} y, \tag{2.5}$$

$$f_z(x,y,z) = -\left\{\frac{(1-\mu)}{r_1^3} + \frac{\mu}{r_2^3}\right\} z. \tag{2.6}$$

Note that r_1 and r_2 represent the radial distance from the spacecraft to the larger and smaller primary, respectively. The quantity μ is the non-dimensional mass parameter associated with the system. Let m_S, m_E, and m_M denote the mass of the Sun, Earth, and Moon, respectively. Then, the value of μ is determined as $\mu = (m_E + m_M)/(m_S + m_E + m_M)$. For the Sun-Earth/Moon system, $\mu \approx 3.0404 \times 10^{-6}$. The non-dimensionalization employed in deriving Equations (2.1)-(2.3) is based on a reference length, l^*, defined as the mean distance between the primaries. For the Sun-Earth/Moon system, $l^* \approx 149597927km = 1au$. The characteristic mass, m^*, is defined as the combined mass of the primaries, $m^* = m_S + (m_E + m_M)$. Finally, the characteristic time, t^*, is the inverse of the mean motion of the primaries, $t^* = (l^{*3}/(Gm^*))^{-1/2}$.

Particular Solutions in the CR3BP

Equations (2.1)-(2.3) admit many interesting types of solutions. Among these are five equilibrium points, L_1-L_5, termed libration points. These equilibrium points are defined in Figure 2.2 and exist only in the rotating frame of the primaries. Three of these points, L_1-L_3, are collinear with the primaries, P_1 and P_2. The remaining two, L_4-L_5 are termed the equilateral libration points because they exist at the vertices of equilateral triangles with the primaries. The examples presented throughout this study focus on orbits in the vicinity of L_1 and L_2, the equilibrium points closest to the smaller primary, P_2. In the CR3BP, P_2 represents the Earth/Moon barycenter. In the EPHEM model, P_2 denotes the Earth only.

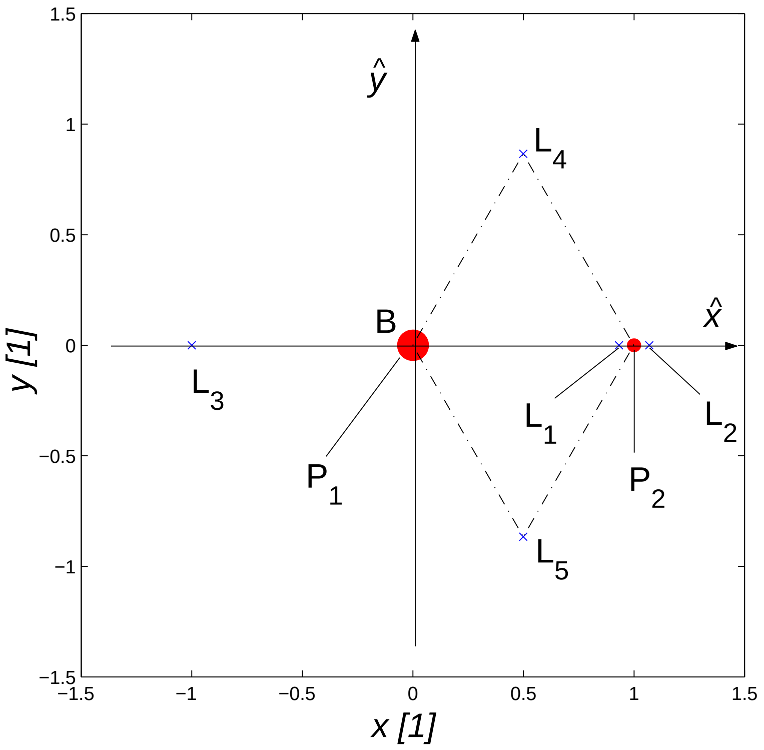

Figure 2.2. Libration Points

In the vicinity of the libration points, of the CR3BP, periodic halo orbits and quasi-periodic Lissajous trajectories are also known to exist. A sample halo orbit and also a Lissajous trajectory near the Sun-Earth/Moon L_1 point, as determined in the CR3BP, are plotted in Figures 2.3 and 2.4, respectively.

In the CR3BP, all solutions are symmetric about the xy-plane as well as the xz-plane. That is, if $\bar{x}(t) = [x(t), y(t), z(t), \dot{x}(t), \dot{y}(t), \dot{z}(t)]$ represents a solution to the equations of motion in Equations (2.1)-(2.3), then $\bar{x} = [x(t), y(t), -z(t), \dot{x}(t), \dot{y}(t), -\dot{z}(t)]$ also satisfies these equations. This xy-plane symmetry is easily verified, by inspection, from the equations of motion. The xz-plane symmetry originates from the time invariance that is characteristic of this mathematical model. In this case, if $\bar{x}(t) = [x(t), y(t), z(t), \dot{x}(t), \dot{y}(t), \dot{z}(t)]$ satisfies the nonlinear equations of motion then $\bar{x}(\tau) = [x(\tau), -y(\tau), z(\tau), -x'(\tau), y'(\tau), -z'(\tau)]$ also satisfies these equations.

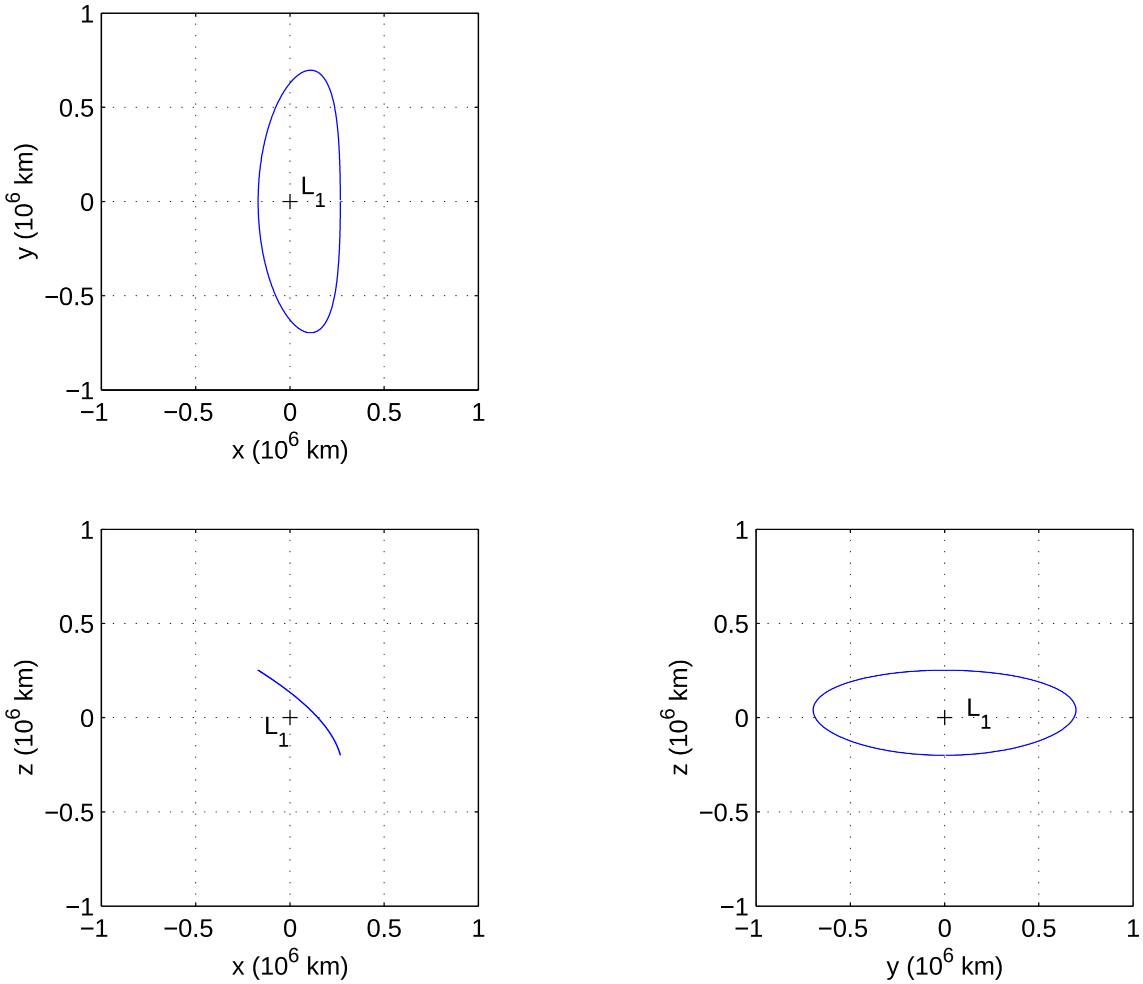

Figure 2.3. Periodic Halo Orbit Near the SEM L_1 Point (CR3BP)

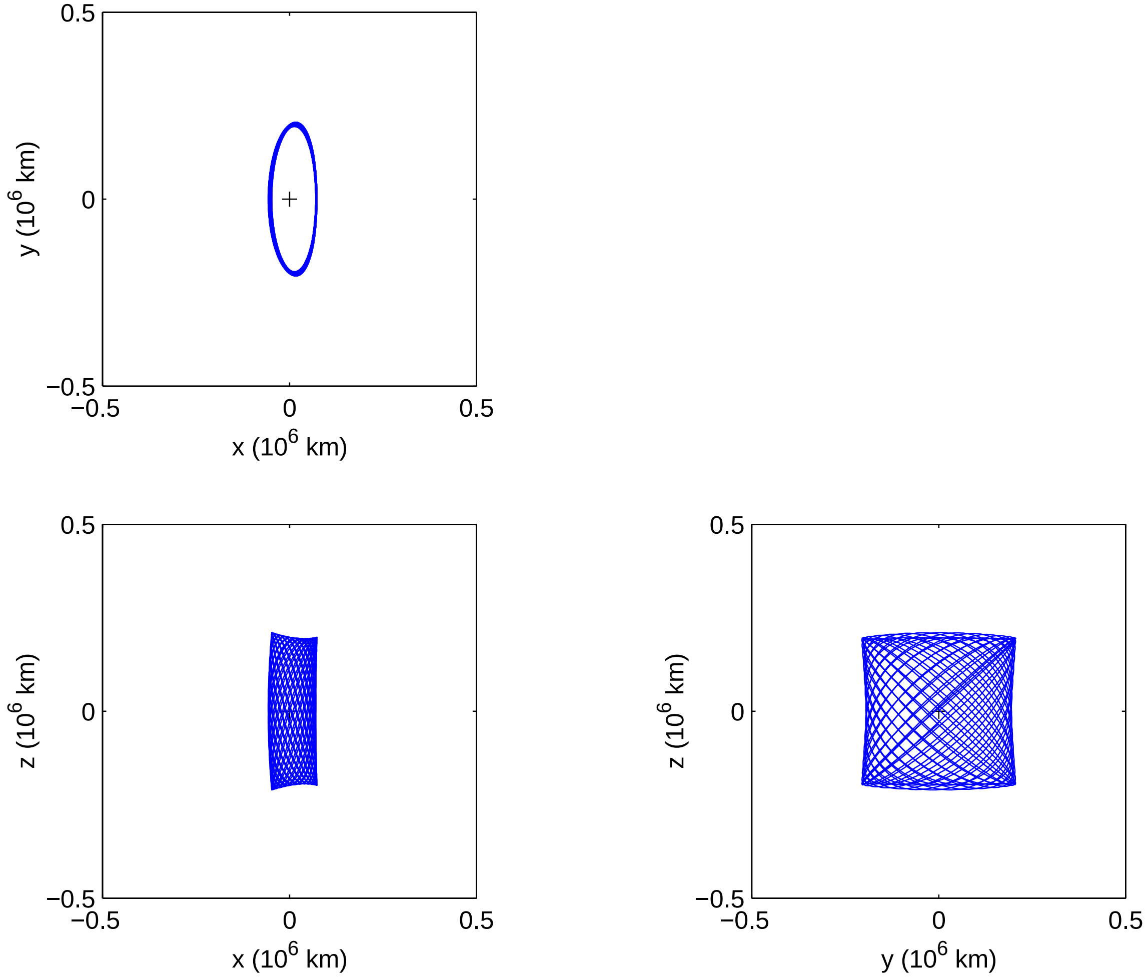

Figure 2.4. Quasi-periodic Lissajous Trajectory Near the SEM L_1 Point (CR3BP)

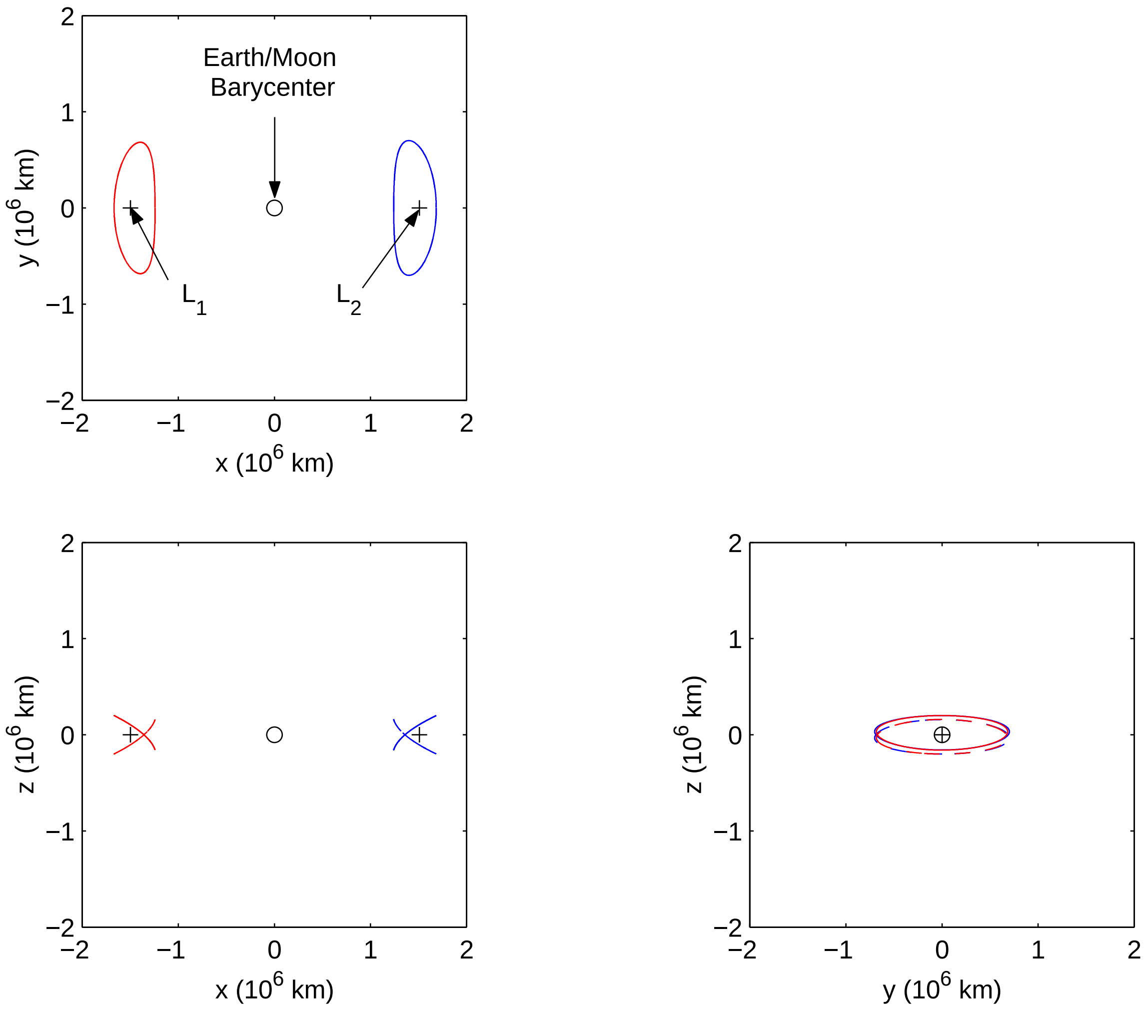

Figure 2.5. Symmetry of Periodic Halo Orbits

For this particular solution, $\tau = -t$ and the superscript " $'$ " implies differentiation with respect to τ. Halo orbits, for instance, are both symmetric about the plane of motion of the primaries, the xy-plane, and about the xz-plane. The xy-plane symmetry leads to the existence of "northern" and "southern" solutions, as demonstrated in Figure 2.5. For a halo orbit, a northern solution is one whose maximum out-of-plane excursion occurs above the xy-plane, in the $+z$-direction. Conversely, a southern orbit is one whose maximum out-of-plane amplitude is below the xy-plane.

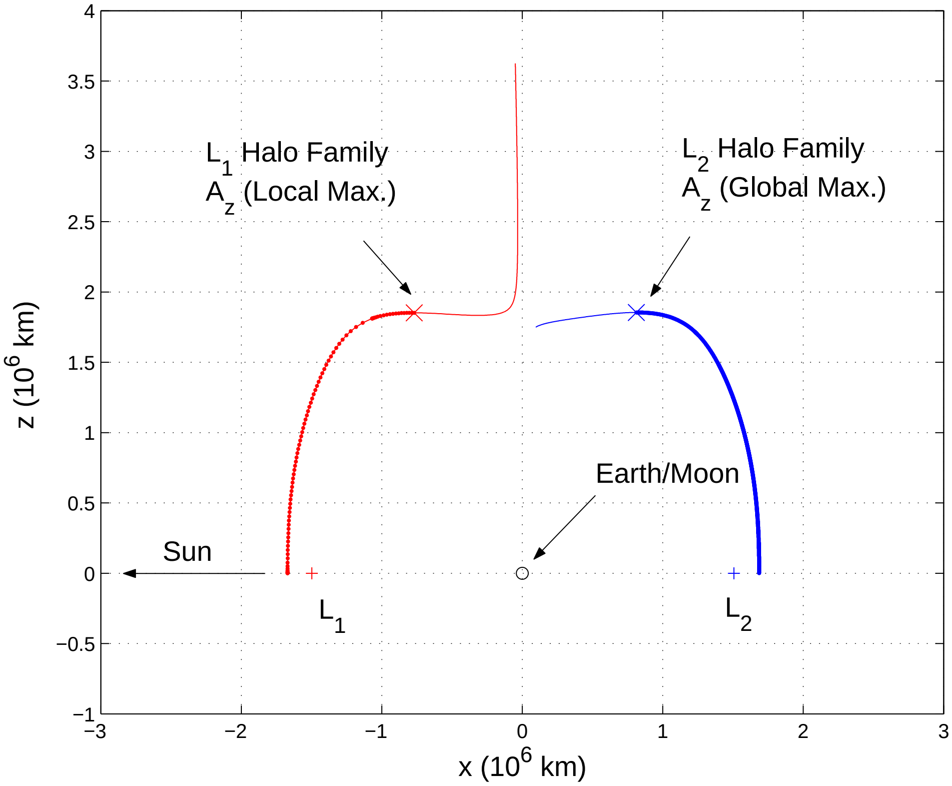

Figure 2.6. Hodographs that Describe the SEM Northern L_1 and L_2 Halo Families

In configuration space, three-dimensional halo orbits near the libration points exists along a surface. This surface defines a family of solutions. Since halo orbits are symmetric about the xz-plane, the surface that defines a particular halo family intersects the xz-plane twice, once above and once below the xy-plane. Each one of these intersections traces a line on the xz-plane defined as a hodograph. Figure 2.6 depicts the hodographs associated with the northern L_1 and L_2 halo families. Only the curves above the xy-plane are illustrated in this Figure. The red hodograph is associated with the northern L_1 halo family. The blue hodograph represents a significant portion of the northern L_2 halo family in the Sun-Earth/Moon system. Note, as both hodographs tend toward the Earth/Moon barycenter, P_2, the halo orbits approach rectilinear orbits. The L_1 hodograph increases in amplitude toward infinity. The blue hodograph sharply falls to zero amplitude.

Linearized System

The numerical implementation of a differential corrector relies on knowledge of the linearized dynamics. The linearization of Equations (2.1)-(2.3) is performed about a reference solution, $\bar{x}^{\circ}(t)$. Let $\delta\bar{x}(t) = \bar{x}(t) - \bar{x}^{\circ}(t)$ denote the state error relative to $\bar{x}^{\circ}$. This error can be approximated via a Taylor series expansion about $\bar{x}^{\circ}(t)$. A first order approximation results in variational equations described by

$$\delta\dot{\bar{x}}(t) = A(t)\delta\bar{x}(t). \tag{2.7}$$

In Equation (2.7), $A(t)$ is the 6×6 Jacobian matrix. The elements of $A(t)$ are time-varying and of the form,

$$A(t) = \begin{bmatrix} I_3 & 0_3 \\ \bar{f}_j & 2\Omega_3 \end{bmatrix} . \tag{2.8}$$

The submatrices I_k and 0_k, correspond to the $k \times k$ identity matrix and null matrix, respectively; thus, in Equation (2.8) both submatrices are 3×3. The elements of the submatrix $\bar{f}_j$ correspond to the partial derivatives of the force vector, $\bar{f} = [f_x, f_y, f_z]$, with respect to the j-th position element, $(x,\ y,\ z)$,

$$\bar{f}_j = \begin{bmatrix} \frac{\partial f_x}{\partial x} & \frac{\partial f_x}{\partial y} & \frac{\partial f_x}{\partial z} \\ \frac{\partial f_y}{\partial x} & \frac{\partial f_y}{\partial y} & \frac{\partial f_y}{\partial z} \\ \frac{\partial f_z}{\partial x} & \frac{\partial f_z}{\partial y} & \frac{\partial f_z}{\partial z} \end{bmatrix} . \tag{2.9}$$

The 3×3 constant submatrix Ω_3 is evaluated as

$$\Omega_3 = \begin{bmatrix} 0 & 1 & 0 \\ -1 & 0 & 0 \\ 0 & 0 & 0 \end{bmatrix} . \tag{2.10}$$

It is simple to verify that the solution to Equation (2.7) may be expressed in the form

$$\delta\bar{x}(t) = \Phi(t, t_0)\delta\bar{x}_0 \ , \tag{2.11}$$

where the vector $\delta\bar{x}_0 = \delta\bar{x}(t_0)$ is the initial state error relative to $\bar{x}^{\circ}(t)$, and $\Phi(t, t_0)$ denotes the state transition matrix. Clearly, at $t = t_0$, $\Phi(t_0, t_0) = I_6$.

Substitution of Equation (2.11) into Equation (2.7) leads to a set of 36 scalar differential equations that govern the elements of the 6×6 state transition matrix, $\Phi(t, t_0)$. These equations may be summarized, in matrix form, as

$$\dot{\Phi}(t, t_0) = A(t)\Phi(t, t_0) \ . \tag{2.12}$$

The matrix Equation (2.12), combined with the first order form of equations (2.1)-(2.3), comprise a set of 42 scalar, nonlinear, ordinary differential equations that must be solved simultaneously via a numerical integration scheme. Once the state transition matrix is available, over the desired length of time, the results may be used to drive a differential corrections process to identify a solution that meets the desired constraints.

Relative Formation Dynamics in the CR3BP

In studying the formation dynamics, as determined in the CR3BP, the motion of the chief spacecraft is modeled using Equations (2.1)-(2.3). The associated time-varying coordinates, relative to the barycenter, are defined as $(x_c(t), y_c(t), z_c(t))$. For the purposes of this investigation, the chief spacecraft is assumed to evolve along a natural arc. That is, no control input is required to maintain the desired path. It is further assumed that the chief vehicle evolves along a periodic halo orbit, similar to that in Figure 2.3, either near the L_1 or the L_2 point. The sample reference halo orbit selected for this study is characterized by an out-of-plane amplitude, A_z, of 2×10^5 km. Here, the A_z amplitude is defined as the distance from the xy-plane to the maximum out-of-plane excursion along the halo orbit.

For the deputy spacecraft, a more convenient choice of coordinates is one that describes the relative dynamics with respect to the chief. Although the choice of coordinates is clearly not unique, it can adversely influence the numerical analysis. For instance, the relative dynamics can be formulated in terms of spherical coordinates.

That is, the deputy spacecraft (S/C) position can be expressed in terms of radial distance to the chief S/C (ρ), azimuth of the chief-deputy line as measured in the plane of motion of the primaries (ξ), and elevation relative to the plane (β). These variables are pictorially defined in Figure 2.1. Although this formulation is adequate when dealing with the two-dimensional CR3BP, where $\beta = 0°$, it is plagued with modeling and numerical issues in the three-dimensional formulation.

In the spherical formulation, modeling difficulties are immediately apparent from the corresponding equations of motion. These are singular at $\beta = 90°$. Aside from this initial observation, the scale difference between the state variables (distance versus angular quantities) leads to numerical difficulties during the integration process if certain types of control – such as LQR – are incorporated into the model. In contrast, these difficulties are easily avoided by formulating the relative motion in terms of cartesian coordinates, $(x_d(t), y_d(t), z_d(t))$. These measure numbers, associated with the synodic rotating frame, are measured with respect to the chief spacecraft. The resulting relative equations of motion for the deputy spacecraft, subject to a control input $\bar{u}_{D_i}(t) = [a_x(t), a_y(t), a_z(t)]$, are determined as

$$\ddot{x}_d\left(t\right) = \Delta f_x\left(x_c, y_c, z_c, x_d, y_d, z_d\right) + 2\dot{y}_d\left(t\right) + x_d\left(t\right) + a_x\left(t\right), \tag{2.13}$$

$$\ddot{y}_d\left(t\right) = \Delta f_y\left(x_c, y_c, z_c, x_d, y_d, z_d\right) - 2\dot{x}_d\left(t\right) + y_d\left(t\right) + a_y\left(t\right), \tag{2.14}$$

$$\ddot{z}_d\left(t\right) = \Delta f_z\left(x_c, y_c, z_c, x_d, y_d, z_d\right) + a_z\left(t\right). \tag{2.15}$$

Equations (2.13)-(2.15) may also be summarized, in vector form, as

$$\ddot{\bar{r}}(t) = \Delta\bar{f}\left(\bar{r}(t), \dot{\bar{r}}(t)\right) + \bar{u}_{D_i}(t), \tag{2.16}$$

where $\bar{r} = (x_d, y_d, z_d)$ and $\dot{\bar{r}} = (\dot{x}_d, \dot{y}_d, \dot{z}_d)$. The differential gravitational forces in Equations (2.13)-(2.15), or the components of $\Delta\bar{f}(\bar{r}, \dot{\bar{r}})$ in Equation (2.16), are represented

$$\begin{aligned} \Delta f_x &= f_x\left(x_c + x_d, y_c + y_d, z_c + z_d\right) - f_x\left(x_c, y_c, z_c\right), \\ \Delta f_y &= f_y\left(x_c + x_d, y_c + y_d, z_c + z_d\right) - f_y\left(x_c, y_c, z_c\right), \\ \Delta f_z &= f_z\left(x_c + x_d, y_c + y_d, z_c + z_d\right) - f_z\left(x_c, y_c, z_c\right). \end{aligned} \tag{2.17}$$

Note that, in Equations (2.13)-(2.15), it is assumed that the chief spacecraft evolves along a natural solution. If such is not the case, these equations are easily adapted simply by replacing $\bar{u}_{D_i}(t)$ with $\bar{u}_{D_i}(t) - \bar{u}_C(t)$.

Depending on the type of control applied, it may be more convenient to formulate the dynamical evolution of the deputy in terms of a set of error equations. For instance, if the desired nominal state and the associated nominal control input are pre-specified, then the equations of motion can be expressed in terms of the error relative to this nominal path such that

$$\begin{aligned}
\ddot{e}_x\left(t\right) &= \left(\Delta f_x - \Delta f_x^\circ\right) + 2\dot{e}_y\left(t\right) + e_x\left(t\right) + \left(a_x - a_x^\circ\right), \\
\ddot{e}_y\left(t\right) &= \left(\Delta f_y - \Delta f_y^\circ\right) - 2\dot{e}_x\left(t\right) + e_y\left(t\right) + \left(a_y - a_y^\circ\right), \\
\ddot{e}_z\left(t\right) &= \left(\Delta f_z - \Delta f_z^\circ\right) + \left(a_z - a_z^\circ\right),
\end{aligned} \tag{2.18}$$

where the superscript "o" implies evaluation along the nominal path of the deputy.

Linearized Formation Dynamics in the CR3BP

In terms of the relative dynamics of the deputy spacecraft, consider a general time-varying reference solution defined by the state vector $\bar{x}_d(t)^\circ$ and a nominal control input $\bar{u}_d(t)^\circ$. Relative to this nominal solution, the linearized dynamics associated with Equations (2.13)-(2.15) are represented by a first order system of the form

$$\delta\dot{\bar{x}}_d\left(t\right) = A_d\left(t\right)\delta\bar{x}_d\left(t\right) + B\left(t\right)\delta\bar{u}_d\left(t\right), \tag{2.19}$$

where $\delta\bar{x}_d(t) = \bar{x}_d(t) - \bar{x}_d(t)^\circ$ denotes the perturbed state relative to $\bar{x}_d(t)^\circ$ and $\delta\bar{u}_d(t) = \bar{u}_d(t) - \bar{u}_d(t)^\circ$ is the differential control input.

The time varying Jacobian, $A_d\left(t\right)$, is evaluated along the reference solution, $\bar{x}_d\left(t\right)^{\circ}$, that defines the desired nominal configuration and is of the form

$$A_d\left(t\right) = \begin{bmatrix} 0 & 0 & 0 & 1 & 0 & 0 \\ 0 & 0 & 0 & 0 & 1 & 0 \\ 0 & 0 & 0 & 0 & 0 & 1 \\ \frac{\partial \Delta f_x}{\partial x_d} + 1 & \frac{\partial \Delta f_x}{\partial y_d} & \frac{\partial \Delta f_x}{\partial z_d} & 0 & 2 & 0 \\ \frac{\partial \Delta f_y}{\partial x_d} & \frac{\partial \Delta f_y}{\partial y_d} + 1 & \frac{\partial \Delta f_y}{\partial z_d} & -2 & 0 & 0 \\ \frac{\partial \Delta f_z}{\partial x_d} & \frac{\partial \Delta f_z}{\partial y_d} & \frac{\partial \Delta f_z}{\partial z_d} & 0 & 0 & 0 \end{bmatrix}. \tag{2.20}$$

The 6×3 matrix $B\left(t\right)$ is, in this case, constant and defined as $B = \begin{bmatrix} 0_3 & I_3 \end{bmatrix}^T$. Note that, even if the desired nominal motion is constant, the matrix $A_d\left(t\right)$ is time-varying because the partial derivative terms in Equation (2.20) depend explicitly on $\bar{x}_c(t)$, the state of the chief S/C.

2.1.2 Ephemeris Model

In the ephemeris (EPHEM) model, the standard form of the relative equations of motion for the n-body problem, as formulated in the inertial frame ($\hat{X}$, $\hat{Y}$, $\hat{Z}$), is employed. Hence, the dynamical evolution of each vehicle in the formation is governed by

$${}^{I}\ddot{\bar{r}}^{P_2P_s} = -\frac{\mu_q}{\left(r^{P_2P_s}\right)^3} + \sum_{j=1,j\neq 2,s}^{N} \mu_j \left(\frac{\bar{r}^{P_sP_j}}{\left(r^{P_sP_j}\right)^3} - \frac{\bar{r}^{P_2P_j}}{\left(r^{P_2P_j}\right)^3}\right) + \bar{f}_{per}^{(P_s)} = \bar{f}_{grav}^{(P_s)} + \bar{f}_{per}^{(P_s)}. \tag{2.21}$$

A graphical representation of the formulation for the equations of motion is illustrated in Figure 2.7. For notational purposes, let P_2 denote the central body of integration, in this case, the Earth. Then, P_s represents the spacecraft, and the sum over j symbolizes the presence of other gravitational perturbations. For the purposes of this analysis, the Sun and the Moon represent the perturbing gravity fields acting on the spacecraft. Other bodies can be added if they are relevant to the analysis. The term $\bar{f}_{per}^{P_s}$ is included to incorporate any non-gravitational external forces that may act upon P_s.

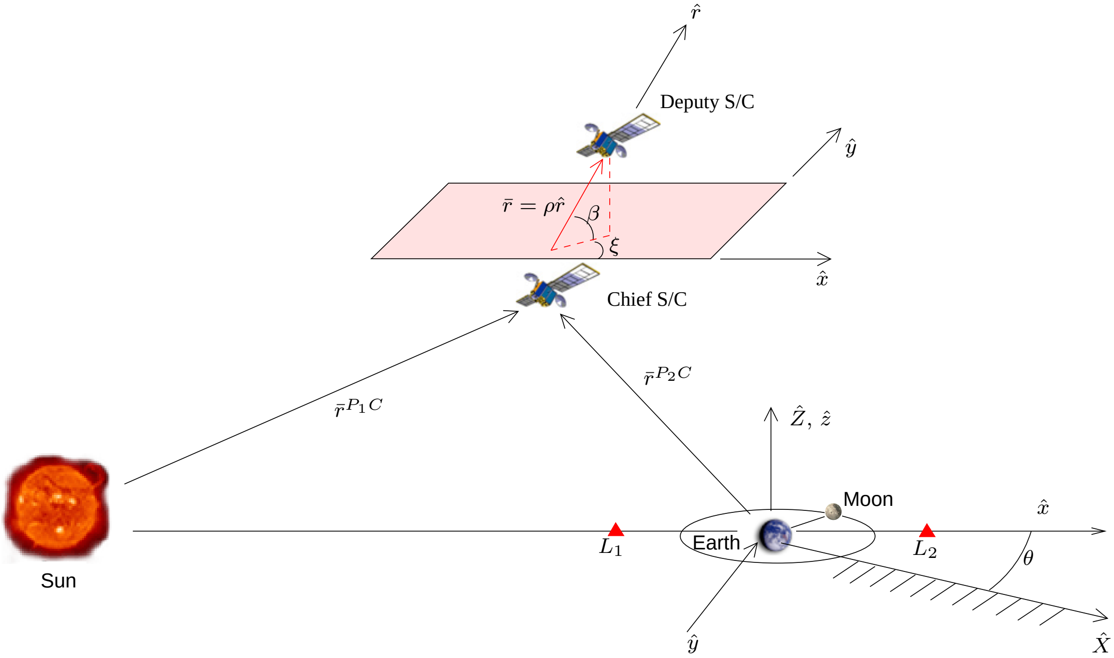

Figure 2.7. Coordinate Frame Definitions

Since the focus of this research is formations that evolve near the libration points of the Sun-Earth/Moon system, it is appropriate to introduce an alternate rotating frame in which the solutions to Equation (2.21) are best visualized. In the EPHEM model, the P_1-P_2 rotating frame (P1P2ROT), as seen in Figure 2.7, is defined by unit vectors $\hat{x}$, $\hat{y}$ and $\hat{z}$. The line directed from the Sun to the Earth is defined as the x-axis. The y-axis is parallel to the instantaneous direction of motion of the Earth. Finally, the z-axis is normal to the instantaneous plane of motion of the primaries.

The P_1-P_2 rotating frame is not the same as that defined in Figure 2.1, where the x-axis is directed towards the Earth/Moon barycenter. In the EPHEM model, the P_1-P_2 rotating frame is determined at each instant of time based on the ephemeris information available for the Earth. Although it is possible to transform the inertial state of the deputy into the frame defined in Figure 2.1, doing so requires some additional computations.

In the CR3BP, the libration points are fixed in the rotating frame of the primaries (P1P2ROT). However, in the CR3BP, the primaries are the Sun (P_1) and the Earth/Moon barycenter (P_2). In the EPHEM model, the primaries are the Sun (P_1) and the Earth (P_2), as perturbed by the Moon. Hence, the libration point is not fixed in the P_1-P_2 rotating frame. The only frame in which the instantaneous libration point "appears" fixed is one that is centered at the libration point. In this case, the rotating x-axis is directed from P_1 to the barycenter of the Earth/Moon system. Since the distance from the Sun to the Earth/Moon barycenter varies with time, the libration point further oscillates along the rotating x-axis. Clearly, determination of this rotating frame requires that the barycenter of the Earth/Moon system be computed at each instant of time from ephemeris information, such that the corresponding location of the instantaneous libration point can be identified. This coordinate frame is termed the rotating libration point (RLP) frame. Note that, if the moon is not present, the unit vectors that define the P1P2ROT frame and the RLP frame are always aligned, though the origin of each frame is different.

Particular Solutions in the EPHEM Model

Periodic solutions do not exist in the EPHEM model, only quasi-periodic Lissajous trajectories exist near the instantaneous libration points in this case. In general, since no analytical solution is available in either the CR3BP or the EPHEM model, the identification of periodic and quasi-periodic solutions depends on iterative procedures, such as the two-level differential corrector developed by Howell and Pernicka [40]. These algorithms are not self-starting since they require an initial approximation of the solution. For example, in both the CR3BP and EPHEM models, an initial guess may be obtained from analytical approximations, such as those developed by Richardson [41, 42] and Cary [42]. A sample solution, obtained from this approach, is plotted in Figure 2.8.

Table 2.1. SRP Parameters for TPF Combiner S/C

k	1.4	c	$299792.458\ km/sec$	$A_{s/c}$	$4.9087 \times 10^{-4}\ km^2$
S_0	$1.358 \times 10^3\ W/m^2$	D_0	$1.49597870 \times 10^8\ km$	m_s	$700\ kg$

As an alternative, a numerical solution previously identified in the CR3BP can be "transitioned" into the EPHEM model by selecting a discrete series of states along the path and using them as an initial guess to the two-level corrector [40] in the EPHEM model. A sample implementation of this approach is computed and appears in Figure 2.9. This particular type of solution is termed a "halo"-like Lissajous, or Liss, in the EPHEM model.

Solar Radiation Pressure Modeling

The effects of solar radiation pressure (SRP) are incorporated into the EPHEM model through the perturbing force term $\bar{f}_{per}^{P_s}$. The SRP force vector, as discussed by McInnes [43], can be modeled as

$$\bar{f}_{srp}^{(P_s)} = \frac{kS_0A_{s/c}}{m_s c}\left(\frac{D_0^2}{d^2}\right)\cos^2(\beta_{srp})\hat{n}, \tag{2.22}$$

where k denotes the absorptivity of the spacecraft surface ($k = 2$ for a perfectly reflective surface), S_0 is the energy flux measured at the Earth's distance from the Sun [W/m^2], D_0 is the mean Sun-Earth distance [km], $A_{s/c}$ represents the constant spacecraft effective cross sectional area [km^2], c is the speed of light [km/sec], m_s is the spacecraft mass [kg], β_{srp} is the angle of incidence of the incoming photons, $\hat{n}$ denotes the unit surface normal, and d [km] represents the Sun-spacecraft distance. The sample spacecraft implemented in this study is modeled after the TPF combiner spacecraft, assuming a 25 meter diameter and a spacecraft mass of 700 kg. The SRP force parameters are summarized in Table 2.1.

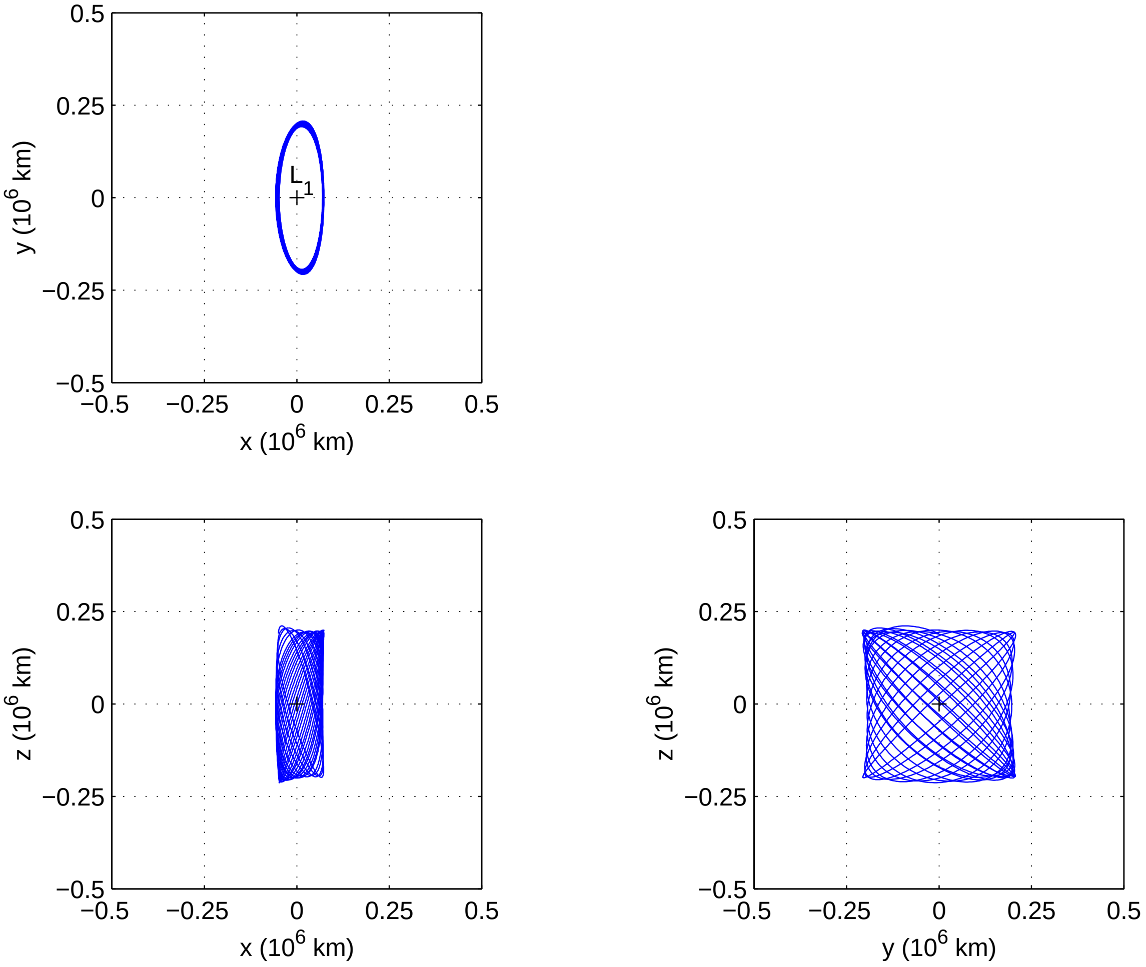

Figure 2.8. Lisssajous Trajectory Near the SEM L_1 Point (EPHEM)

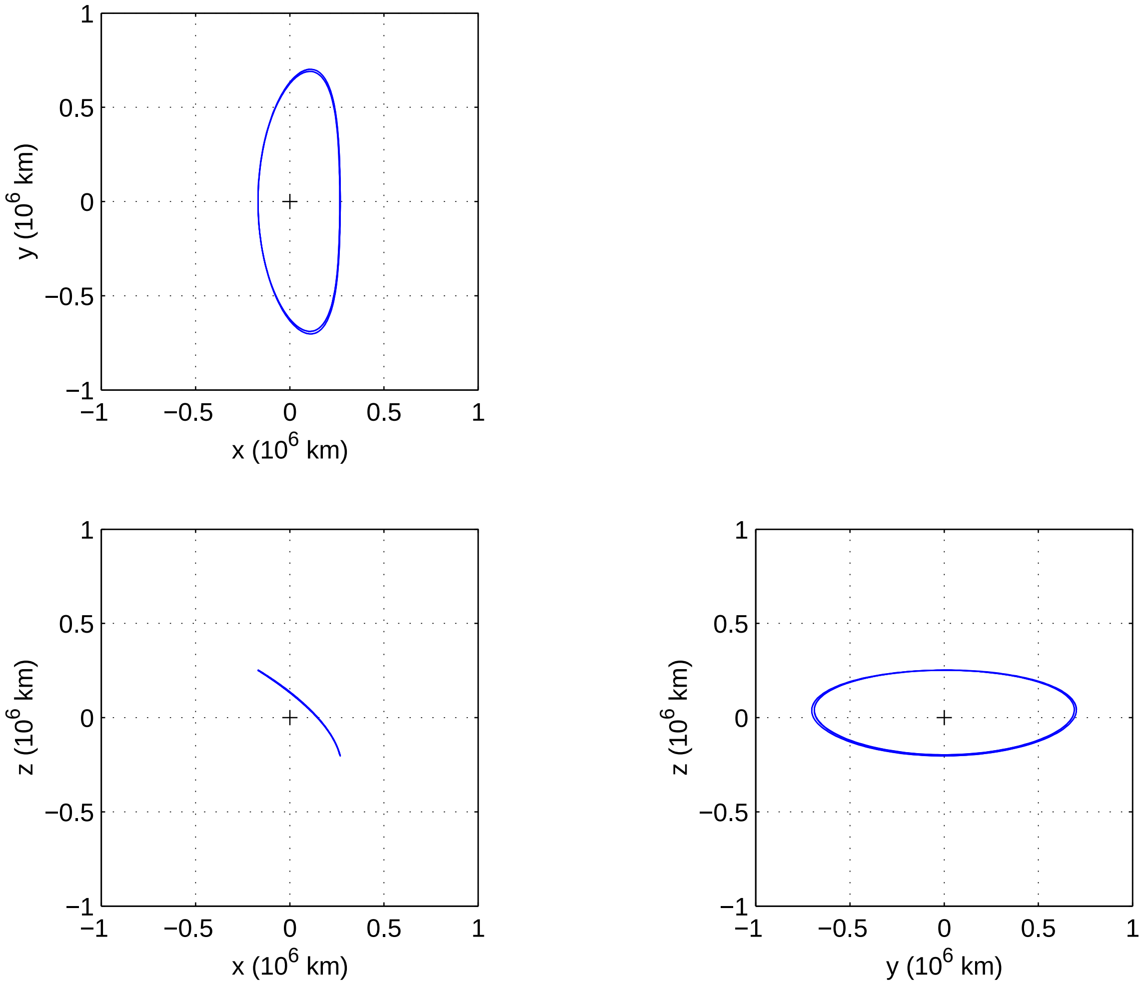

Figure 2.9. "Halo"-like Lissajous Trajectory Near the SEM L_1 Point (EPHEM)

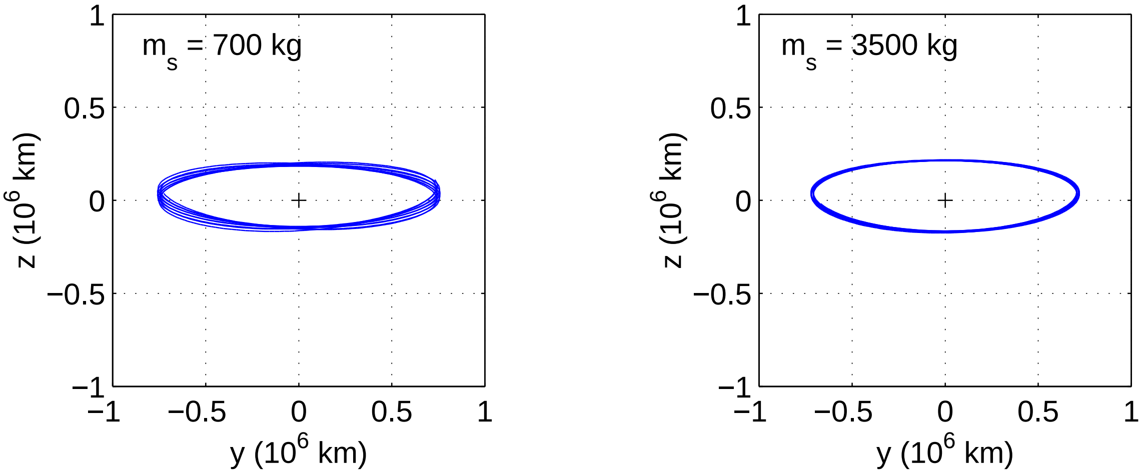

Figure 2.10. Impact of S/C Mass and SRP on a “Halo”-like Lissajous Trajectory

Suppose that the spacecraft is modeled as a flat plate. It is immediately obvious, from Equation (2.22), that the highest impact due to SRP occurs when the plate is normal to the incident photons, $\beta_{srp} = 0$ and $\hat{n} = \bar{d}/d$. In this study, it is assumed that the vehicle is always oriented such that $\beta_{srp} = 0$. In general, the inclusion of solar radiation pressure into the model has the most noticeable effect when the spacecraft mass is small relative to the effective area, as deduced from Equation (2.22). For instance, suppose the chief spacecraft in a formation evolves along a “halo” orbit near L_2, as determined in the Sun-Earth/Moon EPHEM model. If the mass of the spacecraft is 3500 kg, the impact of the SRP force on the path of the vehicle is barely noticeable, compared to the effect on a 700 kg spacecraft, as observed in Figure 2.10.

Impact of Modeling Assumptions on Particular Solutions

To illustrate how the modeling assumptions ultimately affect a particular solution, consider, once again, the TPF combiner spacecraft described by the parameters in Table 2.1. The impact of the choice of dynamical model on a "halo" orbit near the instantaneous L_2 point of the Sun-Earth system, as observed in the RLP frame, appears in Figure 2.11. The top left trajectory represents the projection of a three-dimensional halo orbit, with $A_z = 2 \times 10^5$ km, onto the rotating yz-plane. This solution is determined in the CR3BP and is exactly periodic. The top right figure depicts the same trajectory but transitioned into the EPHEM model (no periodicity). The orbit in the bottom left figure is also associated with the Sun-Earth EPHEM model but as perturbed by the Moon. Finally, the bottom right represents the same trajectory in the Sun-Earth/Moon system but includes SRP effects. Clearly, the dynamical model has a visible impact on the orbit. However, although the inclusion of SRP appears to have some visible effect on an individual trajectory, numerical evidence suggests that the net formation keeping costs are not significantly affected by adding SRP to the dynamical model.

Formation Control in the Ephemeris Model

The equations of motion for both the chief and deputy spacecraft may be expressed in the following form,

$$
\begin{aligned}
{}^{I}\ddot{\bar{r}}_{I}^{P_2C} &= \bar{f}^{(C)} + \bar{u}_C\left(t\right), && (2.23)\\
{}^{I}\ddot{\bar{r}}_{I}^{P_2D_i} &= \bar{f}^{(D_i)} + \bar{u}_{D_i}\left(t\right), && (2.24)
\end{aligned}
$$

where $\bar{f}^{(D_i)}$ and $\bar{f}^{(C)}$ represent the combined effect of all external forces and kinematic terms, if present. Also, $\bar{u}_C(t)$ and $\bar{u}_{D_i}(t)$ denote the control accelerations required to maintain the desired nominal configuration. These equations of motion are formulated in P_2-centered inertial frame (I) coordinates.

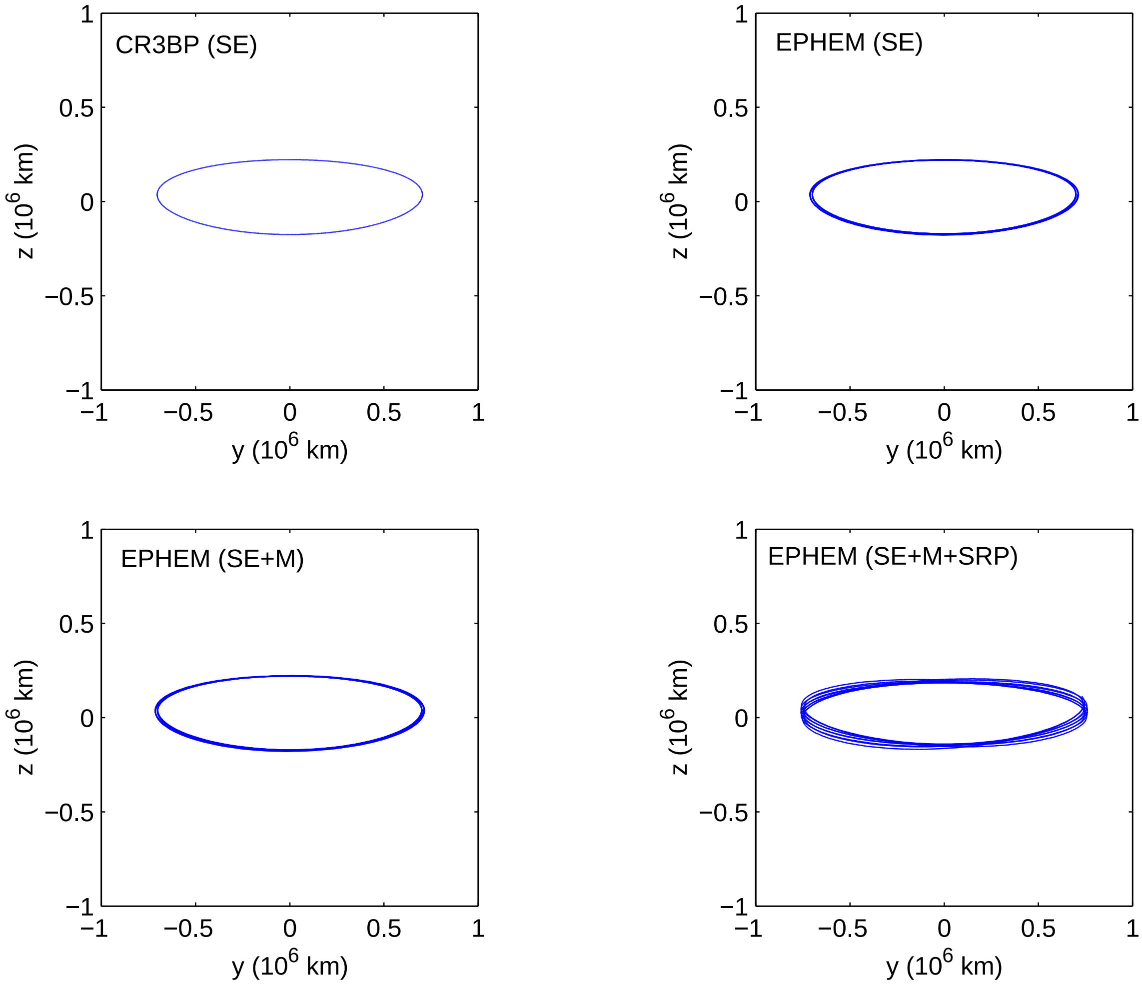

Figure 2.11. Impact of Modeling Assumptions on “Halo” (EPHEM)

Hence, the position of the i^{th} deputy in the formation is denoted $\bar{r}^{P_2 D_i} = x_i\hat{X} + y_i\hat{Y} + z_i\hat{Z}$. The vehicle velocities and accelerations are associated with the inertial frame (I). Note that, at this point, no assumptions have yet been made about the motion of the primaries in the system. Subsequently, Equations (2.23) and (2.24) are applicable to both the CR3BP and the EPHEM model.

In this study, the chief spacecraft in the formation is assumed to evolve along a natural solution of the unforced system. For instance, in the EPHEM model, the chief spacecraft evolves along a quasi-periodic Lissajous trajectory near the libration points. Since this is a naturally existing solution, the baseline control acceleration, $\bar{u}_c(t)$, is zero. The relative equations of motion for the i^{th} deputy, then, are easily determined by subtracting Equation (2.23) from (2.24),

$$ {}^{I}\ddot{\bar{r}}_{I}^{CD_i} = \left(\bar{f}^{(D_i)} - \bar{f}^{(C)}\right) + \bar{u}_{D_i}\left(t\right) = \Delta\bar{f}^{(D_i)} + \bar{u}_{D_i}\left(t\right). \tag{2.25} $$

The vector $\bar{r}^{CD_i}$ denotes the position of the i^{th} deputy relative to the chief spacecraft while $\Delta\bar{f}^{(D)_i}$ represents the relative net force vector. Let $\bar{\rho}$ represent the desired nominal path of the deputy spacecraft, then, $\dot{\bar{\rho}}$ designates the nominal velocity vector, and $\bar{u}^{o}_{D_i}(t)$ denotes the associated nominal control effort such that,

$$ {}^{I}\ddot{\bar{\rho}}_{I} = \Delta\bar{f}^{(D_i)^\circ} + \bar{u}^{\circ}_{D_i}\left(t\right). \tag{2.26} $$

The superscript "$\circ$" denotes evaluation on the nominal solution, $(\bar{\rho}, \dot{\bar{\rho}})$.

2.2 Nominal Motions

In this study, a variety of nominal motions are considered to assess the effectiveness of existing control techniques. These nominal motions are split into two categories; natural and non-natural formations. Natural formations satisfy the unforced equations of motion and exist in both the CR3BP and EPHEM models. Non-natural formations, on the other hand, are configurations that do not satisfy the unforced equations. Hence, continuous control is necessary to maintain the desired relative dynamics.

For instance, in the n-body problem, fixing the distance between the chief and the deputy spacecraft at a constant value represents a non-natural solution, regardless of the orientation constraints. This is easily verified by substituting the associated nominal state into the equations of motion.

2.2.1 Non-Natural Formations

The non-natural configurations considered in this investigation include:

- Fixed radial distance and orientation as observed in the rotating frame
- Fixed radial distance and orientation as observed in the inertial frame
- Fixed radial distance with no orientation constraints
- Fixed radial distance at some specified rotation rate
- Aspherical Formations

For non-natural motions, the "nominal" solution implies both the nominal state vector and the nominal control input required to maintain that state. The linearized dynamics are defined about this nominal solution. Hence, any control strategy that relies on the linearized dynamics of the system, such as LQR, requires that a nominal formation keeping cost be initially determined.

Formations Fixed Relative to the Rotating Frame

One possible type of formation corresponds to a configuration such that the relative distance between the chief spacecraft and the deputy is constant and the relative orientation of the chief-deputy line remains fixed with respect to the rotating frame (R). Mathematically, this constraint is specified by letting $\bar{r}_R^{CD_i} = \bar{c}$, where $\bar{c}$ is some constant vector, and ${}^R\dot{\bar{r}}_R^{CD_i} = \bar{0} = {}^R\ddot{\bar{r}}_R^{CD_i}$.

The right subscript R indicates that the vectors are written in terms of rotating frame coordinates, the left superscript serves to identify the frame of differentiation. Since Equation (2.25) is defined in terms of inertial coordinates, it is necessary to relate the formation constraints to this form of the dynamical model. It is easily verified that the acceleration term ${}^{R}\ddot{\bar{r}}_{R}^{CD_i}$ is related to ${}^{I}\ddot{\bar{r}}_{R}^{CD_i}$ through the kinematic expansion

$$ {}^{I}\ddot{\bar{r}}_{R}^{CD_i} = {}^{R}\ddot{\bar{r}}_{R}^{CD_i} + {}^{R}\dot{\bar{\omega}}_{R} \times \bar{r}_{R}^{CD_i} + 2\bar{\omega}_{R} \times {}^{R}\dot{\bar{r}}_{R}^{CD_i} + \bar{\omega}_{R} \times \left(\bar{\omega}_{R} \times \bar{r}_{R}^{CD_i}\right), \tag{2.27} $$

where $\bar{\omega}_R$ represents the angular velocity of the rotating frame (R) with respect to the inertial frame (I). Since the nominal motion is specified by ${}^{R}\dot{\bar{r}}_{R}^{CD_i} = \bar{0}$ and ${}^{R}\ddot{\bar{r}}_{R}^{CD_i} = \bar{0}$, these terms vanish in the above expression. The nominal inertial acceleration, $\ddot{\bar{\rho}} = {}^{I}\ddot{\bar{r}}_{I}^{CD_i}$, is subsequently determined as

$$ \ddot{\bar{\rho}} = {}^{I}C^{R}\left[{}^{R}\dot{\bar{\omega}}_{R} \times \bar{r}_{R}^{CD_i} + \bar{\omega}_{R} \times \left(\bar{\omega}_{R} \times \bar{r}_{R}^{CD_i}\right)\right], \tag{2.28} $$

where ${}^{I}C^{R}$ represents the appropriate coordinate transformation matrix between the inertial and rotating frames. Substituting the above nominal inertial acceleration into Equation (2.26), the nominal control input vector is defined as

$$ \bar{u}_{D_i}^{\circ}(t) = {}^{I}C^{R}\left({}^{R}\dot{\bar{\omega}}_{R} \times \bar{c} + \bar{\omega}_{R} \times (\bar{\omega}_{R} \times \bar{c})\right) - \Delta\bar{f}^{(D_i)^{\circ}}. \tag{2.29} $$

Note, in the CR3BP, the angular acceleration term ${}^{R}\dot{\bar{\omega}}_{R}$ vanishes. That is, since the primaries are assumed to evolve along circular paths, $\bar{\omega}_R$ is constant in the CR3BP formulation. In the EPHEM model, the angular acceleration of the Sun-Earth line is non-zero and is determined directly from ephemeris information. This computation involves the use of ephemeris data in the relative equations of motion where the Sun is the central body, the Earth is the body of interest, and all the planets, as well as the Moon, are considered as perturbing bodies.

The total ΔV required to maintain the nominal state over a time interval Δt is then defined as

$$ \Delta V = \int_{t_0}^{t_0+\Delta t} \sqrt{\bar{u}_{D_i}^{\circ} \cdot \bar{u}_{D_i}^{\circ}}\, dt. \tag{2.30} $$

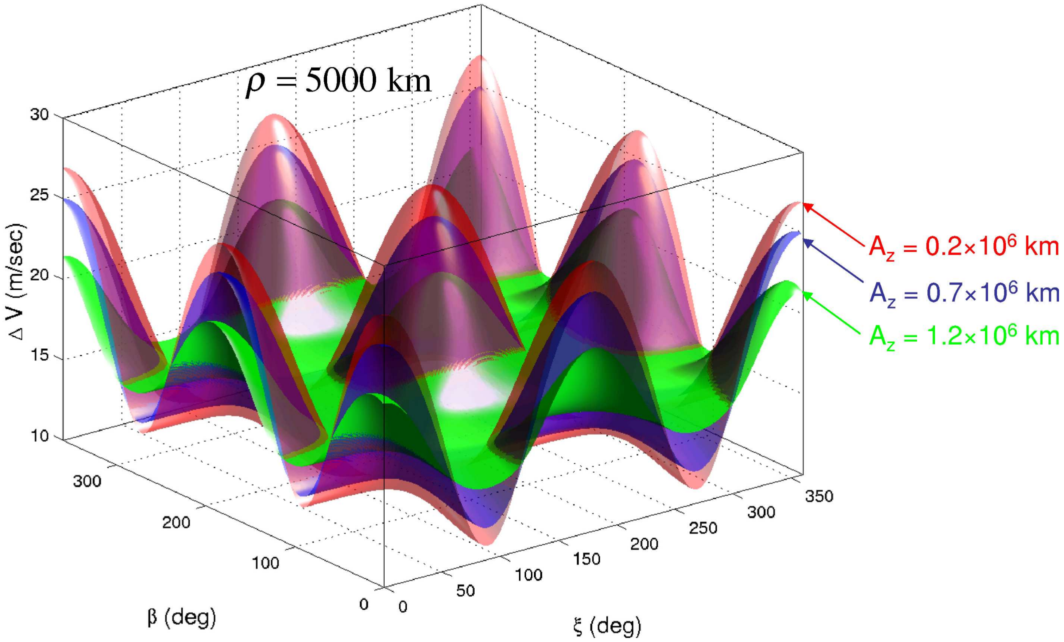

Figure 2.12. Impact of Formation Orientation on Nominal Cost

Numerically, this total cost is easily determined by augmenting the integration state vector, $\bar{X}_n$, by one element, $X_{n+1} = \sqrt{\bar{u}^{\circ}_{D_i} \cdot \bar{u}^{\circ}_{D_i}}$. To illustrate how the formation keeping cost is affected by the nominal separation and orientation of the formation, relative to the rotating frame, consider the following example. In the CR3BP, the chief spacecraft is assumed to evolve along a naturally periodic halo orbit and completes one revolution in approximately six months. Nominally, the deputy spacecraft is located at a specific distance (ρ) and orientation (ξ, β) relative to the chief, as illustrated in Figure 2.7. The elevation, β, of the chief-deputy line is measured relative to the reference xy-plane. The azimuth, ξ, is the angle measured between the x-axis of the reference coordinate system and the orthogonal plane that contains $\bar{\rho}$. In this particular case, ξ and β are measured relative to the rotating frame. The cost (ΔV) to maintain this formation fixed with respect to the rotating frame (R) is determined over one revolution along the path of the chief spacecraft (≈180 days). For a nominal separation of 5000 km, the total cost associated with maintaining a variety of orientations appears in Figure 2.12.

Three surfaces are displayed in Figure 2.12. The green surface corresponds to a halo orbit characterized by a 1.2×10^6 km out-of-plane amplitude (A_z), the intermediate blue contour is associated with an A_z of 700,000 km, and the red outline – with the greatest variation in height over the surface – corresponds to an A_z of 2×10^5 km. It is apparent, from Figure 2.12, that there are particular nominal orientations that can minimize or maximize the formation keeping cost. For instance, constraining the deputy spacecraft to remain aligned with the rotating y-axis ($\alpha = 90°$ and $\beta = 0°$) or the z-axes ($\beta = 90°$) minimizes the total ΔV. Conversely, if the deputy is constrained to remain aligned with the rotating x-axis ($\alpha = 0°$ and $\beta = 0°$) then the total ΔV is maximized. The trends apparent from the surfaces in Figure 2.12, however, do not hold along the entire halo family.

For the maximum and minimum cost configurations that are notable in Figure 2.12, Figure 2.13 illustrates how these costs vary along the L_1 and L_2 halo families. A single orbit along the family is represented in terms of its A_z amplitude. It is apparent, from Figure 2.13, there is a critical A_z amplitude at which the concavity of the cost surface in Figure 2.12 changes. Above this critical amplitude, there is only one minimum cost configuration and it corresponds to the case when the deputy vehicle is, in fact, aligned with the rotating x-axis. The trends from Figures 2.12 and 2.13 appear to hold regardless of the nominal separation. To illustrate how the cost is affected by the nominal relative separation, alone, consider the cost surfaces in Figure 2.12. If the nominal separation is decreased by one order of magnitude, the amplitude of the cost curves also decreases by one order of magnitude. Hence, if maintaining a 5000 km separation requires 10 m/sec over 180 days, then a 500 km would require 1.0 m/sec. Clearly, the total ΔV necessary to enforce a nominal separation on the order of meters, then, is extremely small.

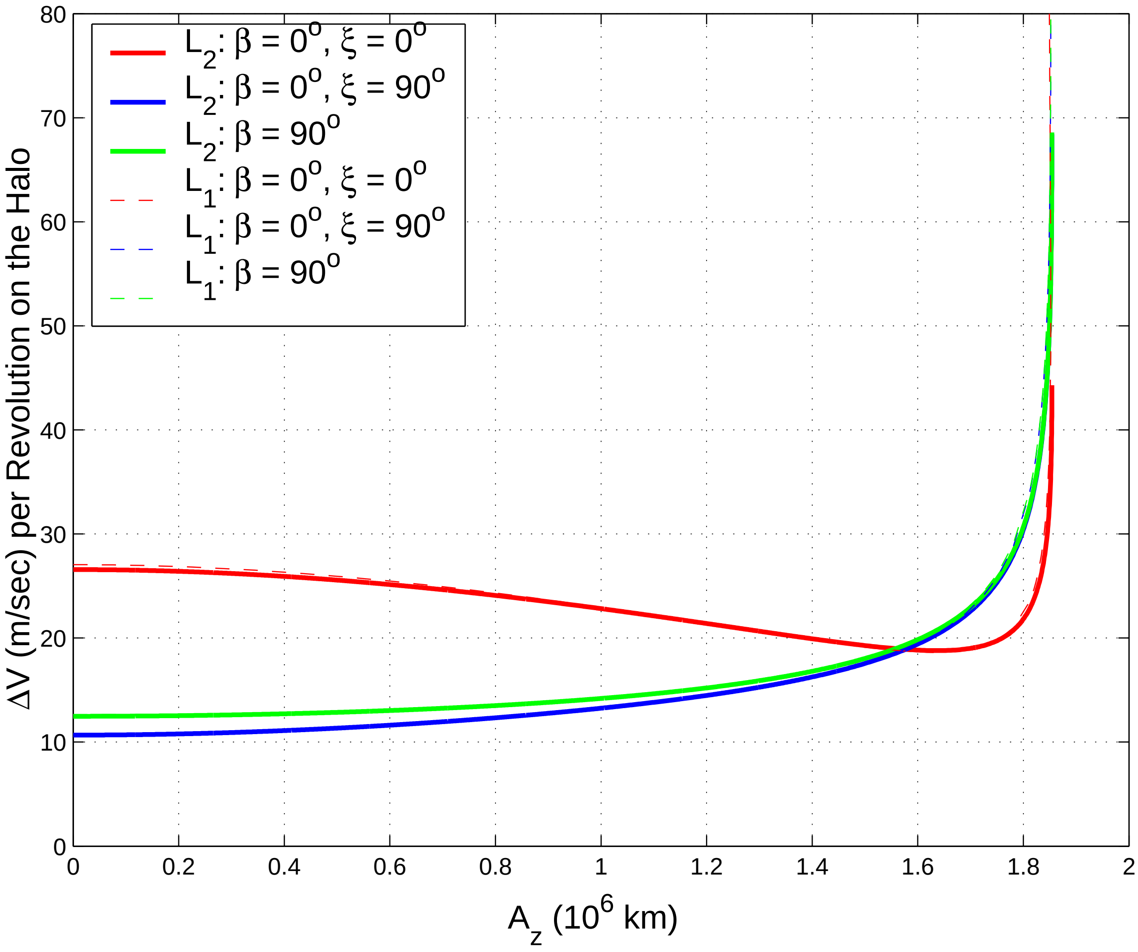

Figure 2.13. Formation Keeping Cost Changes Along Halo Family

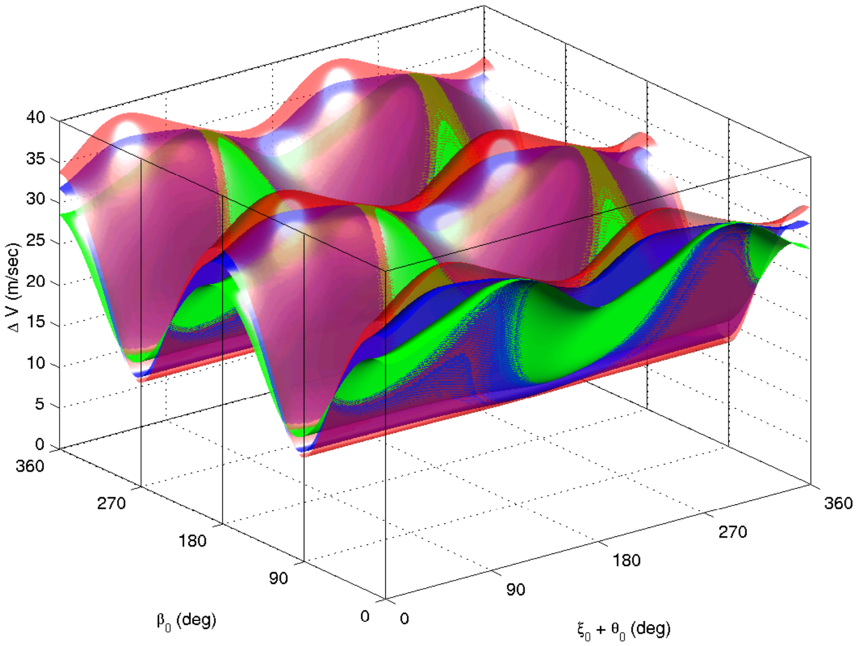

Figure 2.14. Impact of Formation Orientation on Nominal Cost for Formations Fixed in the Rotating Frame

Formations Fixed Relative to the Inertial Frame

A formation that is fixed with respect to the inertial frame (I) must satisfy ${}^I\dot{\bar{r}}_I^{CD_i} = {}^I\ddot{\bar{r}}_I^{CD_i} = \bar{0}$ for $\bar{r}_I^{CD_i} = \bar{\rho}$, where $\bar{\rho}$ is constant. Hence, the associated nominal control input, as determined from Equation (2.26), is simply determined as $\bar{u}^{\circ}_{D_i}(t) = -\Delta\bar{f}^{\circ}$. Unlike formations that are fixed relative to the rotating frame, the numerical evidence presented in Figure 2.14 suggests that the minimum and maximum costs, associated with an inertially fixed formation, depend only on the elevation, β, with respect to the plane of motion of the primaries. Note that, in this case, ξ and β are measured relative to the inertial reference frame. This appears to be true regardless of the out-of-plane A_z amplitude of the reference halo orbit. The maximum formation keeping cost, in this case, is associated with a formation that evolves in the plane of motion of the primaries for all time. The minimum cost, then, corresponds to a formation that is perpendicular to the plane of motion of the primaries as the chief S/C evolves along the halo orbit.

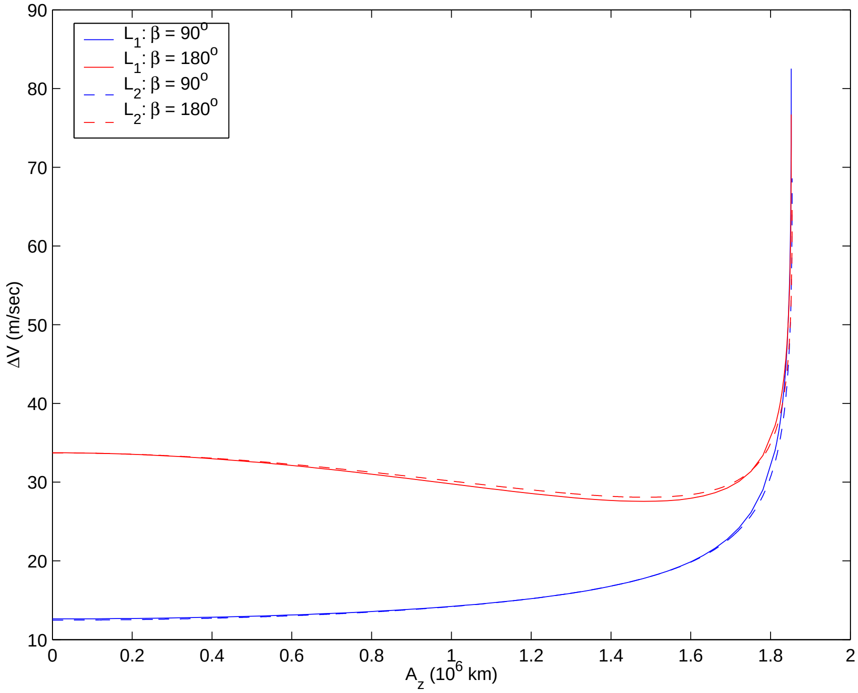

Figure 2.15. Impact of Formation Orientation on Nominal Cost for Inertially Fixed Formations

In a general sense, the trends observed in Figure 2.14 do hold throughout the halo family of solutions, as deduced from Figure 2.15. That is, the maximum cost and minimum cost formations are always associated with the same orientation regardless of the A_z amplitude of the reference orbit.

Fixed Radial Distance Without Orientation Constraints

A formation may also be specified by a number of constraints that depend explicitly on the state vector $\left(\bar{r}^{CD_i}, \dot{\bar{r}}^{CD_i}\right) = (\bar{r}, \dot{\bar{r}})$. In this case, a relation must be established between the state vector and the desired quantities before a control scheme can be devised.

For instance, if the formation requires that the radial distance remain fixed then, mathematically, this is equivalent to $r = \sqrt{\bar{r} \cdot \bar{r}}$ subject to $\dot{r} = 0$ and $\ddot{r} = 0$ where

$$\begin{aligned} \dot{r} &= \frac{{}^{I}\dot{\bar{r}} \cdot \bar{r}}{r}, & (2.31) \\ \ddot{r} &= \frac{\left(\Delta \bar{f}^{(D_i)} + \bar{u}_{D_i}\right) \cdot \bar{r}}{r} + \frac{{}^{I}\dot{\bar{r}} \cdot {}^{I}\dot{\bar{r}}}{r} - \frac{\dot{r}^2}{r}. & (2.32) \end{aligned}$$

Equation (2.32) represents a single scalar equation of constraint on the three control accelerations defined by $\bar{u}_{D_i}$. Hence, there exist an infinite number of solutions that satisfy this constraint.

One of these solutions corresponds to the condition that control inputs are applied solely along the radial direction. To illustrate this, define a formation frame in terms of unit vectors $\hat{r}$, $\hat{\theta}$, and $\hat{h}$ such that

$$\begin{aligned} \hat{r} &= \frac{\bar{r}}{|\bar{r}|}, & (2.33) \\ \hat{h} &= \frac{\bar{r} \times {}^{I}\dot{\bar{r}}}{|\bar{r} \times {}^{I}\dot{\bar{r}}|}, & (2.34) \\ \hat{\theta} &= \hat{h} \times \hat{r}. & (2.35) \end{aligned}$$

In this frame, the relative state of the deputy can be rewritten as $\bar{r} = r\hat{r}$ and ${}^{I}\dot{\bar{r}} = \dot{r}\hat{r} + r\dot{\theta}\hat{\theta}$. The angular rate, $\dot{\theta}$, is determined as

$$\dot{\theta} = \frac{\bar{r} \times {}^{I}\dot{\bar{r}}}{r^2}. \qquad (2.36)$$

Then, Equation (2.32) can be rewritten as

$$\ddot{r} - r\dot{\theta}^2 = \Delta f_r + u_r, \qquad (2.37)$$

where $\Delta f_r = \Delta \bar{f}^{D_i} \cdot \hat{r}$ and $u_r = \bar{u}_{D_i} \cdot \hat{r}$. It is clear, then, that

$$u_r^\circ = -\Delta f_r^\circ - r^\circ {\dot{\theta}^{\circ}}^{2}, \qquad (2.38)$$

is <u>one</u> possible solution that satisfies $\ddot{r} = 0$. Although this particular solution clearly satisfies the constraint defined by Equation (2.32), there is no guarantee or expectation of optimality. Other solutions are explored later in the discussion of the output feedback controller.

Fixed Radial Distance and Rotation Rate

Following the formulation defined previously, the rotation rate $\dot{\theta}$ may also be constrained as a requirement for the nominal formation. Suppose that the nominal configuration requires a fixed radial distance, but some rotation rate about the chief spacecraft is pre-specified. Recall that $\bar{h} = \bar{r} \times \dot{\bar{r}}$, where $\bar{r} = r\hat{r}$ and $\dot{\bar{r}} = \dot{r}\hat{r} + r\dot{\theta}\hat{\theta}$. This implies that $\bar{h} = (r^2\dot{\theta})\hat{h}$ and $\dot{\bar{h}}$ is determined as

$$\dot{\bar{h}} = \bar{r} \times \ddot{\bar{r}} = (r^2\ddot{\theta} + 2r\dot{r}\dot{\theta})\hat{h}. \tag{2.39}$$

In Equation (2.39), the unit vector $\hat{h}$ is <u>not</u> fixed inertially. Rather, it is computed at every instant in time, along with $\hat{r}$ and $\hat{\theta}$. Thus, $\hat{h}$ is normal to the instantaneous plane of motion. Furthermore, note that the cross product, $\bar{r} \times \ddot{\bar{r}}$, in this expression may also be evaluated from the forcing terms and control inputs in Equation (2.25),

$$\bar{r} \times \ddot{\bar{r}} = r(\Delta f_\theta + u_\theta)\hat{h} - r(\Delta f_h + u_h)\hat{\theta}, \tag{2.40}$$

where $\Delta f_\theta = \Delta\bar{f}^{(D_i)} \cdot \hat{\theta}$, $\Delta f_h = \Delta\bar{f}^{(D_i)} \cdot \hat{h}$, $u_\theta = \bar{u}_{D_i} \cdot \hat{\theta}$, $u_h = \bar{u}_{D_i} \cdot \hat{h}$. Combining Equations (2.39) and (2.40) leads to one equation of motion for θ, i.e.,

$$r\ddot{\theta} + 2\dot{r}\dot{\theta} = \Delta f_\theta + u_\theta, \tag{2.41}$$

and one equation of constraint,

$$\Delta f_h = -u_h. \tag{2.42}$$

If the above constraint is enforced, the instantaneous plane of motion, defined by $\hat{h}$, is fixed. If $\dot{\theta}$ is to remain constant, along with r, the following nominal cost is required,

$$u_r^\circ = -\Delta f_r^\circ - r^\circ{\dot{\theta}^{\circ}}^2 \tag{2.43}$$

$$u_\theta^\circ = -\Delta f_\theta^\circ \tag{2.44}$$

$$u_h^\circ = -\Delta f_h^\circ. \tag{2.45}$$

where the superscript "∘" implies evaluation along the nominal solution (r°, $\dot{\theta}^\circ$). Note that the above control inputs assume that the initial state of the deputy satisfies the nominal constraints. Sources of error must be addressed with additional control effort. The formulation for the more general problem is presented in Chapter 4.

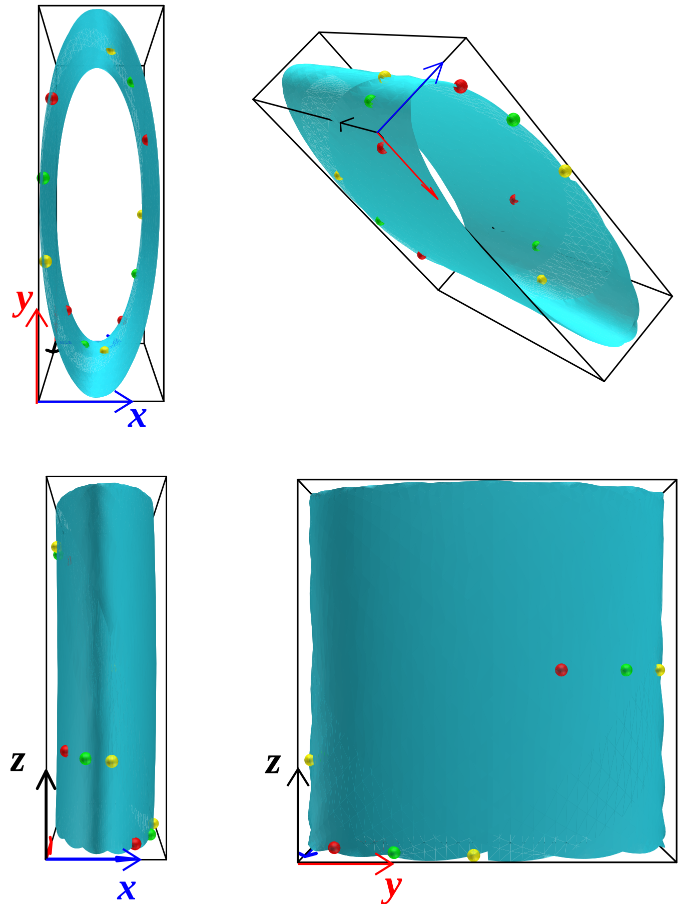

Figure 2.16. String of Pearls Formation

2.2.2 Natural Formations

The term “natural formations” refers to an appropriate phasing of the vehicles in the formation along naturally existing solutions near the libration points, such as Lissajous trajectories. One such type of formation identified in this study is analogous to the “string of pearls” formation familiar from two-body Earth orbiting formations. Such a formation is plotted in Figure 2.16 on a Liss surface. The surface in Figure 2.16 is traced by a quasi-periodic Lissajous trajectory, near the Sun-Earth/Moon L_2 point, as it completes 100 revolutions. This surface is determined in the SRP perturbed n-body EPHEM model.

By properly phasing each vehicle, it is possible for the formation to naturally evolve along this surface such that the relative positions of each spacecraft in the formation are unaltered and the relative distances are closely bounded. That is, if the formation originates as a string of pearls, the orientation of the string is relatively unaffected in time, the lead vehicle always remains in the lead and the order of each subsequent vehicle along the "string of pearls" remains unchanged. Since each spacecraft in this formation evolves along a naturally existing Lissajous trajectory, maintaining this type of formation can be achieved with a standard station keeping approach.

3. Natural Formations

The center manifold that exists in the immediate vicinity of the reference halo orbit allows for a variety of natural motions that may prove beneficial for formation flight missions. To numerically identify these regions, it is necessary to understand the eigenstructure associated with the reference orbit. To that end, the analysis of the center manifold presented here exploits the simplified model from the CR3BP. The reference orbit, then, is defined as a three-dimensional periodic halo orbit. The natural formation dynamics in the vicinity of the reference orbit are studied in detail. Once a suitable set of nominal configurations is identified, the results are easily transitioned into the EPHEM model via the two-level differential corrections process developed by Howell and Pernicka [40].

3.1 Floquet Analysis

Let $\bar{x}^*(t)$ denote the state vector, at time t, along a reference halo orbit near L_1 or L_2 in the CR3BP and let $\delta\bar{x}(t)$ denote a perturbation relative to $\bar{x}^*(t)$. Note that $\bar{x}$ and $\delta\bar{x}$ are associated with a formulation developed for the rotating frame as represented in Equations (2.1)-(2.3). Hence, the velocity elements of these vectors are associated with an observer fixed in the rotating frame. In terms of the linearized dynamics, the evolution of the perturbation vector $\delta\bar{x}(t)$ is governed by the state transition matrix, $\Phi(t,0)$, such that

$$\delta\bar{x}(t) = \Phi(t,0)\,\delta\bar{x}(0)\,. \tag{3.1}$$

Since the reference orbit is T-periodic, the state transition matrix admits a Floquet decomposition [30, 31] of the form

$$\Phi(t,0) = \tilde{P}(t)\,e^{Bt}\tilde{P}(0)^{-1}\,. \tag{3.2}$$

In Equation (3.2), $\tilde{P}(t) = \tilde{P}(t+T)$ is a periodic matrix, $\tilde{P}(0)$ is the identity matrix, and B is a constant matrix. Knowledge of the eigenvalues and eigenvectors of B allows the system in Equation (3.2) to be diagonalized such that,

$$\Phi(t,0) = E(t)e^{Jt}E(0)^{-1}. \tag{3.3}$$

Here, J is a block diagonal matrix determined from the eigenvalues of B and $E(t) = \tilde{P}(t)\tilde{S}$. The columns of $\tilde{S}$ are determined from the real and imaginary parts of the eigenvectors of the B matrix, as determined by the standard definition of the Real Jordan form of B. The matrix $E(t)$ is defined as the Floquet Modal matrix. Note that, since $\tilde{P}(t)$ is periodic, and $\tilde{S}$ is a constant matrix, the modal matrix is also periodic with $E(0) = \tilde{S}$.

Now, at any point in time, the perturbation $\delta\bar{x}(t)$ can be expressed in terms of any six-dimensional basis. The Floquet modes ($\bar{e}_j$), defined by the columns of $E(t)$, form a non-orthogonal six-dimensional basis. Hence, $\delta\bar{x}(t)$ can be expressed as

$$\delta\bar{x}(t) = \sum_{j=1}^{6} \delta\bar{x}_j(t) = \sum_{j=1}^{6} c_j(t)\,\bar{e}_j(t), \tag{3.4}$$

where $\delta\bar{x}_j(t)$ denotes the component of $\delta\bar{x}(t)$ along the j^{th} mode, $\bar{e}_j(t)$, and the coefficients $c_j(t)$ are easily determined as the elements of the vector $\bar{c}(t)$ defined by

$$\bar{c}(t) = E(t)^{-1}\,\delta\bar{x}(t). \tag{3.5}$$

The reference halo orbits of interest in this study are inherently unstable. The six-dimensional eigenstructure of the B matrix is thus characterized by one unstable eigenvalue (γ_1), one stable eigenvalue (γ_2), and four eigenvalues associated with the center subspace. Two of these neutrally stable eigenvalues are purely imaginary (γ_3 and γ_4) and the remaining two are exactly equal to zero (γ_5 and γ_6). The eigenvalues of the B matrix are commonly denoted the Floquet exponents. Howell and Keeter [30] and Gómez et al. [31] take advantage of this decomposition to develop a station keeping strategy for a single spacecraft evolving along a halo orbit.

In their study, Howell and Keeter (following Gómez et al.) determine a scheme comprised of a series of impulsive maneuvers that periodically remove the unstable component, $\delta\bar{x}_1$, of the perturbation, $\delta\bar{x}\,(t)$. For instance, let

$$\delta\bar{x}_n\,(t) = \sum_{j=2}^{6} \left(1 + \alpha_j\,(t)\right)\delta\bar{x}_j, \tag{3.6}$$

denote the desired perturbation relative to the reference orbit, where the $\alpha_j\,(t)$'s denote some, yet to be determined, coefficients. Note that the limits of the summation range from 2 through 6 which implies that the unstable mode, $\bar{e}_1$, has been removed. The control problem, then, reduces to finding the impulsive maneuver, $\Delta\bar{V}\,(t)$, such that

$$\sum_{j=2}^{6} \left(1 + \alpha_j\,(t)\right)\delta\bar{x}_j\,(t) = \sum_{j=1}^{6} \delta\bar{x}_j + \begin{bmatrix} 0_3 \\ \Delta\bar{V} \end{bmatrix}. \tag{3.7}$$

After some reduction, Equation (3.7) can be rewritten in matrix form as

$$\begin{bmatrix} \delta\bar{x}_{2r} & \delta\bar{x}_{3r} & \delta\bar{x}_{4r} & \delta\bar{x}_{5r} & \delta\bar{x}_{6r} & 0_3 \\ \delta\bar{x}_{2v} & \delta\bar{x}_{3v} & \delta\bar{x}_{4v} & \delta\bar{x}_{5v} & \delta\bar{x}_{6v} & -I_3 \end{bmatrix} \begin{bmatrix} \bar{\alpha} \\ \Delta\bar{V} \end{bmatrix} = \tilde{E}^{*}\bar{\alpha}^{*} = \delta\bar{x}_1, \tag{3.8}$$

where $\delta\bar{x}_{jr}$ refers to the first three elements of the vector $\delta\bar{x}_j$, $\delta\bar{x}_{jv}$ denotes the last three elements of $\delta\bar{x}_j$, and $\bar{\alpha}$ represents a 5×1 vector formed by the α_j coefficients in Equation (3.7). Howell and Keeter [30] identify the required $\Delta\bar{V}$ via a minimum norm solution. An exact solution is also considered in both [30] and [31] by constraining the maneuver to be performed along the Sun-Earth line ($\hat{x}$).

Although this approach was originally devised for station keeping of the reference orbit, in this study, a modified version of the methodology provides much insight for formation keeping in the three-body problem. In particular, a discrete three-axis control is implemented that removes the components of $\delta\bar{x}$ associated with the unstable mode ($\delta\bar{x}_1$) and two of the four center modes (($\delta\bar{x}_3$ and $\delta\bar{x}_4$) or ($\delta\bar{x}_5$ and $\delta\bar{x}_6$)). The particular set of two center modes that is removed depends on the type of formation that is sought.

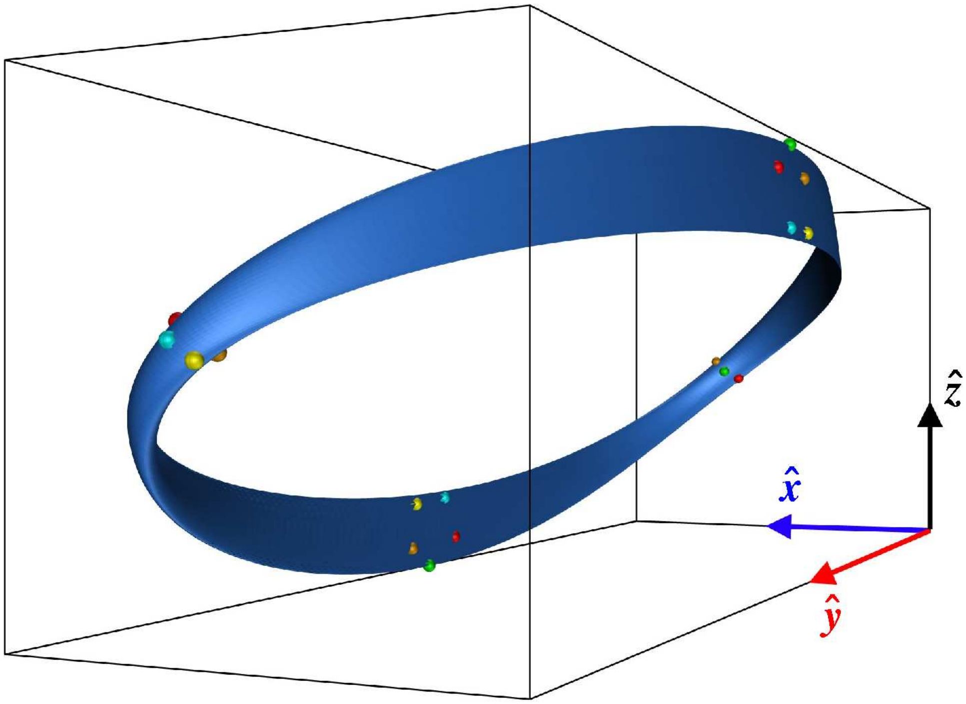

Figure 3.1. 2-D Hollow Torus That Envelops Halo Orbit
(Libration Point Centered View)

In general, the center modes point towards other bounded solutions that exist in the vicinity of the reference halo orbit. For instance, a solution that excites only modes $\bar{e}_3\,(t)$ and $\bar{e}_4\,(t)$ leads to a solution that resembles a two-dimensional hollow torus that is known to envelop the halo orbit, as plotted in Figure 3.1. The torus depicted in Figure 3.1 is determined relative to an observer fixed at the L_1 point of the Sun-Earth/Moon system. If the chief spacecraft is assumed to evolve along a halo orbit near L_1, and a deputy vehicle orbits the chief along the surface of the torus in Figure 3.1, the chief centered relative motion of the deputy due to the natural dynamics appears as plotted in Figure 3.2 If, instead, the initial state is entirely contained within the subspace spanned by $\bar{e}_5$ and $\bar{e}_6$, then the perturbed path corresponds to a neighboring halo orbit. A blend of subspaces reveals some interesting possible motion, however.

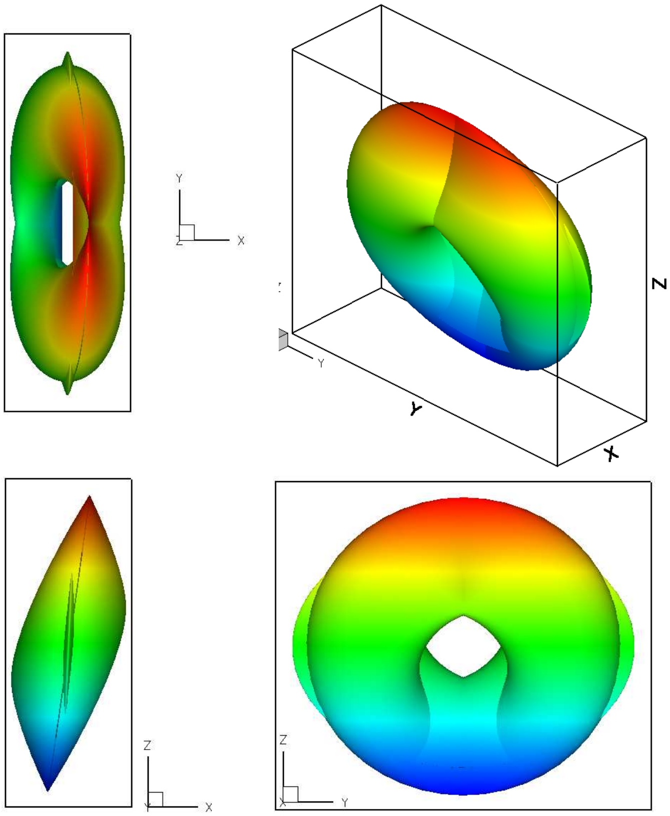

Figure 3.2. 2-D Hollow Torus That Envelops Halo Orbit
(Chief Spacecraft Centered View)

The controller developed by Howell and Keeter is modified here such that, at periodic time intervals, the unstable component of $\delta\bar{x}\,(t)$ is removed, along with two of the center modes. Through this approach, the $\Delta\bar{V}$ required to remove modes $\bar{e}_1$, $\bar{e}_3$, and $\bar{e}_4$ can be determined exactly from

$$\begin{bmatrix} \bar{\alpha} \\ \Delta\bar{V} \end{bmatrix} = \begin{bmatrix} \delta\bar{x}_{2\bar{r}} & \delta\bar{x}_{5\bar{r}} & \delta\bar{x}_{6\bar{r}} & 0_3 \\ \delta\bar{x}_{2\bar{v}} & \delta\bar{x}_{5\bar{v}} & \delta\bar{x}_{6\bar{v}} & -I_3 \end{bmatrix}^{-1} \left(\delta\bar{x}_1 + \delta\bar{x}_3 + \delta\bar{x}_4\right). \tag{3.9}$$

Similarly, the $\Delta\bar{V}$ required to remove modes $\bar{e}_1$, $\bar{e}_5$, and $\bar{e}_6$ is exactly determined from

$$\begin{bmatrix} \bar{\alpha} \\ \Delta\bar{V} \end{bmatrix} = \begin{bmatrix} \delta\bar{x}_{2\bar{r}} & \delta\bar{x}_{3\bar{r}} & \delta\bar{x}_{4\bar{r}} & 0_3 \\ \delta\bar{x}_{2\bar{v}} & \delta\bar{x}_{3\bar{v}} & \delta\bar{x}_{4\bar{v}} & -I_3 \end{bmatrix}^{-1} \left(\delta\bar{x}_1 + \delta\bar{x}_5 + \delta\bar{x}_6\right). \tag{3.10}$$

Either one of these controllers leads to motion that exhibits not only the overall features of the associated center subspaces, but also of the stable manifold that converges onto that region of space. As a direct result, the controllers described by Equations (3.9) and (3.10) not only define other potential nominal configurations, but also deployment into these configurations, as is demonstrated below.

3.1.1 Application: Deployment into Quasi-Periodic Torus Formation

Consider a two-spacecraft formation where the chief spacecraft is assumed to evolve along a 2×10^5 km halo orbit near the Sun-Earth/Moon L_1 point. Let the initial relative state of the deputy spacecraft be defined as $\bar{r} = 50\hat{x}$ m and $\bar{v} = (\hat{x} - \hat{y} + \hat{z})$ m/sec. Since the state is arbitrarily chosen, it is likely to have components along all six Floquet modes. Implementing an injection maneuver, based on Equation (3.10), allows modes 1, 5, and 6 to be removed. This leads to a single injection maneuver of roughly 1.73 m/sec. The resulting path appears in Figure 3.3. The first leg of the path is characteristic of motion along a stable manifold that ultimately converges onto the torus previously presented in Figure 3.2.

3.1.2 Application: Deployment into Nearly Periodic Formations

For the same reference halo orbit, consider three deputies deployed along with the chief spacecraft. Each deputy spacecraft arrives simultaneously at a different location relative to the chief. In particular, the relative position vectors are 50 meters, 100 meters, and 140 meters along the $+x$-direction. The relative velocity of each vehicle is still the same as that defined in the previous example. Application of the Floquet controller described by Equation (3.9) results in the delivery of each vehicle to a nearly periodic formation through a single injection maneuver.

Once again, the first leg along the path of each deputy resembles motion along a stable manifold that converges onto a nearly periodic relative orbit about the chief spacecraft, as observed from Figure 3.4. The resulting paths are propagated for 10 revolutions of the reference halo orbit (1800 days).

The converged paths in Figure 3.4 reveals a variety of very nearly periodic solutions in the vicinity of the chief spacecraft. To better visualize the potential configurations, Eight deputies evolving along nearly periodic orbits appear in Figure 3.5. The actual path of each is expanding, but does so very slowly. So, the individual orbits can be propagated for 100 revolutions of the reference halo and will still appear periodic. Let $\bar{r}\,(t)$ denote the vector formed by the position elements of $\delta\bar{x}\,(t)$. The orbits depicted in Figure 3.5 are obtained by applying the controller to a relative position vector of the form $\bar{r} = r_0\hat{y}$, where r_0 denotes some initial separation between the chief and deputy spacecraft. Note that the initial position for these trajectories is aligned with the y-axis, as opposed to those previously presented in Figure 3.4. The rate of expansion of these orbits is more noticeable if the initial position vector originates anywhere else in the yz-plane. In fact, the rate of expansion reaches a maximum if the initial relative position vector is of the form $\bar{r} = r_0\hat{z}$. In this case, the resulting orbits appear nearly vertical and are illustrated in Figure 3.6 using a four spacecraft formation as an example.

Figure 3.7 further illustrates how the rate of expansion changes as the initial state is shifted throughout the yz-plane. The sphere at the origin (the location of the chief) is included only to aid in visualizing the path of the deputy. Note that with no initial $z-$component, the orbit of the vehicle appears periodic. As an out-of-plane component is introduced into the initial state, the resulting trajectory blends the characteristics of the orbits in both Figures 3.5 and 3.6. Further propagating a nearly vertical orbit, characterized by $\bar{r}\,(0) = r_0\hat{z}$, over a period of 100 revolutions (49.2 years) yields the surface illustrated in Figure 3.8. Clearly, the rate of expansion is extremely slow and the deviation from the initial orientation is relatively small within the first few years.

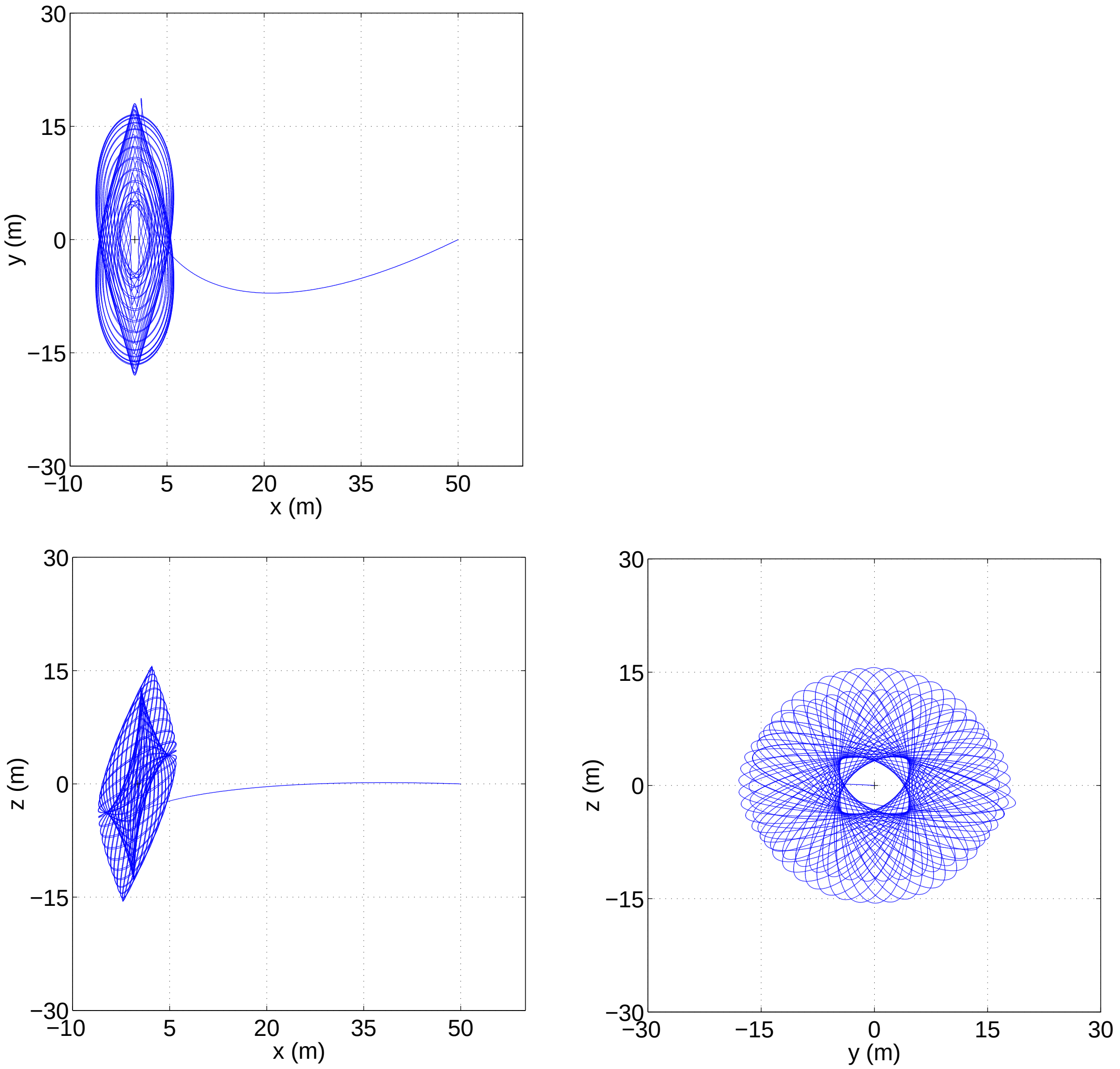

Figure 3.3. Deployment into Quasi-Periodic Relative Orbit

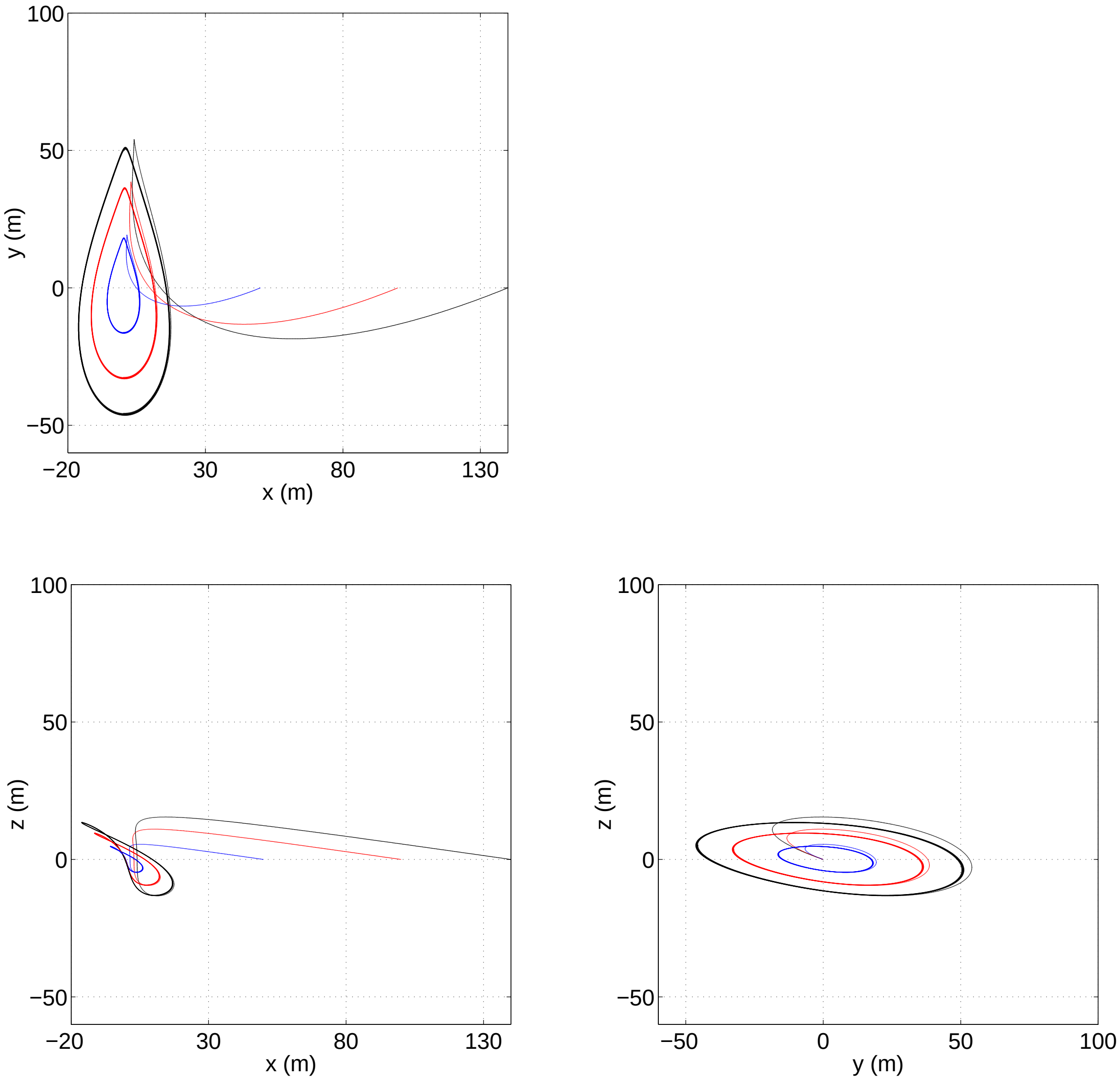

Figure 3.4. Deployment into Nearly Periodic Relative Orbit

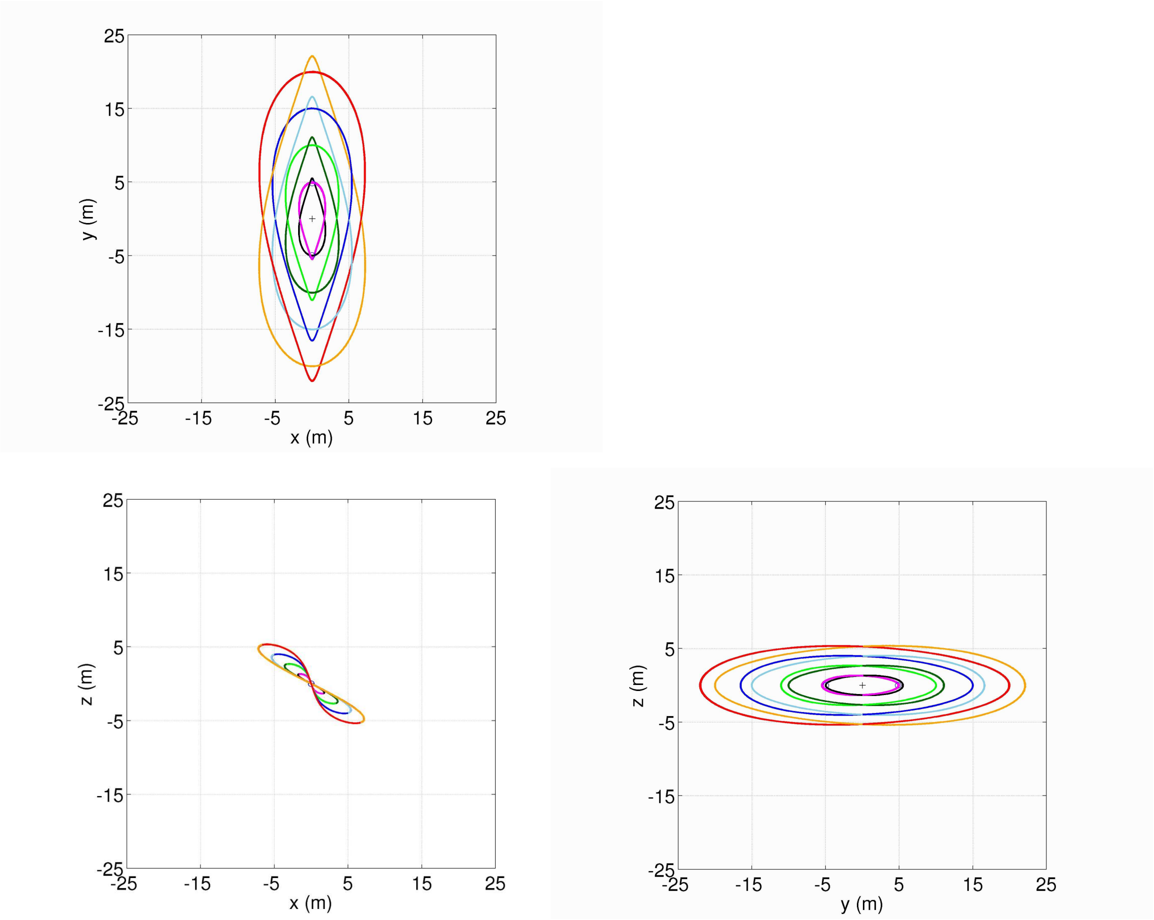

Figure 3.5. Nearly Periodic Relative Orbits About Chief S/C

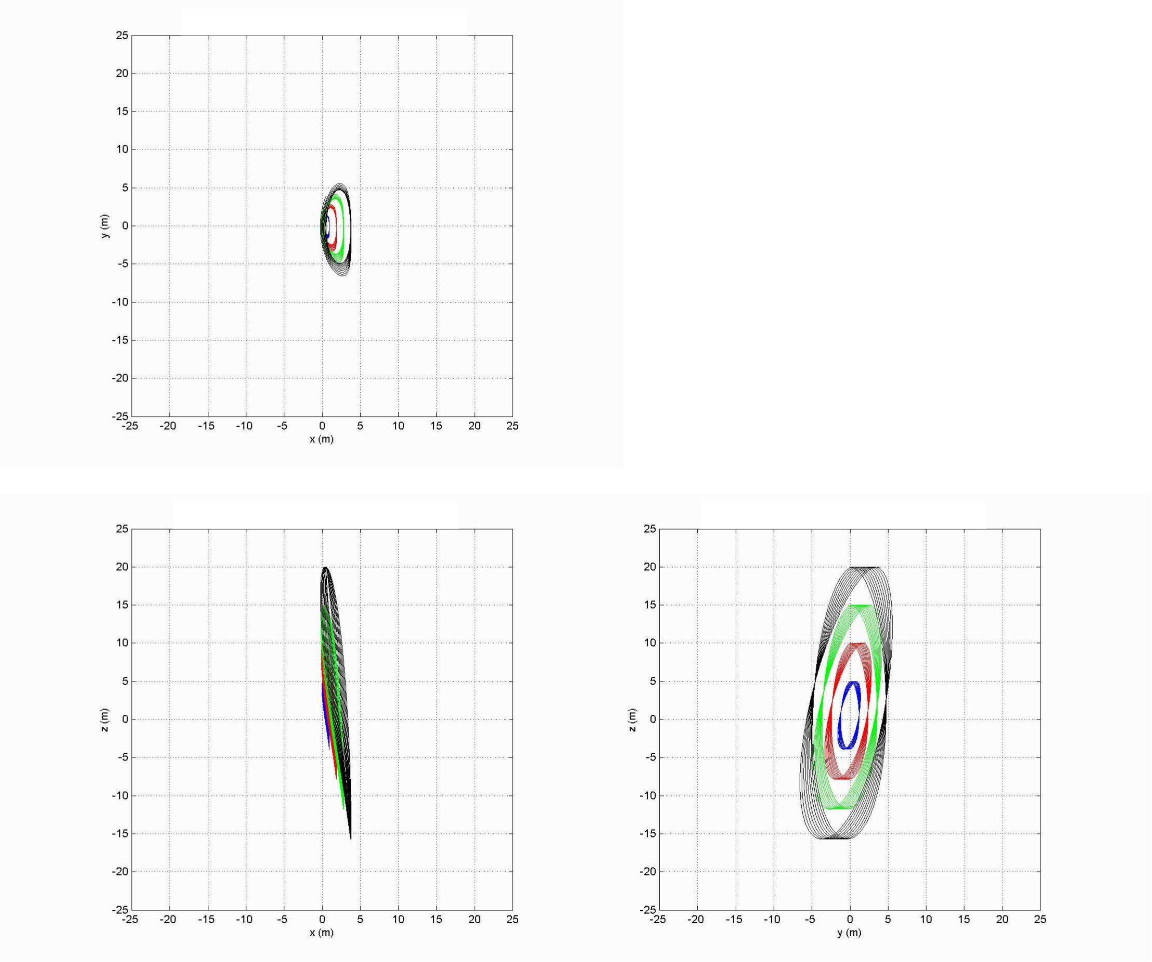

Figure 3.6. Nearly Vertical Relative Orbits About Chief S/C

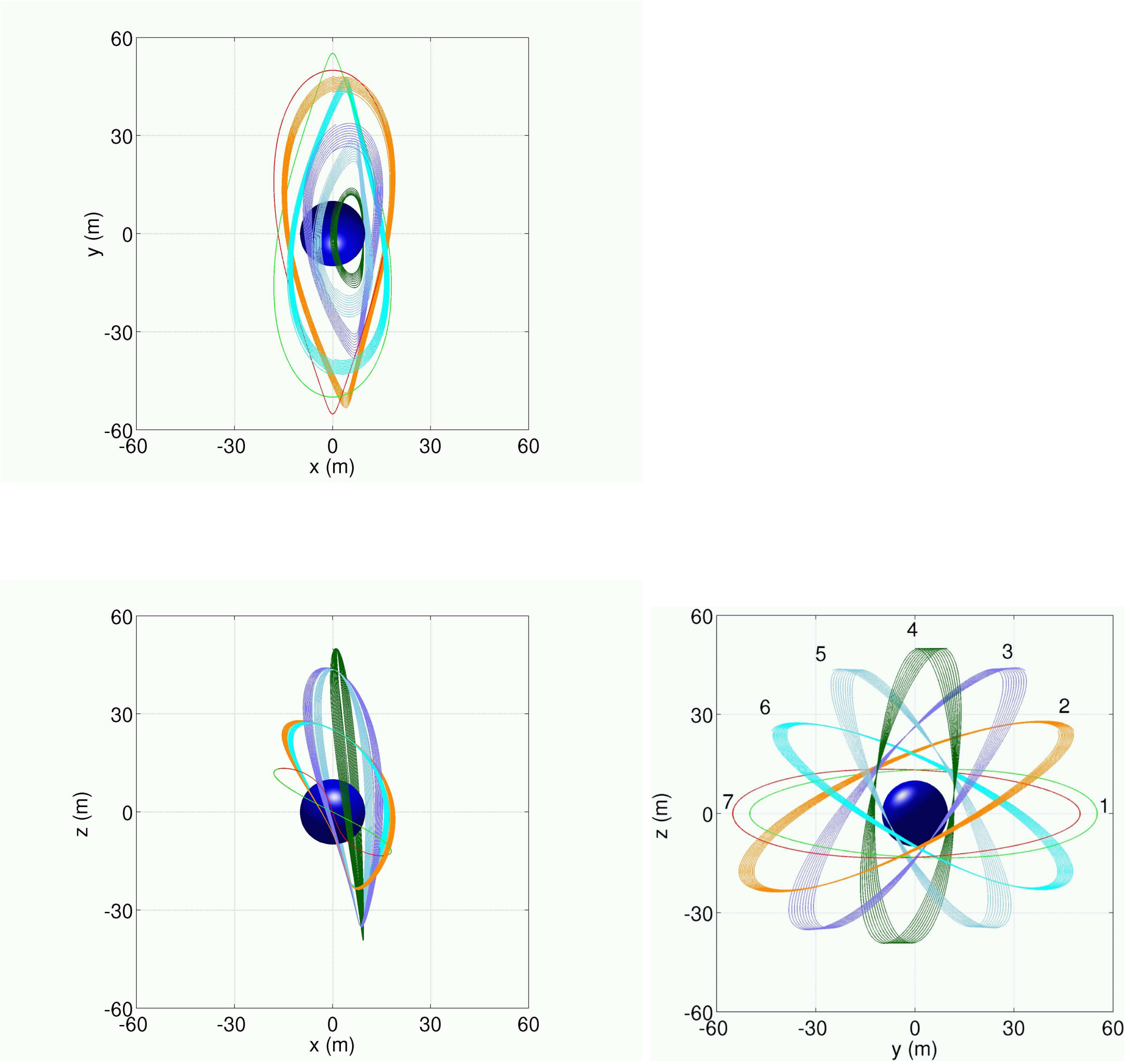

Figure 3.7. Variation in Relative Orbit Expansion Rate Along the yz-plane

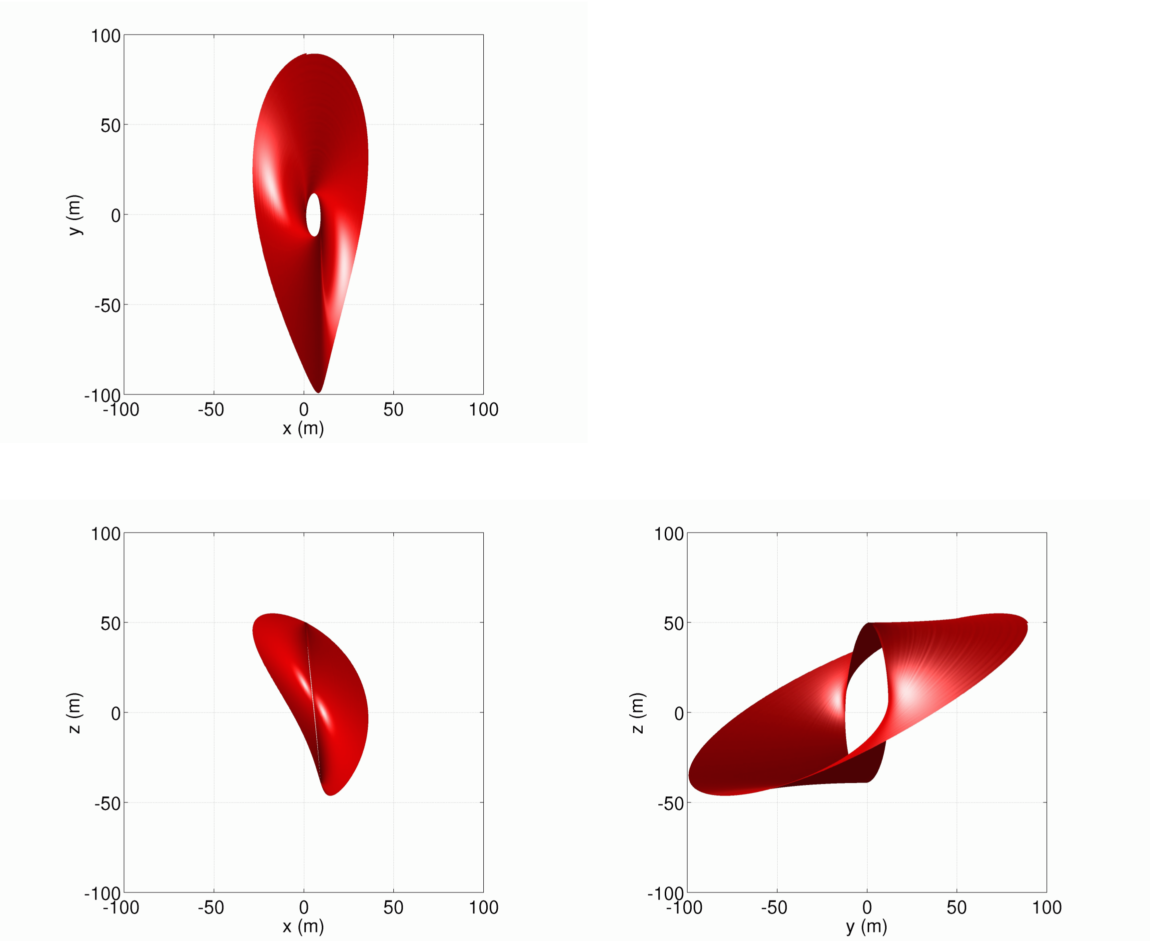

Figure 3.8. Evolution of Nearly Vertical Orbits Over 100 Revolutions (49.2 years)

4. Non-Natural Formations: Continuous Control

Several continuous control techniques are considered in this investigation for applications to formation keeping. Initially, the analysis is focused on linear control methodologies that include linear state feedback, subject to actuator lower bounds, an linear optimal control. Both of these methods are applied to formation keeping in the CR3BP. Nonlinear control techniques, including Input Feedback Linearization (IFL) and Output Feedback Linearization (OFL) are explored in both the CR3BP and EPHEM models. Continuous optimal nonlinear control is presented in the next chapter as a subset of discrete optimal control.

The first methodology presented in this section is based on linear state feedback subject to control input lower bounds. The discussion pertains to a methodology developed by Corless [44] and is applied, here, to the formation keeping problem. In its present stage of development, this particular methodology does not represent a feasible alternative for formation keeping near the libration points, as revealed in the following section. However, this approach serves as an excellent example to highlight the impact of the dynamical sensitivity of the model in the formation keeping problem.

The results of this investigation further reveal that a linear quadratic regulator (LQR) can yield essentially identical response and control input time histories as those obtained via the IFL approach. However, implementation of the IFL approach is computationally much less intensive and, by comparison, conceptually simpler than the LQR approach. This particular characteristic makes the IFL controller more suitable as a preliminary analysis tool in the EPHEM model. Control via OFL is also relatively straightforward with some additional advantages over IFL. In particular, instead of controlling to a nominal state vector, it is possible to control functions of the state vector, such as radial distance and spin rate.

4.1 Linear State Feedback Subject to Bounded Control Inputs

Recall, from Equation (2.16), that the relative equations of motion for the deputy spacecraft may be summarized as

$$\ddot{\bar{r}}(t) = \Delta\bar{f}\left(\bar{r}(t), \dot{\bar{r}}(t)\right) + \bar{u}_{D_i}(t)\,, \tag{4.1}$$

where $\bar{r}(t)$ represents the position vector from the chief vehicle to the deputy spacecraft and $\dot{\bar{r}}(t)$ denotes the relative velocity. The vector $\bar{u}_{D_i}(t)$ represents the actual control input applied to force the deputy to track the desired nominal motion. Note that the nominal path must also satisfy Equation (4.1), thus,

$$\ddot{\bar{r}}^{\circ}(t) = \Delta\bar{f}\left(\bar{r}^{\circ}(t), \dot{\bar{r}}^{\circ}(t)\right) + \bar{u}^{\circ}_{D_i}(t)\,. \tag{4.2}$$

If the desired solution is not consistent with the natural dynamics, then the nominal control effort, $\bar{u}^{\circ}_{D_i}(t)$, is non-zero. The relative error dynamics are then determined by subtracting Equation (4.2) from (4.1),

$$\ddot{\bar{e}}(t) = \bar{u}_{D_i}(t) + \left[\Delta\bar{f}\left(\bar{r}(t), \dot{\bar{r}}(t)\right) - \Delta\bar{f}\left(\bar{r}^{\circ}(t), \dot{\bar{r}}^{\circ}(t)\right) - \bar{u}^{\circ}_{D_i}(t)\right]. \tag{4.3}$$

The nonlinear dynamical model described by Equation (4.3) may be summarized, in first order form, as

$$\dot{\bar{x}}(t) = A\bar{x}(t) + B\bar{u}_{D_i}(t) + B\tilde{w}(t), \tag{4.4}$$

where $\bar{x}(t)$ is a 6×1 vector whose elements are $\bar{e}(t)$ and $\dot{\bar{e}}(t)$, respectively, while

$$A = \begin{bmatrix} 0 & I \\ 0 & 0 \end{bmatrix}, \tag{4.5}$$

and

$$B = \begin{bmatrix} 0 \\ I \end{bmatrix}. \tag{4.6}$$

The nonlinear terms are contained within the vector $\tilde{w}(t)$. Near the libration points, and for small relative separations, the term $\tilde{w}(t)$ <u>can</u> be very small. Whether or not that is true depends on the nominal motion that is specified. Note that, if $\tilde{w} = \bar{0}$, the resulting system of equations is linear.

For the linear system, Corless [44] develops a linear state feedback approach, subject to control input lower bounds ($||\bar{u}_{D_i}(t)|| \geq \beta_u$), that seeks to stabilize the response. Hence, in his initial development, the nonlinear terms in Equation (4.3) are assumed to be sufficiently small to be considered negligible. This is only done initially to assess if the linear system is stabilizable in the presence of control inputs that are subject to a lower bound. At a later point in this formulation, Corless does include the nonlinear terms. To deal with this lower bound, the following control laws are considered:

1. Control Law 1:

$$\bar{u}_{D_i}(t) = \begin{bmatrix} K\bar{x}, & \|K\bar{x}\| \geq \beta_u \\ \beta_u \frac{K\bar{x}}{\|K\bar{x}\|}, & \|K\bar{x}\| < \beta_u \end{bmatrix} \tag{4.7}$$

   In this particular control law, the input is continuously applied either at or above the lower bound. As demonstrated in [44], this type of bounded state feedback does not stabilize the linear system.

2. Control Law 2:

$$\bar{u}_{D_i}(t) = \begin{bmatrix} K\bar{x}, & \|K\bar{x}\| \geq \beta_u \\ \bar{0}, & \|K\bar{x}\| < \beta_u \end{bmatrix} \tag{4.8}$$

   In this example, the thrusters are deactivated once the lower bound is reached and they remain off until the linear state feedback is greater than the lower bound. This form of control law also does not stabilize the linear system, as detailed in [44].

3. Control Law 3:

   In the absence of any actuator constraints, the pair (A, B) is stabilizable. Hence, there is a unique symmetric positive definite matrix, P, that satisfies the Algebraic Riccati Equation (ARE) $PA + A^T P - \lambda PBB^T P + Q = 0$ for some specified weighting matrix Q.

For a gain matrix defined by $K = -\lambda B^T P$, a feedback control law of the form $\bar{u}_{D_i} = K\bar{x}(t)$ leads to an asymptotically stable closed loop system. An actuator lower bound may be incorporated by defining

$$\bar{u}_{D_i}(t) = \begin{bmatrix} K\bar{x} & \|K\bar{x}\| \geq \beta_u \\ \beta_u \frac{K\bar{x}}{\|K\bar{x}\|} & \|K\bar{x}\| < \beta_u \end{bmatrix}. \tag{4.9}$$

However, this control law cannot be physically implemented because the system is discontinuous and existence of solutions is not guaranteed, as discussed in [44].

4. Control Law 4:

To overcome the issues associated with Equation (4.9), Corless proposes an alternate switching controller of the form

$$\bar{u}_{D_i}(t) = \begin{bmatrix} K\bar{x} & \|K\bar{x}\| > \beta_u \\ \beta_u \frac{K\bar{x}}{\|K\bar{x}\|} & \epsilon_2 < \|K\bar{x}\| < \beta_u \\ \beta_u \frac{K\bar{x}}{\|K\bar{x}\|} \text{ or } 0 & \epsilon_1 < \|K\bar{x}\| < \epsilon_2 \\ 0 & 0 < \|K\bar{x}\| < \epsilon_1 \end{bmatrix}. \tag{4.10}$$

The control law in this equation is best described by Figure 4.1. As detailed in his work, implementation of this last controller in the nonlinear system can stabilize the nonlinear system if ϵ_2 is sufficiently small.

The examples presented in [44] are associated with a relatively simple scalar nonlinear system. Furthermore, the nominal configuration cannot be achieved exactly, with the approach in Equation (4.10), because the nonlinear terms are not accounted for in the control law. The goal of this section is to determine if the control law in Equation (4.10) can be successfully applied for formation keeping and how closely the desired tolerances can be achieved.

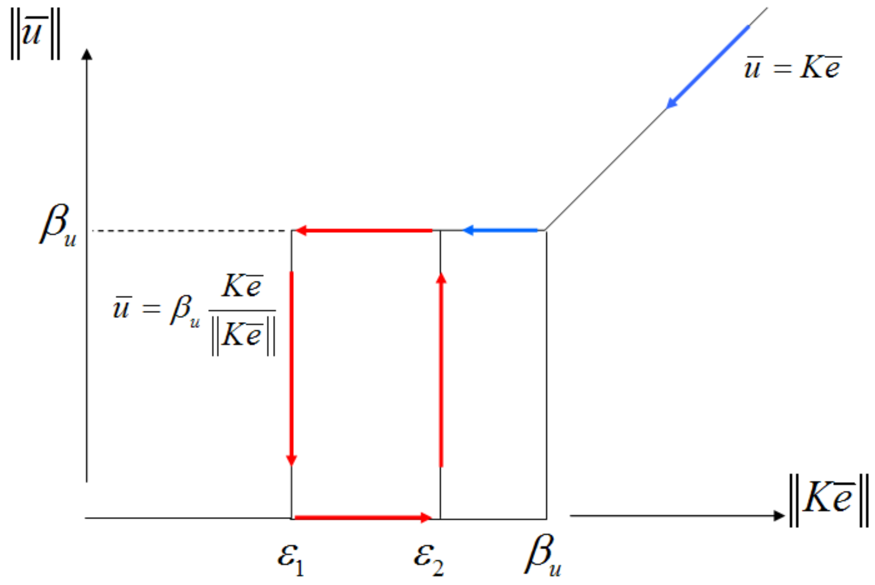

Figure 4.1. Linear State Feedback Control Law with Lower Input Bounds

A critically damped error response is sought in this case. Consistent with this constraint, let $\bar{u}_{D_i}(t) = K\bar{x}(t)$, where

$$K = -\begin{bmatrix} \omega_n^2 I_3 & 2\omega_n I_3 \end{bmatrix}. \tag{4.11}$$

It is possible to show that the choice of K specified in Equation (4.11) satisfies the algebraic Riccati Equation (ARE),

$$A^T S + SA - SBR^{-1}B^T S + Q = 0 \tag{4.12}$$

for

$$Q = \begin{bmatrix} \omega_n^4 I_3 & 0 \\ 0 & 2\omega_n^2 I_3 \end{bmatrix}, \tag{4.13}$$

$$S = \begin{bmatrix} 2\omega_n^3 I_3 & \omega_n^2 I_3 \\ \omega_n^2 I_3 & 2\omega_n I \end{bmatrix}, \tag{4.14}$$

and $K = -R^{-1}B^T S$ with $R = I$.

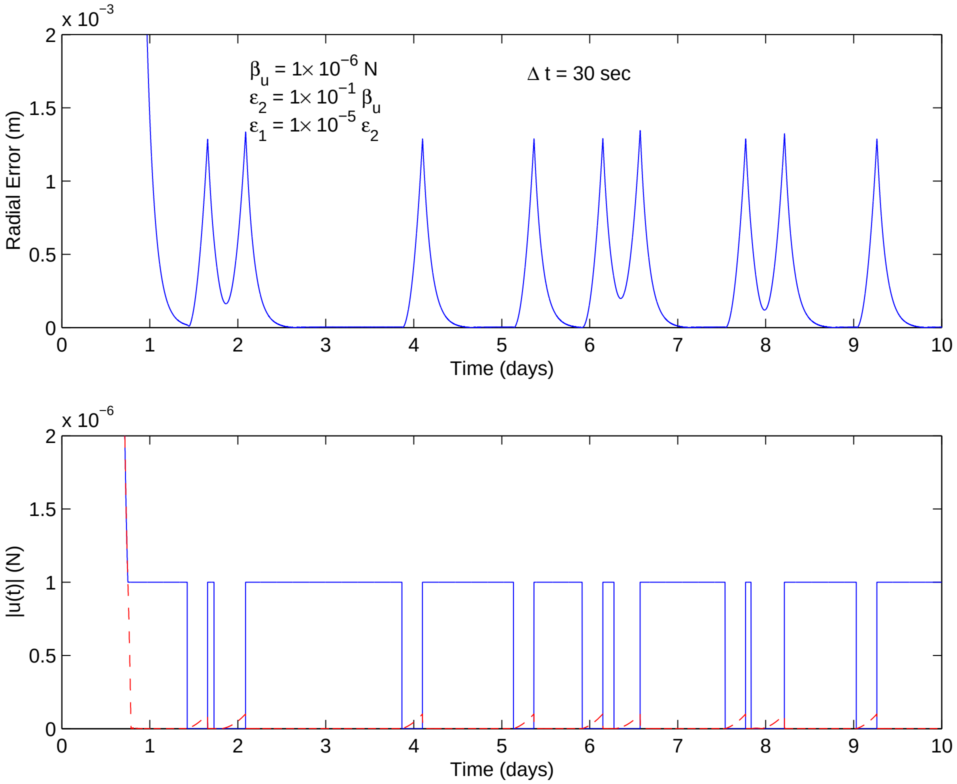

Figure 4.2. Linear State Feedback with Actuator Lower Bounds: Magnitude of Position Error for Example 1

To illustrate how this controller performs for formation keeping applications near the libration points consider the following example. Let $\bar{r}(t)^{\circ} = (50 \text{ m})\hat{z}$ denote the nominal relative position of the deputy. Suppose that the initial state error is characterized by $\delta\bar{r} = [7, -5, 3.5]$ km and $\delta\dot{\bar{r}} = [1, -1, 1]$ m/sec, where δ denotes a quantity that is perturbed relative to the nominal state. Let $\beta_u = 1 \times 10^{-6} N$ represent the minimum thrust deliverable by the onboard propulsion system. Furthermore, let $\epsilon_2 = 1 \times 10^{-1}\beta_u$ and $\epsilon_1 = 1 \times 10^{-5}\epsilon_2$ and let the integration step size be defined as 30 seconds. The control law in Equation (4.10) leads to the results in Figure 4.2. On a large scale view, the results in Figure 4.2 appear to converge as specified by the critically damped response. The more interesting features, however, occur once the controller switching sequence is initiated.

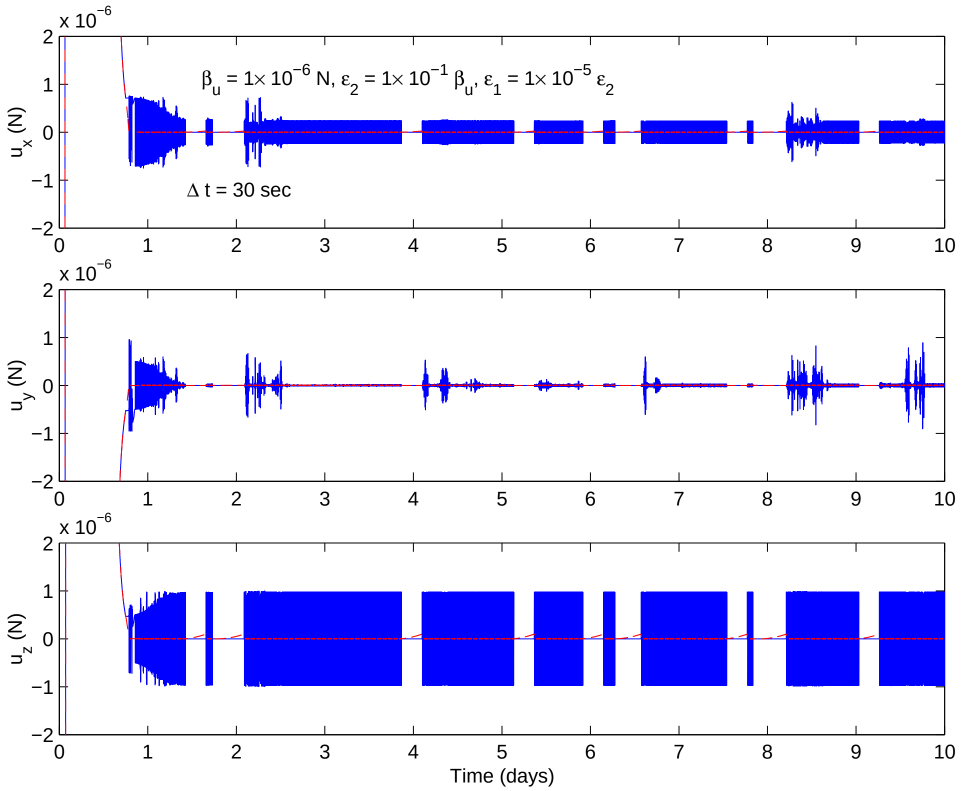

Figure 4.3. Linear State Feedback with Actuator Lower Bounds:
Control Inputs Along Each Rotating Axis for Example 1

The top plot in Figure 4.2 represents a close-up view of the response, presented in terms of the magnitude of the state error. The bottom figure, then, illustrates the magnitude of both the control input that is actually applied in the nonlinear system, represented by a solid blue line, and the linear state feedback control input, identified as the dashed red curve. When the controller is switched off, the solution begins to diverge away from the nominal, as expected. The average magnitude of the error depends on the value of ϵ_2, as demonstrated by Corless [44]. Hence, in theory, the magnitude of the relative state error can be made arbitrarily small by reducing ϵ_2.

Note, from Figure 4.3, that the individual control accelerations, applied in each direction, are not subject to this lower bound. In the development presented in [44], only the magnitude of the control input is bounded. No such constraint is placed on the magnitude of the individual thrust inputs.

Ultimately, the numerical analysis must be based on the realistic capabilities of the onboard propulsion system for a particular spacecraft. This requires that constraints be imposed on the thrust inputs in each direction. In addition, the results in Figure 4.3 suggest that the control solution is not continuous. Upon closer inspection of these results, it appears that the control law pulses, while alternating thrust directions, with every step of the integration. The pulse frequency, however, is very high and may not represent an acceptable solution for a particular mission.

In addition, since the solution is discontinuous, and the dynamical model is highly sensitive to small perturbations, the results themselves are very sensitive to the choice of integrator, the integration tolerance and step size, and the machine precision. To illustrate this, consider the exact same example but with a step size of 10 minutes instead of 30 seconds. As deduced from Figure 4.4, the control input is applied continuously. Hence, the thrusters are never switched off in this case. The result is a solution that exhibits numerical chatter and an average offset from the nominal path. As detailed in [44], the controller must switch off to achieve asymptotic stability between thrust segments. The results in Figure 4.4 validate this statement since the error level remains at a constant offset from the nominal. Also, the thrust inputs are still discontinuous as evidenced from Figure 4.5.

Since linear state feedback, as presently developed in [44], appears to be sensitive to the numerical solution process and the associated parameters, this method does not currently represent a feasible alternative for formation keeping near the libration points. Certainly, any feasible formation keeping strategy requires that the control solution be consistently reproduced regardless of the numerical integration scheme employed. Future stages of development may, however, lead to a more feasible solution. Of course, regardless of whether or not this method is presently applicable, these examples demonstrate the sensitivity of the formation keeping problem near the libration points.

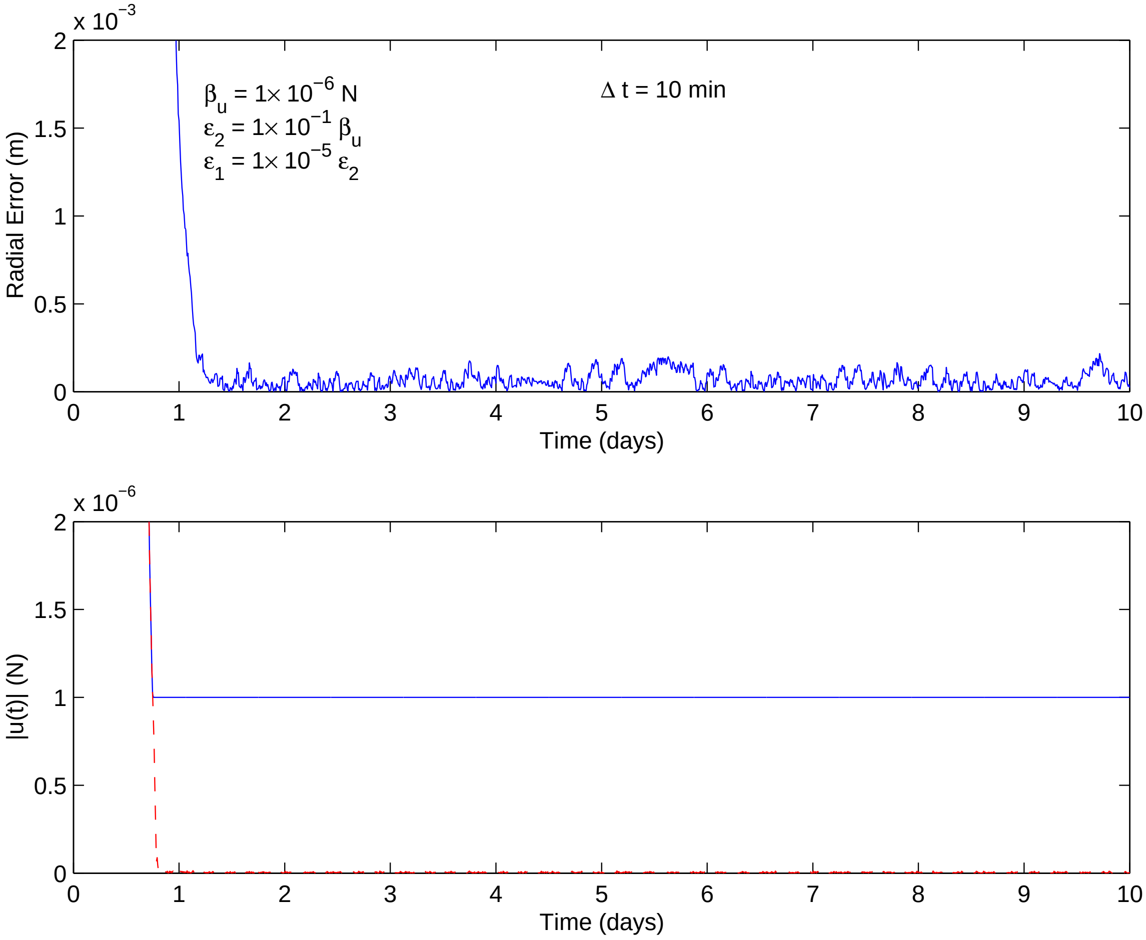

Figure 4.4. Linear State Feedback with Actuator Lower Bounds: Magnitude of Position Error for Example 2

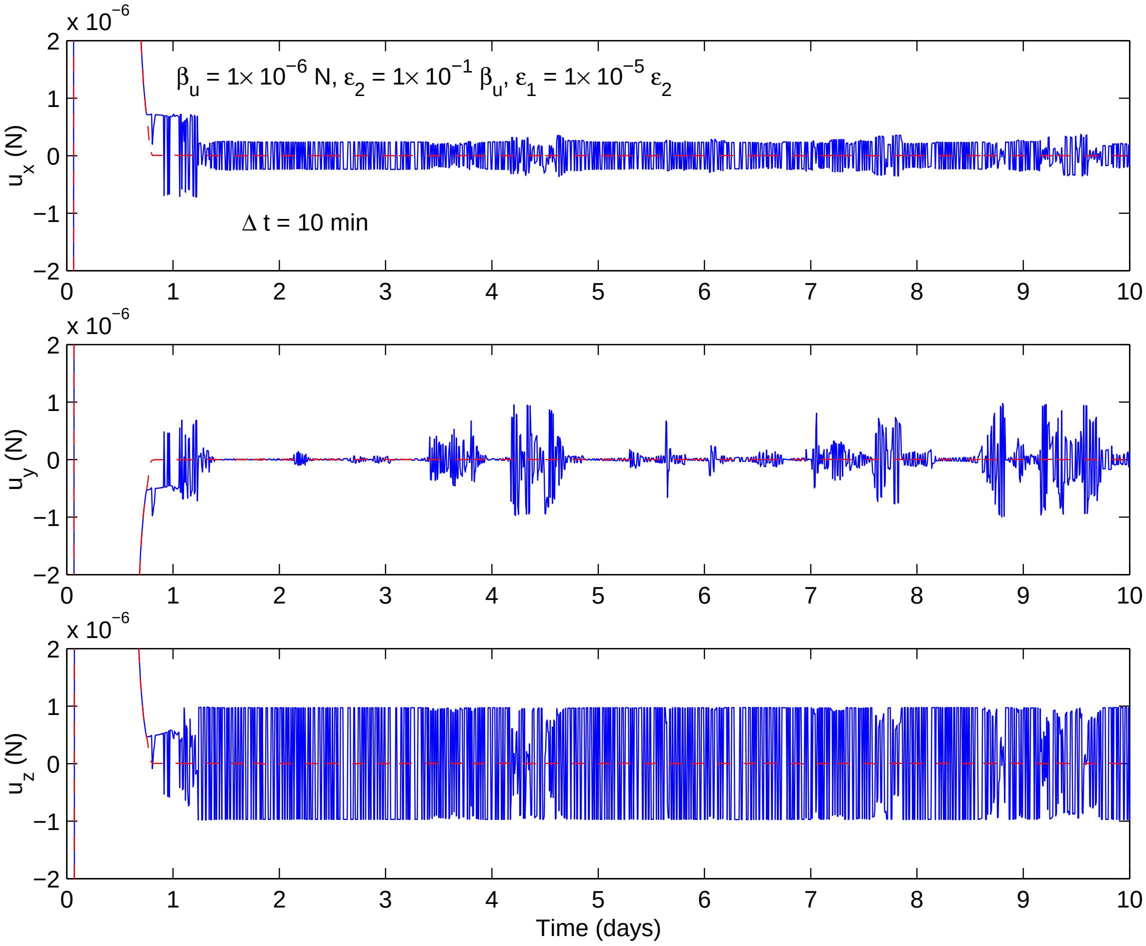

Figure 4.5. Linear State Feedback with Actuator Lower Bounds: Control Inputs Along Each Rotating Axis for Example 2

4.2 Linear Quadratic Regulator for Time-Varying Systems

Consider a general nonlinear vector field of the form

$$\dot{\bar{x}}(t) = \bar{f}(\bar{x}(t), \bar{u}(t)), \tag{4.15}$$

where $\bar{x} \in R^n$ is the state vector at time t, $\dot{\bar{x}}$ represents the time derivative of $\bar{x}$, $\bar{u} \in R^{n/2}$ is defined as the control acceleration vector, and $\bar{f} : U \to R^n$ is a smooth function defined on some subset $U \subseteq R^n$. Let $\bar{x}^\circ(t)$ denote some reference motion that satisfies the system in Equation (4.15) and $\bar{u}^\circ(t)$ represent the control effort required to maintain $\bar{x}^\circ(t)$. Linearization about this reference solution yields a system of the form

$$\delta\dot{\bar{x}}(t) = A(t)\,\delta\bar{x}(t) + B(t)\,\delta\bar{u}(t), \tag{4.16}$$

where $\delta\bar{x}$ and $\delta\bar{u}$ represent perturbations relative to $\bar{x}^\circ(t)$ and $\bar{u}^\circ(t)$, respectively. Consider the general quadratic cost function

$$\min J = \frac{1}{2}\int_{t_0}^{t_f} \left(\delta\bar{x}(t)^T Q\delta\bar{x}(t) + \delta\bar{u}(t)^T R\delta\bar{u}(t)\right) dt, \tag{4.17}$$

subject to the system in Equation (4.16) with initial conditions $\delta\bar{x}(t_0) = \delta\bar{x}_0$. The matrices Q and R represent the weighting on the state error and control effort, respectively, and are both symmetric positive definite. For simplicity, let Q and R be diagonal matrices. This implies that the individual state variable errors, and control accelerations, are decoupled. Since the cost function can be scaled by any constant without affecting the results, only the relative magnitudes of the elements of Q and R are important. Hence, in this study, R denotes the 3×3 identity matrix and Q, scaled relative to R, is defined as $Q = diag(Q_p, Q_p, Q_p, Q_v, Q_v, Q_v)$ where Q_p and Q_v are the position and velocity weights, respectively. The structure of this matrix places equal weighting on each position error as well as each velocity error.

As outlined in Bryson and Ho [45], application of the Euler Lagrange theorem to the system in Equations (4.17) and (4.16) yields the following optimality requirements,

$$\dot{\bar{\lambda}}(t) = -Q\bar{x}(t) - A(t)^T \bar{\lambda}(t)\,;\ \bar{\lambda}(t_f) = \bar{0}, \tag{4.18}$$

$$\bar{u} = -R^{-1}B(t)^T \bar{\lambda}(t)\,. \tag{4.19}$$

Consider a state feedback controller by defining $\bar{\lambda}(t) = P(t)\,\delta\bar{x}(t)$. Substitution of this transformation into Equation (4.18) yields the following Riccati matrix differential equation,

$$\dot{P}(t) = -A(t)^T P(t) - P(t)A(t) + P(t)B(t)R^{-1}B(t)^T P(t) - Q, \tag{4.20}$$

subject to $P(t_f) = 0_6$. Equations (4.20) and (4.15), represent a two-point boundary value problem with $(n{\times}n{+}n)$ first order ordinary differential equations. Obtaining an exact solution to this matrix equation is numerically inconvenient because it requires that the reference trajectory be integrated first, forward in time, from t_0 to t_f to evaluate $A(t)$ before integrating Equation (4.20) backwards from t_f to t_0. However, for application to the CR3BP, this difficulty can be avoided by exploiting the time invariance properties associated with the dynamical model. Consider the following time transformation,

$$\tau = t_f - t, \tag{4.21}$$

$$\frac{d}{dt} = -\frac{d}{d\tau}. \tag{4.22}$$

In the CR3BP, the linear system in Equation (4.16) is time invariant. Hence, for a given set of initial conditions, the initial time is of no consequence. Only the elapsed time is relevant. Consequently, introduce the following coordinate transformation,

$$z(\tau) = Gx(t)\,, \tag{4.23}$$

where G denotes a constant non-singular matrix. For the free response, where $\bar{u}(t) = \bar{0}$, the transformed state must also satisfy the differential equations,

$$\begin{aligned} \tfrac{dz(\tau)}{d\tau} &= A(\tau)\,z(\tau)\,, \\ -\tfrac{d(G\bar{x}(t))}{dt} &= A(t_f - t)\,G\bar{x}(t)\,, \\ \tfrac{d\bar{x}(t)}{dt} &= -G^{-1}A(t_f - t)\,G\bar{x}(t) = A(t)\,\bar{x}(t)\,. \end{aligned}$$

Hence,

$$A\left(t\right)=-G^{-1}A\left(t_f-t\right)G. \tag{4.24}$$

Equation (4.24) must be satisfied for all time. Thus,

$$A\left(t_f-t\right)=-G^{-1}A(t_f-(t_f-t))G=-G^{-1}A\left(t\right)G,$$

$$A\left(t\right)=-GA\left(t_f-t\right)G^{-1}. \tag{4.25}$$

For both Equations (4.24) and (4.25) to be satisfied, the matrix G must possess some special properties. In particular, $G^{-1}=G$, $G^2=I$, but $G\neq I$. Since G must be a diagonal matrix to satisfy these conditions it must also satisfy

$$G=G^T=G^{-1}=G^{-T}. \tag{4.26}$$

The diagonal matrix $G_{jj}=\left(-1\right)^{j-1}$ satisfies all of the stated requirements.

Substitution of the time transformation defined by Equations (4.21) and (4.25) into (4.20) yields

$$-\frac{dS\left(\tau\right)}{d\tau}=A\left(\tau\right)^TS\left(\tau\right)+S\left(\tau\right)A\left(\tau\right)+S\left(\tau\right)\tilde{B}\left(\tau\right)R^{-1}\tilde{B}\left(\tau\right)^TS\left(\tau\right)-\tilde{Q}, \tag{4.27}$$

where,

$$S\left(\tau\right)=G^{-1}P\left(t_f-\tau\right)G, \tag{4.28}$$

$$\tilde{B}\left(\tau\right)=G^{-1}B\left(t_f-\tau\right), \tag{4.29}$$

$$\tilde{Q}=G^{-1}QG. \tag{4.30}$$

The terminal boundary condition $P\left(t_f\right)=0$ implies that when $\tau=0$, $S\left(0\right)=0$. Since Equation (4.27) must be satisfied for all time, let $\tau=t$ such that

$$\dot{S}\left(t\right)=-A\left(t\right)^TS\left(t\right)-S\left(t\right)A\left(t\right)-S\left(t\right)\tilde{B}\left(t\right)R^{-1}\tilde{B}\left(t\right)^TS\left(t\right)+\tilde{Q}, \tag{4.31}$$

with $S\left(0\right)=0$. Equation (4.31) can be numerically integrated to time t_f along with the nonlinear equations of motion in Equation (4.15). Then, using Equation (4.28),

$$P\left(t_f-t\right)=GS\left(t\right)G^{-1}=G^{-1}S\left(t\right)G. \tag{4.32}$$

This yields the controller gain matrix

$$K\left(t_f - t\right) = -R^{-1} B\left(t\right)^T S\left(t\right) G. \tag{4.33}$$

The process of implementing the linear controller in the nonlinear model is decomposed into two steps. In the first step, the nonlinear system in Equation (4.15) is numerically integrated along with the matrix differential equation in Equation (4.31). These equations are subject to $\bar{x}\left(t_0\right) = \bar{x}^{\circ}(t_0)$ and $S\left(t_0\right) = 0$, respectively. The results are used to determine $K\left(t\right)$ which is stored, along with the corresponding time, for later implementation. The second step involves numerical integration of the perturbed nonlinear equations and, at each time step, application of the control accelerations associated with the corresponding $K\left(t\right)$ matrix. The integration step size is determined by the first integration since the gain matrix elements are accessed from memory at each time.

4.2.1 Transition to the Ephemeris Model

In the CR3BP, the equations of motion are invariant under time transformation. Hence, as previously demonstrated, it is possible to reduce the two-point boundary value problem to an initial value problem by appropriate choice of time transformation. However, this property is not applicable to the EPHEM model and so, once again, solving the formation keeping problem via LQR techniques requires the solution of a two-point boundary value problem. The simplest way to accomplish this task requires that the nominal solution be stored and later approximated on demand while solving the differential Riccati equation. The complete process is extremely computationally intensive, particularly when multiple spacecraft are to be considered. Furthermore, there is a certain degree of error introduced by the interpolating polynomials. Reducing this error requires small integration step sizes which further decrease the integration speed.

One of the observations deduced from the present analysis is that implementation of an LQR approach in the EPHEM model is ultimately unnecessary since numerical evidence, based on analysis performed in the CR3BP, suggests that both the LQR and IFL methods can yield essentially identical responses and control input histories. That is, the state error weighting elements, Q_p and Q_v, in the LQR controller can be selected to match the response of the IFL controller for a given ω_n. This is possible because both methods assumed that the error in one state is independent of the error in another. Since the resulting response is basically identical, the IFL controller is preferred to determine the control requirements for formations in the EPHEM model.

4.3 Input Feedback Linearization

Feedback linearization, as discussed in Slotine and Li [46], is a nonlinear control strategy that allows the designer to pre-specify the desired response characteristics. For instance, let

$$\dot{\chi}\left(t\right) = h\left(\chi\left(t\right)\right) + \upsilon\left(t\right), \tag{4.34}$$

where $\chi\left(t\right)$ represents the state at time t, $h(\chi)$ denotes some nonlinear function of χ, and $\upsilon(t)$ is the control input. In input feedback linearization, the control $\upsilon\left(t\right)$ is selected such that

$$\upsilon\left(t\right) = -h\left(\chi\left(t\right)\right) + \tilde{\upsilon}\left(t\right). \tag{4.35}$$

The control acceleration, $\tilde{\upsilon}\left(t\right)$, in Equation (4.35) is designed to be representative of the desired nominal motion, $\chi^{\circ}\left(t\right)$. For a critically damped response,

$$\tilde{\upsilon}\left(t\right) = \ddot{\chi}^{\circ} - 2\omega_n\left(\dot{\chi} - \dot{\chi}^{\circ}\right) - \omega_n^2\left(\chi - \chi^{\circ}\right). \tag{4.36}$$

Although canceling the nonlinear terms may, in general, lead to prohibitive control levels, the dynamical sensitivity characteristic of the region of space near the libration points creates an environment well suited to this particular approach.

An additional advantage of feedback linearization methods is that the mathematical development, and subsequent computational implementation, is simpler than that corresponding to an optimal control strategy. Of course, in practice, the physical construction of a nonlinear controller may be a daunting task, as discussed by Chen et al. [47]. This is particularly true for highly nonlinear dynamics such as those associated with the n-body problem. It is also important to note that any form of feedback linearization requires full-state feedback, one of the disadvantages of the approach. However, for formation flight, if accurate relative state information is available, this method can be a powerful tool.

4.3.1 Application of IFL Control: Inertially Fixed Formations

Let $(\bar{r}^{\circ}, \dot{\bar{r}}^{\circ})$ represent the nominal state vector corresponding to the deputy. The IFL control law is designed to follow a critically damped error response for the actual deputy relative state, $\bar{r}^{CD_i}$,

$$\ddot{\bar{r}}^{CD_i}(t) = \ddot{\bar{r}}^{\circ} - 2\omega_n(\dot{\bar{r}}^{CD_i} - \dot{\bar{r}}^{\circ}) - \omega_n^2(\bar{r}^{CD_i} - \bar{r}^{\circ}). \tag{4.37}$$

where ω_n denotes the natural frequency of the response. The control input required, then, to yield the desired response is determined by equating the right hand side of Equation (4.37) to that of the relative equation of motion in Equation (2.25). The resulting control law is determined as

$$\bar{u}_{D_i}(t) = -\Delta\bar{f}^{D_i} + \ddot{\bar{r}}^{\circ} - 2\omega_n(\dot{\bar{r}}^{CD_i} - \dot{\bar{r}}^{\circ}) - \omega_n^2(\bar{r}^{CD_i} - \bar{r}^{\circ}). \tag{4.38}$$

This method is successfully applied in both the CR3BP and the EPHEM model. In general, the IFL control approach offers several advantages over standard LQR techniques. First, this method does not rely on a priori knowledge of the controller gain matrix since it is determined directly from the nonlinear system rather than the linearized dynamics. Hence, storing the nominal trajectory and gain matrices is not required.

Furthermore, it is both conceptually and computationally simpler than LQR methods. This is an important advantage when working in the EPHEM model, where the time invariance properties are lost and the simplifications introduced in the previous section are no longer applicable.

Example: Formations Fixed Relative to the Rotating Frame

Consider a 5000 km two-spacecraft formation fixed relative to the rotating frame as defined in the CR3BP. Note that both LQR and IFL methods can be successfully applied to either the chief spacecraft orbit or the motion of the deputy in either the CR3BP or the ephemeris model. In this example, the line defining the formation is commanded to track the rotating y-axis at all times. Consistent with Figure 2.12, this type of formation represents the most cost effective baseline configuration. The response to an injection error defined by $\bar{e}\,(0) = (7, -5, 3.5)$ km and $\dot{\bar{e}}\,(0) = (1, -1, 1)$ m/sec appears in Figure 4.6 for both controllers. The top two plots in Figure 4.6 represent the response of the error dynamics in each state to the LQR controller, for a particular set of weighting matrices (Q and R). In contrast, the two plots at the bottom of Figure 4.6 demonstrate the error response corresponding to each state for a controller based on Input Feedback Linearization (IFL), as represented by Equation (4.38), for a non-dimensional frequency, ω_n, of 1250. Note that, in this example, both controllers yield good tracking characteristics at essentially the same cost, as is apparent in Figure 4.6. For the two time histories in Figure 4.6, a close-up view of the converged control acceleration components and of the associated net magnitudes, beyond the injection phase, is presented in Figure 4.7. Observe that, for a 5000 km nominal separation and a 1000 kg deputy vehicle, the thrust level required to enforce the desired configuration is, roughly, between 0.5 and 1.0 mN.

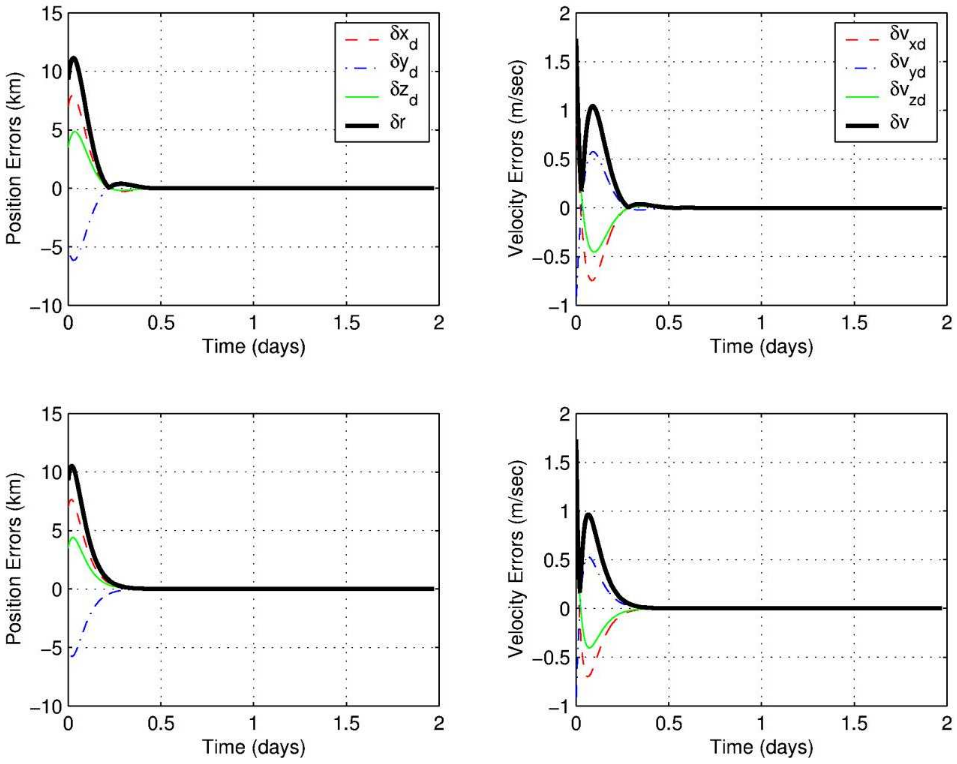

Figure 4.6. Sample LQR vs. IFL Error Response for Deputy S/C in a 5000 km Formation, Fixed Relative to the Rotating Frame (Over Six Months), Near a 2×10^5 km L_1 Halo Orbit

Although the results in Figure 4.6 reflect only the response to initial injection errors, the methodology can be extended to accomplish reconfigurations during flight. For instance, suppose the formation must reconfigure its relative separation every 20 days by 10 km. Application of the IFL approach yields the response presented in Figure 4.8. According to the control acceleration history in Figure 4.8, and beyond the initial injection error correction, each subsequent reconfiguration requires a maximum control input of 0.075 mm/sec^2. This is equivalent to 75 mN for a 1000 kg spacecraft. Once the solution has converged onto the desired configuration, the nominal control input ranges between 0.00043-0.00048 mm/sec^2, or 0.43 to 0.48 mN for the 1000 kg deputy. The reconfiguration can also be accomplished using the LQR controller.

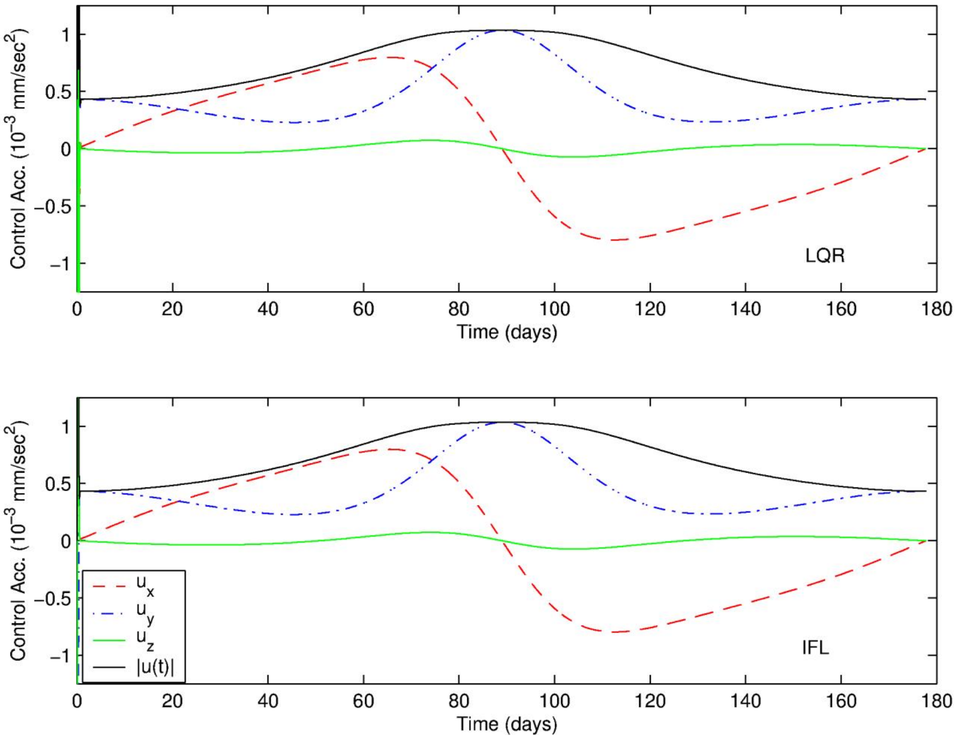

Figure 4.7. LQR vs. IFL Control Accelerations for Deputy S/C in a 5000 km Formation, Fixed Relative to the Rotating Frame (Over Six Months), Near a 2×10^5 km L_1 Halo Orbit

In comparing the LQR and feedback linearization results, the following information is notable. Clearly, it is possible to identify weighting matrices, Q and R, such that the LQR and IFL responses are nearly identical. However, the selection of the elements of these matrices is not necessarily trivial. In fact, the selection itself can be envisioned as an optimization problem. But, automating the selection process is also quite challenging. The goal of the above example is to obtain a very specific set of response characteristics. In the IFL analysis, a critically damped response is sought. Matching the LQR response to that of the IFL controller requires a very specific set of position and velocity weights. The appropriate ratio between the position and velocity weights is determined experimentally. Since the IFL approach eliminates the need for this determination, it offers another advantage over LQR.

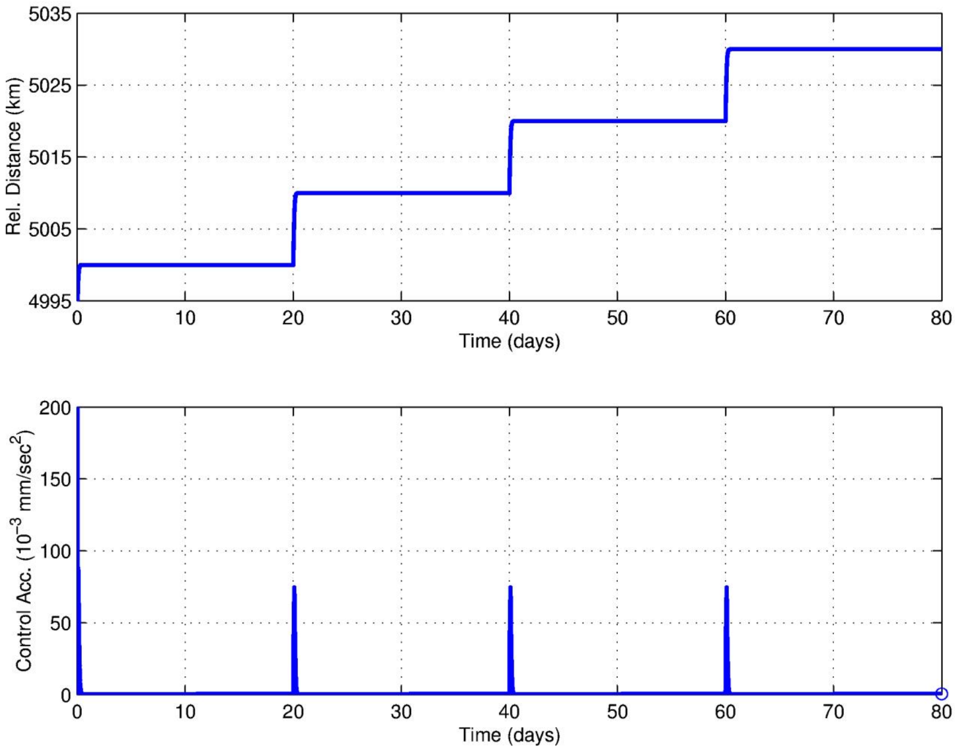

Figure 4.8. IFL Applied to Formation Reconfiguration

Example: Formations Fixed in the Inertial Frame

Formations fixed relative to inertial directions are just as effectively controlled by either of the two methods. Once again, let the reference halo orbit be characterized by $A_z = 2 \times 10^5$ km. Assume that the deputy is to follow the chief spacecraft as it evolves along the reference halo orbit over one revolution. The minimum cost configuration corresponds to the chief-deputy line aligned with the inertial Z-axis. A sample response to an initial injection error of $\bar{e}(0) = (7, -5, 3.5)$ km and $\dot{\bar{e}}(0) = (1, -1, 1)$ m/sec is presented in Figure 4.9. The nominal control input required to enforce this type of motion ranges between 0.0006 and 0.00125 mm/s^2, or 0.6-1.25 mN for a 1000 kg deputy vehicle.

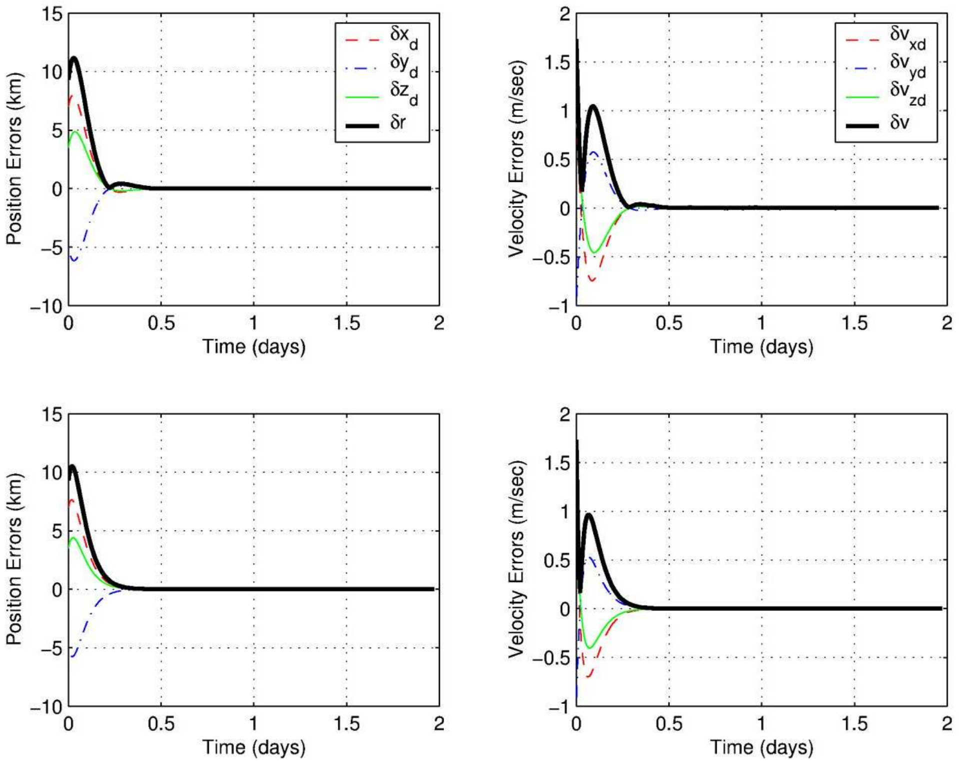

Figure 4.9. LQR vs. IFL Error Response for Deputy S/C in a 5000 km Formation, Fixed Relative to the Inertial Frame (Over Six Months), Near a 2×10^5 km L_1 Halo Orbit

4.4 Output Feedback Linearization

Both input and output feedback linearization methods require full-state feedback. However, the OFL controller design is far less constrained. That is, rather than specifying a nominal state vector, a quantity that is a function of the state vector may be the only function or constraint of interest. In output feedback linearization, the function (measured output) is differentiated q times until the control input appears explicitly in the expression. Then, similar to the IFL approach, the control law can be determined simply by specifying the desired dynamic response of the measured output.

4.4.1 Application of OFL Control: Fixed Range

Recall that the radial distance dynamics for the deputy spacecraft are governed by Equation (2.32),

$$\ddot{r} = \frac{\left(\Delta\bar{f}^{(D_i)} + \bar{u}_{D_i}\right)\cdot\bar{r}}{r} + \frac{{}^I\dot{\bar{r}}\cdot{}^I\dot{\bar{r}}}{r} - \frac{\dot{r}^2}{r}.$$

Define the measured system output as $y_1 = r$ and let r° and $\dot{r}^\circ$ denote the nominal range and range rate of the deputy spacecraft relative to the chief. The goal of the OFL controller is to determine a control vector $\bar{u}_{D_i}(t)$ that yields the desired output response, $r = r^\circ$ and $\dot{r}^\circ = 0$ for all time. Physically, this is equivalent to constraining the motion of the deputy to evolve along the surface of a nominal sphere, centered around the chief spacecraft. As long as the deputy remains on this surface the control goal is satisfied, regardless of the relative vehicle orientation.

It is apparent in Equation (2.32), the control appears explicitly in $\ddot{r}$ through the vector derivative $\ddot{\bar{r}} = \Delta\bar{f}^{(D_i)} + \bar{u}_{D_i}$. The desired response satisfies $\ddot{r} = g\left(\bar{r},\dot{\bar{r}}\right)$, where $g(\bar{r},\dot{\bar{r}})$ is a scalar function of the state, $\bar{r}$ and $\dot{\bar{r}}$, that is representative of the desired output response. In this investigation, a critically damped error response is sought,

$$g(\bar{r},\dot{\bar{r}}) = \ddot{r}^\circ - 2\omega_n(\dot{r} - \dot{r}^\circ) - \omega_n^2(r - r^\circ), \tag{4.39}$$

where ω_n is the natural frequency of the error response. Substituting Equation (4.39) into (2.32) yields

$$\bar{u}_{D_i}\cdot\bar{r} = h(\bar{r},\dot{\bar{r}}) = \left[g(\bar{r},\dot{\bar{r}})\sqrt{\bar{r}\cdot\bar{r}} + \frac{\left(\dot{\bar{r}}\cdot\bar{r}\right)^2}{\bar{r}\cdot\bar{r}} - \dot{\bar{r}}\cdot\dot{\bar{r}} - \Delta\bar{f}^{(D_i)}\cdot\bar{r}\right]. \tag{4.40}$$

The expression in Equation (4.40) represents one equation in three unknowns, i.e., the three control accelerations in the input vector $\bar{u}_{D_i}(t)$. Since no additional constraint equations are imposed, there are an infinite number of solutions that satisfy Equation (4.40). An immediately obvious solution to Equation (4.40) corresponds to a control history based solely on radial-axis inputs, termed here the “geometric” approach.

Table 4.1. Summary of Control Laws for Various Output Vector Definitions

Formulation	**Control Law**	$u_\theta(t)$	$u_h(t)$
$y_1 = r$	$\bar{u}_1(t) = \left\{ g_1(\bar{r}, \dot{\bar{r}}) - \frac{\dot{\bar{r}}\cdot\dot{\bar{r}}}{r} + \frac{\dot{r}^2}{r} - \frac{\Delta \bar{f}^{(D_i)}}{r} \right\} \hat{r}$	0	0
$y_2 = r$	$\bar{u}_2(t) = \left\{ \frac{g_2(\bar{r}, \dot{\bar{r}})}{r} - \frac{\dot{\bar{r}}\cdot\dot{\bar{r}}}{r^2} \right\} \bar{r} + \left(\frac{\dot{r}}{r}\right) \dot{\bar{r}} - \Delta \bar{f}^{(D_i)}$	$\dot{r}\dot{\theta} - f_\theta$	$-f_h$
$y_3 = r^2$	$\bar{u}_3(t) = \left\{ \frac{1}{2}\frac{g_3(\bar{r}, \dot{\bar{r}})}{r^2} - \frac{\dot{\bar{r}}\cdot\dot{\bar{r}}}{r^2} \right\} \bar{r} - \Delta \bar{f}^{(D_i)}$	$-f_\theta$	$-f_h$
$y_4 = \frac{1}{r}$	$\bar{u}_4(t) = \left\{ -r g_4(\bar{r}, \dot{\bar{r}}) - \frac{\dot{\bar{r}}\cdot\dot{\bar{r}}}{r^2} \right\} \bar{r} + 3\left(\frac{\dot{r}}{r}\right) \dot{\bar{r}} - \Delta \bar{f}^{(D_i)}$	$3\dot{r}\dot{\theta} - f_\theta$	$-f_h$

That is, since $\bar{u}_{D_i} \cdot \bar{r} = |\bar{r}||\bar{u}_{D_i}| \cos\theta$, where θ represents the angle between $\bar{u}_{D_i}$ and $\bar{r}$, it is obvious that $\bar{u}_{D_i} = \{h\,(\bar{r}, \dot{\bar{r}})/r\}\,\hat{r}$ is a solution to Equation (4.40). Although this particular solution satisfies the control goal, there are no guarantees or expectations of optimality. In fact, this control law can lead to absurdly high formation keeping costs depending on the initial state of the deputy vehicle.

Alternate solutions can be obtained by factoring $h(\bar{r}, \dot{\bar{r}})$ as a function of $\bar{r}$ and solving explicitly for $\bar{u}_{D_i}(t)$. Table 4.1 summarizes the results of this approach for outputs of the form $y_2 = r$, $y_3 = r^2$, and $y_4 = r^{-1}$. The target responses for each case are

$$g_1(\bar{r}, \dot{\bar{r}}) = -2\omega_n\left(\dot{r} - \dot{r}^\circ\right) - \omega_n^2\left(r - r^\circ\right), \tag{4.41}$$

$$g_2(\bar{r}, \dot{\bar{r}}) = g_1(\bar{r}, \dot{\bar{r}}), \tag{4.42}$$

$$g_3(\bar{r}, \dot{\bar{r}}) = -4\omega_n r\dot{r} - \omega_n^2\left(r^2 - r^{\circ 2}\right), \tag{4.43}$$

$$g_4(\bar{r}, \dot{\bar{r}}) = 2\omega_n\frac{\dot{r}}{r^2} - \omega_n^2\left(\frac{1}{r} - \frac{1}{r^\circ}\right). \tag{4.44}$$

The geometric approach, discussed previously, is associated with y_1, the first line in Table 4.1. Each of the outputs listed in the first column of Table 4.1 lead to different control laws that produce vastly different costs. For instance, $\bar{u}_1(t)$ and $\bar{u}_3(t)$, in Table 4.1, yield a total integrated ΔV, over 180 days, in excess of 16,400 m/sec while $\bar{u}_4(t)$ only requires approximately 50 m/sec.

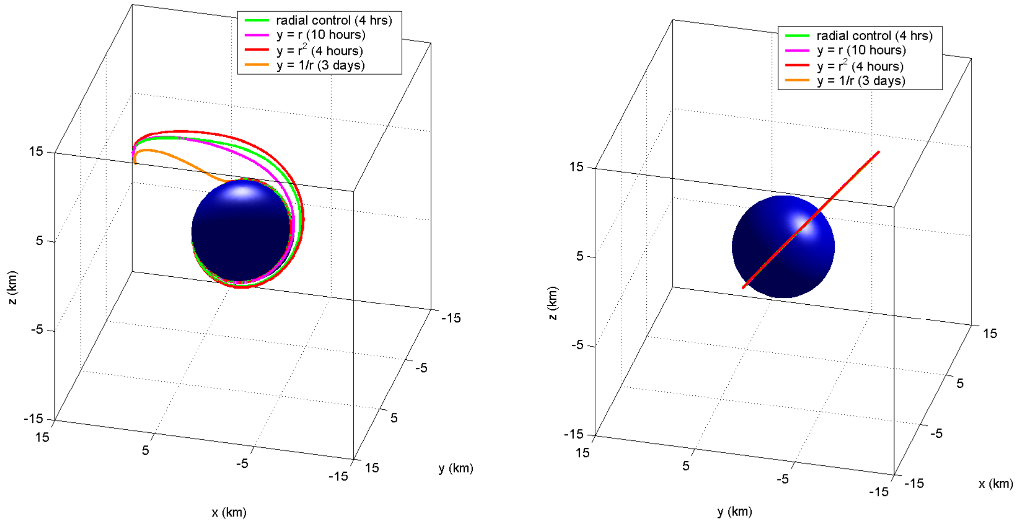

Figure 4.10. OFL Control of Spherical Formations (EPHEM Model)

In turn, each case is associated with a unique dynamical response, as observed from Figure 4.10. There are four trajectories illustrated in Figure 4.10. Each trajectory shares a common initial state, relative to the chief spacecraft (origin), defined by $\bar{r} = 12\hat{X} - 5\hat{Y} + 3\hat{Z}$ km and $\dot{\bar{r}} = \hat{X} - \hat{Y} + \hat{Z}$ m/sec. As observed in Figure 4.10, the deputy spacecraft still evolves onto and along the surface of a sphere, but the manner in which this is accomplished varies according to the control law. To better understand these differences, consider, briefly, the instantaneous rotating frame formed by the unit vectors $\hat{r}$, $\hat{\theta}$, and $\hat{h}$, previously defined in Equations (2.33)-(2.35).

At any given time, the angular momentum vector provides information about the instantaneous relative orbital plane of the deputy vehicle ($\hat{h}$) as well as its rotation rate ($\dot{\theta}$) about $\hat{h}$. The rate of change of the relative angular momentum vector can be expressed in terms of this rotating coordinate system as

$$ {}^{I}\dot{\bar{h}} = \bar{r} \times {}^{I}\ddot{\bar{r}} = r\left(\Delta f_{\theta} + u_{\theta}\right)\hat{h} - r\left(\Delta f_{h} + u_{h}\right)\hat{\theta}, \tag{4.45} $$

where Δf_θ, Δf_h, u_θ, and u_h denote the components of $\Delta\bar{f}^{(D_i)}$ and $\bar{u}_{D_i}$ along the $\hat{\theta}$ and $\hat{h}$ directions, respectively.

The associated unit normal vector, $\hat{h} = \bar{h}\left(\bar{h}^T\bar{h}\right)^{-1/2}$, varies with time as follows,

$$\frac{{}^I d\hat{h}}{dt} = -\frac{r\left(\Delta f_h + u_h\right)}{h}\hat{\theta}. \tag{4.46}$$

Thus, the plane of motion is preserved, and completely determined by the relative initial state, if $u_h + \Delta f_h = 0$. The last two columns in Table 4.1 summarize the $\hat{\theta}$ and $\hat{h}$ components of the control inputs, $\bar{u}_1(t)$-$\bar{u}_4(t)$. It is apparent, from Table 4.1 and Equation (4.46), that the plane of motion is preserved for the last three entries in Table 4.1. Also, since $h = \left|\bar{h}\right| = r^2\dot{\theta}$, the rotation rate $\dot{\theta}$ is further determined by u_θ. To better demonstrate these observations, consider the u_θ and u_h components from each formulation in Table 4.1. Substitution of these components into Equation (2.44) leads to the following results:

- Case 1: $\ddot{\theta} = \frac{\Delta f_\theta - 2\dot{r}\dot{\theta}}{r}$.

  Since $u_\theta = u_h = 0$, neither the angular momentum vector, $\bar{h} = h\hat{h}$, nor the angular acceleration, $\ddot{\theta}$, are ever constant. Naturally, the plane of motion is not preserved.

- Case 2: $\ddot{\theta} = \frac{-\dot{r}\dot{\theta}}{r}$.

  In this case, $u_\theta + \Delta f_\theta = \dot{r}\dot{\theta}$. Hence, $\bar{h} = h\hat{h}$, is not constant. However, $\ddot{\theta} \to 0$ as $\dot{r} \to 0$. Thus, both h and $\dot{\theta}$ converge to some limiting constant value as $r \to r^\circ$. The plane of motion is also preserved since $u_h + \Delta f_h = 0$.

- Case 3: $\ddot{\theta} = \frac{-2\dot{r}\dot{\theta}}{r}$.

  Here, $u_\theta + \Delta f_\theta = 0$ and $u_h + \Delta f_h = 0$, thus, $\bar{h}$ is constant and completely specified by the initial state of the deputy before the controller is activated. Accordingly, the angular acceleration $\ddot{\theta} \to 0$ as $\dot{r} \to 0$. Thus, $\dot{\theta}$ converges to some limiting constant value as $r \to r^\circ$.

- Case 4: $\ddot{\theta} = \frac{\dot{r}\dot{\theta}}{r}$.

  In this case, $\bar{h} = h\hat{h}$ is not constant since $u_\theta + \Delta f_\theta = 3\dot{r}\dot{\theta}$. Nonetheless, $\ddot{\theta} \to 0$ as $\dot{r} \to 0$. Thus, both h and $\dot{\theta}$ converge to some limiting constant value as $r \to r^\circ$. The plane of motion is still preserved since $u_h + \Delta f_h = 0$.

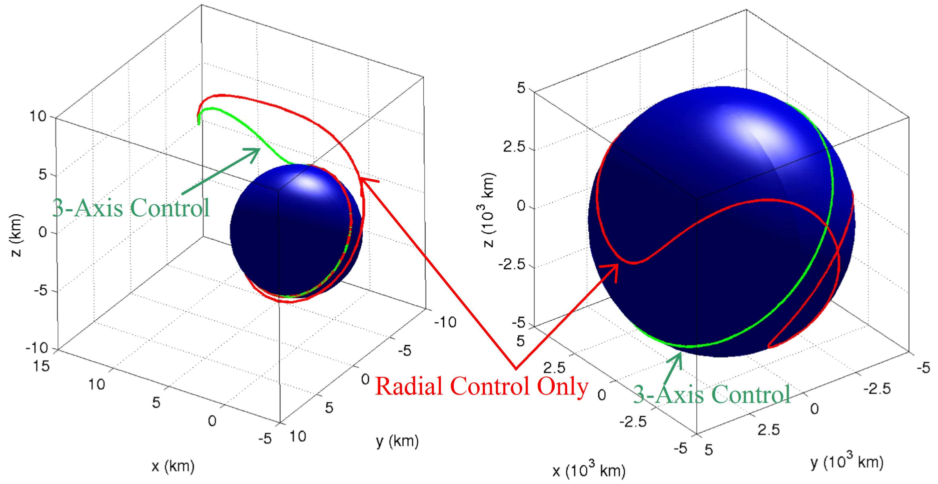

(a) (b)

Figure 4.11. Impact of Relative Orbit Size on Controlled Path of Deputy S/C

Note, for the case that employs radial axis inputs, if the nominal relative separation is small, it may appear that the solution converges onto a plane, though small deviations are present. Recall that if $u_h = u_\theta = 0$, then $\dot{\bar{h}} = r(\Delta f_\theta \hat{h} - \Delta f_h \hat{\theta})$. When the chief and deputy vehicles are close, r is small but Δf_θ and Δf_h are much smaller. However, as r increases the force differentials also increase. It is then that the angular momentum vector deviations are most apparent. The deviations in the actual path of the deputy are visible for nominal separations on the order of hundreds or thousands of kilometers, as observed from the sample cases in Figure 4.11. The blue sphere in the figure represents the nominal surface. In Figure 4.11(a), the nominal distance is 5 km (the radius of the nominal sphere) as compared to 5000 km for the plot in Figure 4.11(b). Each trajectory in Figure 4.11(a) is associated with an initial state characterized by $\bar{r}\,(0) = \begin{bmatrix} 12 & -5 & 3 \end{bmatrix}$ km and ${}^{I}\dot{\bar{r}}\,(0) = \begin{bmatrix} 1 & -1 & 1 \end{bmatrix}$ m/sec. The trajectories in Figure 4.11(b), are associated with the initial state $\bar{r}\,(0) = \begin{bmatrix} 5007 & -5 & 3 \end{bmatrix}$ km and ${}^{I}\dot{\bar{r}}\,(0) = \begin{bmatrix} 1 & -1 & 1 \end{bmatrix}$ m/sec. Both figures include two separate curves evolving onto the nominal sphere. The green path is associated with the $\bar{u}_4$ controller in Table 4.1, while the red curve corresponds to $\bar{u}_1$.

Though numerical evidence may at times appear to suggest that each controller is converging onto the same orbital plane, as is apparent from Figure 4.11(a), the theoretical proof is evidence that radial axis inputs alone do not allow for this type of solution. This is evident from Figure 4.11(b).

4.4.2 Application of OFL Control: Fixed Range and Rotation Rate

Recall, from Chapter 2, that the relative equations of motion can be rewritten in terms of an instantaneous relative rotating frame defined by unit vectors $\hat{r}$, $\hat{\theta}$ and $\hat{h}$. At each point in time, these vectors are directly determined from Equations (2.33)-(2.35). In terms of this set of unit vectors, the relative equations of motion that govern the radial distance and rotation rate dynamics are derived and appear in Equations (2.37) and (2.41). As a result of this formulation, one equation of constraint, Equation (2.45), is imposed on the $\hat{h}$ component of the control input, $u_h = -\Delta f_h$, where $\Delta f_h = \Delta \bar{f}^{(D_i)} \cdot \hat{h}$ and $u_h = \bar{u}_{D_i} \cdot \hat{h}$. The resulting system of equations can be rewritten as

$$\begin{aligned} \ddot{r} &= \Delta f_r + u_r + r\dot{\theta}^2 = g_r(\bar{r}, \dot{\bar{r}}), && (4.47) \\ r\ddot{\theta} &= \Delta f_\theta + u_\theta - 2\dot{r}\dot{\theta} = r g_\theta(\bar{r}, \dot{\bar{r}}), && (4.48) \\ 0 &= \Delta f_h + u_h. && (4.49) \end{aligned}$$

where $g_r(\bar{r}, \dot{\bar{r}})$ represents the desired radial response and $g_\theta(\bar{r}, \dot{\bar{r}})$ defines the nominal rotation rate dynamics. Once again, a critically damped error response, associated with natural frequency ω_n, is specified for the radial distance. However, for the rotation rate ($\dot{\theta}$), an exponentially decaying error response ($\delta\dot{\theta}$) is selected, $\delta\dot{\theta} = \delta\dot{\theta}_0 e^{-k\omega_n t}$. The quantity $\delta\dot{\theta}_0$ represents the initial error in $\dot{\theta}$ relative to the nominal rate, $\dot{\theta}^\circ$. The constant k is simply a scale factor to control the rate of decay of θ towards the nominal value. The desired rotation rate dynamics are described by

$$\ddot{\theta} = \ddot{\theta}^\circ - k\omega_n(\dot{\theta} - \dot{\theta}^\circ). \tag{4.50}$$

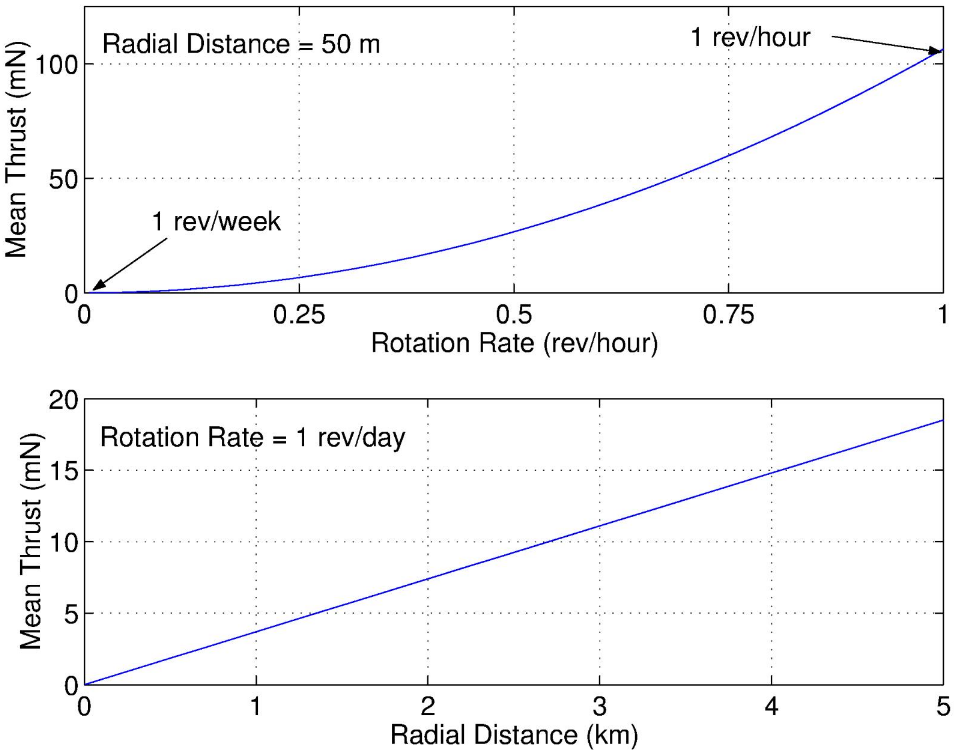

Figure 4.12. Impact of Commanded Radial Distance and Spin Rate on Formation Keeping Costs

The control inputs required to achieve the overall target response, in both r and $\dot{\theta}$, are subsequently determined to be of the form

$$u_r = g_r(\bar{r}, \dot{\bar{r}}) - r\dot{\theta}^2 - \Delta f_r, \tag{4.51}$$

$$u_\theta = r g_\theta(\bar{r}, \dot{\bar{r}}) + 2\dot{r}\dot{\theta} - \Delta f_\theta, \tag{4.52}$$

$$u_h = -\Delta f_h. \tag{4.53}$$

Using this type of control law, it is possible to determine how the formation keeping cost varies both as a function of the commanded relative separation and the commanded rotation rate. Of course, Equation (4.49) guarantees that the plane of motion is entirely determined by the relative state of the deputy before the controller is activated and remains fixed. The associated trends in the cost appear in Figure 4.12 in terms of the mean thrust required to enforce the formation.

Note, from Figure 4.12, that the cost increases quadratically with increasing rotation rate and linearly with the separation that is commanded between the chief and deputy vehicles. For a nominal separation of 50 meters, commanding the deputy to spin at one revolution per hour, about the chief spacecraft, requires over 100 mN of thrust, for a 700 kg vehicle. The mean thrust drops to 6.7 mN if the deputy vehicle is to nominally orbit the chief spacecraft once every 4 hours. The thrust levels continue to drop down to 0.19 mN for one revolution a day. If one revolution per day is required, a 500 meter separation raises the mean thrust to 18 mN. Though the plane of motion is not affected by this type of control approach, activating the controller at the appropriate time, or biasing the initial velocity, may be sufficient to achieve the desired orbital plane. Overall, the control strategy is conceptually simple and numerically efficient for implementation in the EPHEM model.

A sample implementation of the control law in Equations (4.51)-(4.53) is presented in Figure 4.13. In this example, the chief spacecraft is assumed to evolve along the Lissajous trajectory presented in the lower right of Figure 2.11. The nominal deputy motion is defined by a relative separation of 5 km between the chief and deputy vehicles. The mass of each vehicle is assumed to be 700 kg. The relative initial state of the deputy is defined by $\bar{r}\,(0) = \begin{bmatrix} 12 & -5 & 3 \end{bmatrix}$ km and $\dot{\bar{r}}\,(0) = \begin{bmatrix} 1 & -1 & 1 \end{bmatrix}$ m/sec. Two curves appear in Figure 4.13, one corresponds to $\dot{\theta}^{\circ} = 1$ rev/day and the other to $\dot{\theta}^{\circ} = 1$ rev /6 hours. The response of the deputy in configuration space is plotted in the left figure. As expected, both solutions converge onto the same plane orbiting on the nominal sphere. The plot on the right side in Figure 4.13 represents the converged thrust profile, as determined from Equations (4.51)-(4.53).

Clearly, not all formation flight missions may benefit from this type of spherical formation control. For instance, MAXIM requires that the relative state of each deputy vehicle remain fixed, inertially. This particular formation also requires formation tolerances on the order of micro-meters. In this case, forcing the deputies to rotate (i.e., orbit) the chief spacecraft does not represent a feasible option. However, missions like TPF may be able to take advantage of this particular approach.

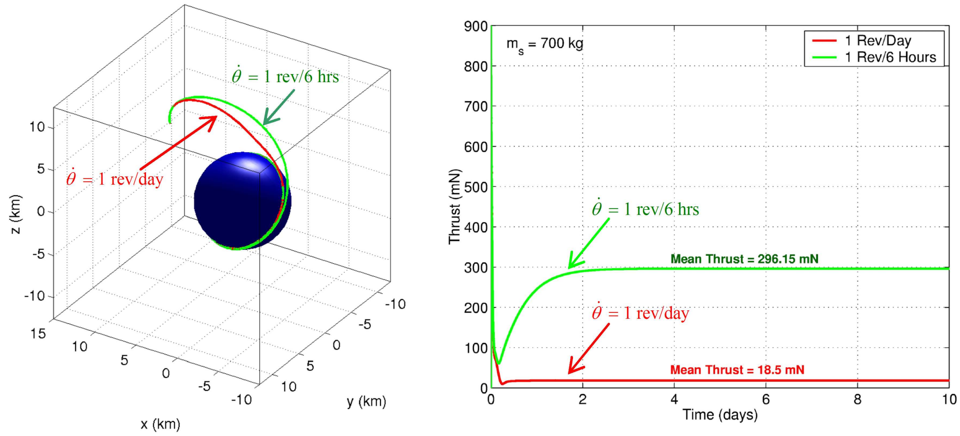

Figure 4.13. OFL Control of Radial Distance and Rotation Rate

4.5 Aspherical Formations

Consider a multi-spacecraft formation where the chief vehicle evolves along a quasi-periodic Lissajous trajectory near L_1 or L_2, as determined in the EPHEM model. It is specified that the deputy vehicles in the formation follow the chief such that their relative motion evolves along the surface of a paraboloid that is inertially fixed in orientation. Constraining the deputies onto a surface, at all times, minimizes the probability of collisions during formation reconfigurations. Note, then, that the same goal may be accomplished with other surfaces as well (i.e., conical, hyperboloid, etc.). For the present formulation, the chief spacecraft and the nadir of the paraboloid define the focal line of the formation. Maintenance of a constant distance between the chief vehicle and the nadir of the paraboloid is the first objective of the controller. The second requirement is that the motion of all deputies, even during reconfigurations, is constrained to evolve along the surface of the paraboloid. To accomplish these goals, it is first necessary to define a suitable parameterization for the formation surface. To facilitate the derivations, consider Figure 4.14.

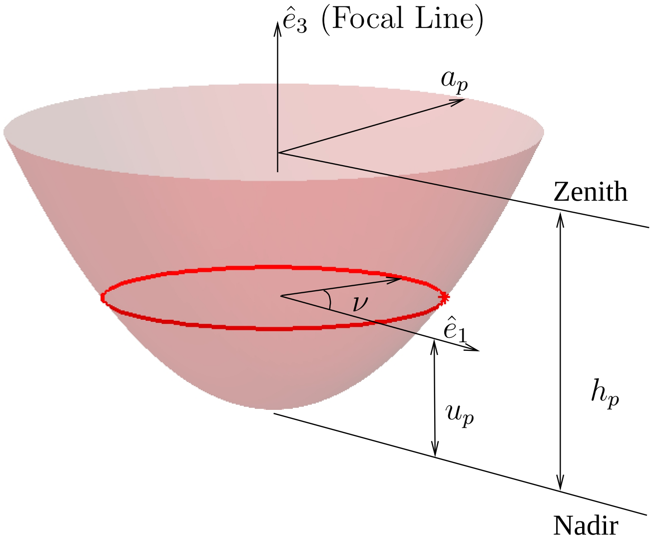

Figure 4.14. Parametrization of a Paraboloid

The paraboloid in Figure 4.14 is defined in an inertial frame (E) described in terms of the unit vectors $\hat{e}_1$, $\hat{e}_2$, and $\hat{e}_3$. The orientation of this frame, relative to the ephemeris inertial frame (I), is defined by the azimuth (α) and elevation (δ) of the focal line relative to the inertial frame (I) unit vectors $\hat{X}$, $\hat{Y}$, and $\hat{Z}$. This is better visualized in Figure 4.15, where the unit vector $\hat{e}_3$ is directed from the chief vehicle to the nadir of the nominal paraboloid. This direction is representative of the focal line of the formation. The "height" of any given deputy vehicle along this surface, measured relative to the nadir point, is defined by u_p where $0 \leq u_p \leq h_p$ and h_p denotes the maximum allowable height along the paraboloid surface. The radius at the zenith of the paraboloid ($u_p = h_p$) is denoted by the variable a_p. The unit vector $\hat{e}_1$, defined as $\hat{e}_1 = \hat{Z} \times \hat{e}_3 \Big/ \left|\hat{Z} \times \hat{e}_3\right|$, is simply a reference direction for the measurement of the angular position (ν) along the surface in Figure 4.14. Of course, $\hat{e}_2 = \hat{e}_3 \times \hat{e}_1$ completes the right handed inertial triad.

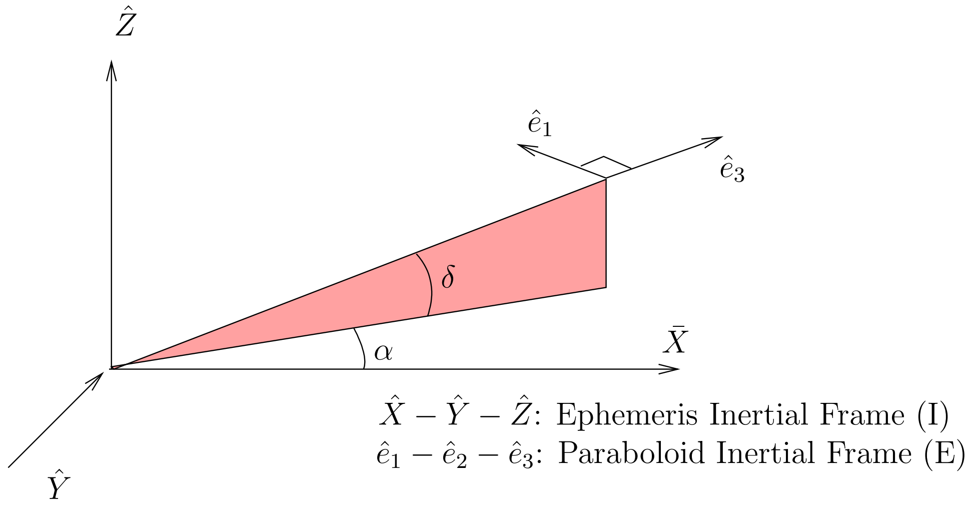

Figure 4.15. Formation Focal Line Orientation

The variables ν and u_p completely specify the position of a deputy vehicle along the formation surface in Figure 4.14. In the focal frame (E), the position vector from the nadir to any given deputy vehicle along the surface of the paraboloid is defined as

$$\bar{p}\left(u_p,\nu\right)=\left(a_p\sqrt{u_p/h_p}\cos\nu\right)\hat{e}_1+\left(a_p\sqrt{u_p/h_p}\sin\nu\right)\hat{e}_2+u_p\hat{e}_3. \tag{4.54}$$

The desired position of the nadir, relative to the chief spacecraft, is specified as $\bar{q}=q\hat{e}_3$. The equation of motion in Equation (2.26) is associated with the inertial frame (I). The nominal relative position vector can also be written in terms of E-frame coordinates as $\bar{\rho}_E=\bar{q}+\bar{p}\left(u_p,\nu\right)$. In this alternate inertial frame, the nominal relative acceleration vector, ${}^E\ddot{\bar{\rho}}_E$, can be expressed as

$${}^E\ddot{\bar{\rho}}_E={}^E\ddot{\bar{q}}+\left(\bar{p}_{u_pu_p}\dot{u}_p+\bar{p}_{u_p\nu}\dot{v}\right)\dot{u}_p+\bar{p}_{u_p}\ddot{u}_p+\left(\bar{p}_{\nu u_p}\dot{u}_p+\bar{p}_{\nu\nu}\dot{\nu}\right)\dot{\nu}+\bar{p}_{\nu}\ddot{\nu}, \tag{4.55}$$

where $\bar{p}_{u_p}$, $\bar{p}_{u_pu_p}$, $\bar{p}_{u_p\nu}$, $\bar{p}_{\nu u_p}$, $\bar{p}_{\nu}$, and $\bar{p}_{\nu\nu}$ denote the first and second partial derivatives of $\bar{p}$ with respect to u_p and ν, respectively. The scalar rates $\dot{u}_p$ and $\dot{\nu}$ represent the climb rate and the rotation rate along the nominal surface. Since both the E and I frames are inertial, the accelerations in Equations (2.26) and (4.55) are related through the orientation matrix ${}^IC^E$ such that ${}^I\ddot{\bar{\rho}}_I={}^IC^{E\,E}\ddot{\bar{\rho}}_E$. The j^{th} column of the matrix ${}^IC^E$ corresponds to the unit vector $\hat{e}_j$, for $j=1-3$, as defined in Figure 4.15.

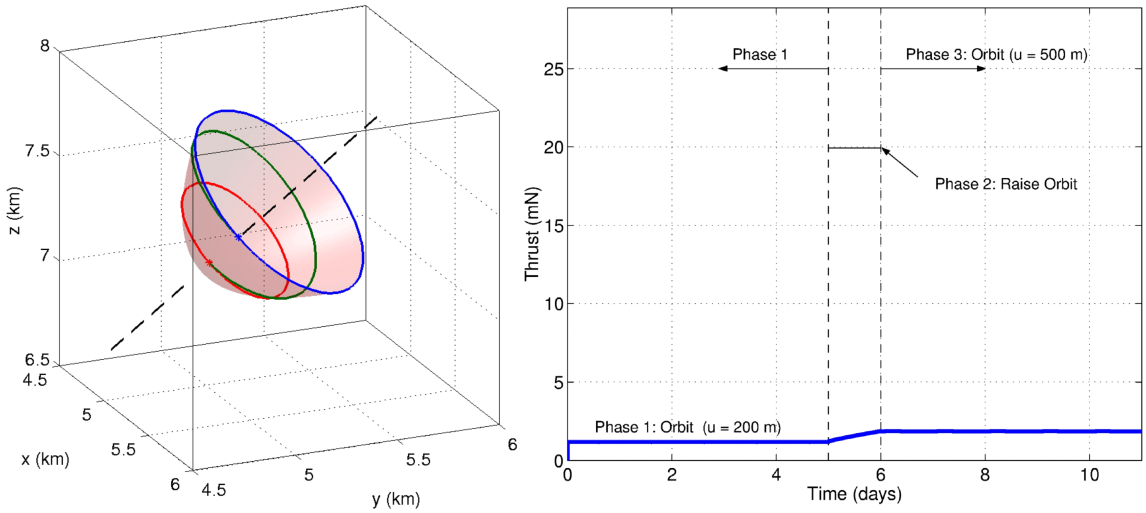

Figure 4.16. Nominal Geometry and Thrust Requirements for a Sample Parabolic Formation

In order for the nominal motion to satisfy Equation (4.55) precisely, the control law must be applied continuously and is determined as

$$\bar{u}^{\circ}_{D_i}(t) = {}^{I}C^{E}\left[{}^{e}\ddot{\bar{q}} + \left(\bar{p}_{u_p}\ddot{u}_p + \bar{p}_{\nu}\ddot{\nu}\right) + \left(\bar{p}_{u_p u_p}\dot{u}_p^2 + 2\bar{p}_{u_p\nu}\dot{u}_p\dot{\nu} + \bar{p}_{\nu\nu}\dot{\nu}^2\right)\right] - \Delta\bar{f}^{(D_i)^{\circ}}. \quad (4.56)$$

Consider a formation characterized by $\bar{q} = (10\text{ km})\,\hat{e}_3$, $h_p = 500$ m, $a_p = 500$ m. Let the focal line be oriented such that $\alpha = 0°$, and $\delta = 45°$. Each vehicle in the formation is to complete one revolution along the surface once a day, $\dot{\nu} = 1$ rev/day. The nominal motion of one of the vehicles is initially described by $u_p = 200$ meters such that $\dot{u}_p = \ddot{u}_p = 0$ and $\ddot{\nu} = 0$. After 5 days, the vehicle's nominal path must be reconfigured, along the paraboloid, such that $\dot{\nu}$ and $\dot{u}_p$ remain constant. The climb rate, $\dot{u}_p$, is specified such that, after 1 day, the vehicle "height" is raised to 500 meters relative to the nadir of the paraboloid, a 300 meter climb relative to the initial orbit. The nominal control law in Equation (4.56) leads to the desired motion in Figure 4.16.

In this Figure, the off-center circular orbit closest to the nadir (red) represents the initial nominal motion over a span of 5 days. The green spiral defines the reconfiguration segment over the next day while the highest circular orbit (blue) denotes the converged solution over the remaining 5 days. The associated nominal thrust profile reveals that a range of 1.4 to 2.0 mN of continuous thrust is required to enforce the formation, including the reconfiguration, in the absence of external perturbations.

4.5.1 OFL Control and Parabolic Formations

The control design presented above is associated with nominal formation keeping. That is, assuming the vehicles are already in the desired configuration, Equation (4.56) establishes the thrust profile necessary to enforce the desired formation continuously. In the example illustrated in Figure 4.16, each phase is computed separately and independently from the other. For instance, the end state of Phase 1, plus the necessary impulsive ΔV, is used as the initial state to compute the trajectory associated with Phase 2. A similar approach is employed to determine the trajectory associated with Phase 3. Hence, the above solution addresses neither the deployment nor the reconfiguration of an actual continuous solution. To address this aspect, output feedback linearization techniques are applied.

In prior investigations, input/output feedback linearization (IFL/OFL) is successfully applied to achieve the desired formation keeping goals. The earlier OFL examples are based on a tracking scheme involving relative distance and rotation rate. Hence, the number of variables to track is less than the number of available control inputs. As such, there are an infinite number of solutions available that satisfy the goals for the controller. In the present case, a parabolic configuration requires the tracking of three variables: $u_p(t)$, $q(t)$, and $\nu(t)$. That is, the distance to the nadir, the height of the vehicle along the paraboloid surface and the orientation time history along the surface.

To demonstrate the application of an OFL controller to this type of configuration, it is necessary to establish a set of expressions relating the state variables (and control inputs) to the tracked quantities. For instance, recall that any vector expressed in terms of focal frame coordinates, E, has an equivalent representation in the ephemeris inertial frame, I, through the transformation matrix ${}^{I}C^{E}$. Hence, the relative deputy position vector may be expressed

$$\bar{\rho}_I = {}^{I}C^{E}\bar{\rho}_E = \left[\begin{array}{ccc} \tilde{x} & \tilde{y} & \tilde{z} \end{array}\right]^T, \tag{4.57}$$

where the symbol '$\sim$' above each variable indicates that the measure numbers are associated with the focal frame (E) of the paraboloid. These measure numbers are related to the paraboloid parameters in Figure 4.14 as follows,

$$\tilde{x} = a_p\sqrt{u_p/h_p}\cos\nu, \tag{4.58}$$

$$\tilde{y} = a_p\sqrt{u_p/h_p}\sin\nu, \tag{4.59}$$

$$\tilde{z} = q + u_p. \tag{4.60}$$

Squaring and then adding Equations (4.58)-(4.59) reveals that

$$u_p = \left(h_p/a_p^2\right)\left[\tilde{x}^2 + \tilde{y}^2\right], \tag{4.61}$$

while dividing Equation (4.59) by Equation (4.58) yields

$$\tan\nu = \left(\tilde{y}/\tilde{x}\right). \tag{4.62}$$

Furthermore, Equation (4.60) indicates that

$$q = \tilde{z} - \left(h_p/a_p^2\right)\left[\tilde{x}^2 + \tilde{y}^2\right]. \tag{4.63}$$

The associated rates are defined by differentiating Equations (4.61)-(4.63) with respect to time, i.e.,

$$\dot{u}_p = \frac{2h_p}{a_p^2}\left(\tilde{x}\dot{\tilde{x}} + \tilde{y}\dot{\tilde{y}}\right), \tag{4.64}$$

$$\dot{q} = \dot{\tilde{z}} - \frac{2h_p}{a_p^2}\left(\tilde{x}\dot{\tilde{x}} + \tilde{y}\dot{\tilde{y}}\right), \tag{4.65}$$

$$\dot{\nu} = \frac{\tilde{x}\dot{\tilde{y}} - \tilde{y}\dot{\tilde{x}}}{(\tilde{x}^2 + \tilde{y}^2)}. \tag{4.66}$$

With these expressions, it is possible to identify relationships between the control inputs ($\tilde{u}_x$, $\tilde{u}_y$, $\tilde{u}_z$) and the tracked variables (u_p, q, $\dot{\nu}$). These relationships are obtained by differentiating Equations (4.64)-(4.66) with respect to time. Differentiation is straightforward and ultimately suggests that,

$$\ddot{u}_p = \frac{2h_p}{a_p^2}\left(\dot{\tilde{x}}^2 + \dot{\tilde{y}}^2 + \tilde{x}(\Delta\tilde{f}_x + \tilde{u}_x) + \tilde{y}(\Delta\tilde{f}_y + \tilde{u}_y)\right), \tag{4.67}$$

$$\ddot{q} = (\Delta\tilde{f}_z + \tilde{u}_z) - \frac{2h_p}{a_p^2}\left(\dot{\tilde{x}}^2 + \dot{\tilde{y}}^2 + \tilde{x}(\Delta\tilde{f}_x + \tilde{u}_x) + \tilde{y}(\Delta\tilde{f}_y + \tilde{u}_y)\right), \tag{4.68}$$

$$\ddot{\nu} = \frac{-2(\tilde{x}\dot{\tilde{x}} + \tilde{y}\dot{\tilde{y}})(\tilde{x}\dot{\tilde{y}} - \tilde{y}\dot{\tilde{x}})}{(\tilde{x}^2 + \tilde{y}^2)^2} + \frac{\tilde{x}(\Delta\tilde{f}_y + \tilde{u}_y) - \tilde{y}(\Delta\tilde{f}_x + \tilde{u}_x)}{(\tilde{x}^2 + \tilde{y}^2)}. \tag{4.69}$$

Equations (4.67)-(4.69) represent the actual response of each of these variables to some arbitrary control input. The desired response, in this case, is specified as critically damped error dynamics for the distance elements u_p and q, while an exponentially decaying error response is sought for $\dot{\nu}$. These constraints are mathematically represented by

$$\ddot{u}_p = \ddot{u}_p^\circ - 2\omega_n(\dot{u}_p - \dot{u}_p^\circ) - \omega_n^2(u_p - u_p^\circ) = g_{u_p}(u_p, \dot{u}_p), \tag{4.70}$$

$$\ddot{q} = \ddot{q}^\circ - 2\omega_n(\dot{q} - \dot{q}^\circ) - \omega_n^2(q - q^\circ) = g_q(q, \dot{q}), \tag{4.71}$$

$$\ddot{\nu} = \ddot{\nu}^\circ - k\omega_n(\dot{\nu} - \dot{\nu}^\circ) = g_{\dot{\nu}}(\dot{\nu}). \tag{4.72}$$

In Equations (4.70)-(4.72), ω_n represents the natural frequency of the desired response, k is an arbitrary scale factor, and the superscript "$\circ$" denotes nominal values. Equations (4.67)-(4.69) are then equated to Equations (4.70)-(4.72) to obtain an exact solution for the control $\tilde{u}_x$, $\tilde{u}_y$, and $\tilde{u}_z$ to produce the desired response.

The first step in identifying this solution is to isolate the control inputs as a function of the spacecraft states and the desired nominal response. This leads to

$$g_{u_p}\left(u_p, \dot{u}_p\right) - \frac{2h_p}{a_p^2}\left(\dot{\tilde{x}}^2 + \dot{\tilde{y}}^2 + \tilde{x}\Delta\tilde{f}_x + \tilde{y}\Delta\tilde{f}_y\right) = \frac{2h_p}{a_p^2}(\tilde{x}\tilde{u}_x + \tilde{y}\tilde{u}_y), \tag{4.73}$$

$$g_q\left(q, \dot{q}\right) + \frac{2h_p}{a_p^2}\left(\dot{\tilde{x}}^2 + \dot{\tilde{y}}^2 + \tilde{x}\Delta\tilde{f}_x + \tilde{y}\Delta\tilde{f}_y\right) - \Delta\tilde{f}_z = -\frac{2h_p}{a_p^2}(\tilde{x}\tilde{u}_x + \tilde{y}\tilde{u}_y) + \tilde{u}_z, \tag{4.74}$$

$$g_{\dot{\nu}}\left(\dot{\nu}\right) + 2\frac{\left(\tilde{x}\dot{\tilde{x}} + \tilde{y}\dot{\tilde{y}}\right)\left(\tilde{x}\dot{\tilde{y}} - \tilde{y}\dot{\tilde{x}}\right)}{\left(\tilde{x}^2 + \tilde{y}^2\right)^2} + \frac{\left(\tilde{y}\Delta\tilde{f}_x - \tilde{x}\Delta\tilde{f}_y\right)}{\left(\tilde{x}^2 + \tilde{y}^2\right)} = \frac{\tilde{x}\tilde{u}_y}{\left(\tilde{x}^2 + \tilde{y}^2\right)} - \frac{\tilde{y}\tilde{u}_x}{\left(\tilde{x}^2 + \tilde{y}^2\right)}. \tag{4.75}$$

In Equations (4.73)-(4.75), recall that the '$\sim$' represents quantities associated with the focal frame (E) of the paraboloid. Hence, $\tilde{u} = {}^E C^I \bar{u} = [\ \tilde{u}_x \quad \tilde{u}_y \quad \tilde{u}_z\ ]^T$ represents the transformed control input vector. Similarly, $\Delta\tilde{f} = {}^E C^I \Delta\bar{f}^{(D_i)} = [\ \Delta\tilde{f}_x \quad \Delta\tilde{f}_y \quad \Delta\tilde{f}_z\ ]^T$ and $\tilde{r} = {}^E C^I \bar{r} = [\ \tilde{x} \quad \tilde{y} \quad \tilde{z}\ ]^T$ denote the differential force and the radial distance with respect to the chief spacecraft, in terms of focal frame coordinates, respectively.

The control law may now be determined, in terms of focal frame coordinates (E), by solving the system of equations in Equations (4.73)-(4.75). To simplify the form of the solution, let $\alpha_x = 2h_p\tilde{x}/a_p^2$, $\alpha_y = 2h_p\tilde{y}/a_p^2$, $\beta_x = \tilde{x}/\left(\tilde{x}^2 + \tilde{y}^2\right)$, and $\beta_y = \tilde{y}/\left(\tilde{x}^2 + \tilde{y}^2\right)$. Furthermore, let the left hand side of Equations (4.73)-(4.75) be represented by G_{u_p}, G_q, and $G_{\dot{\nu}}$, respectively. Then, the commanded control input is expressed

$$\tilde{u}_x = \frac{\left(\beta_x G_{u_p} - \alpha_y G_{\dot{\nu}}\right)}{\left(\alpha_x\beta_x + \alpha_y\beta_y\right)}, \tag{4.76}$$

$$\tilde{u}_y = \frac{\left(\beta_y G_{u_p} + \alpha_x G_{\dot{\nu}}\right)}{\left(\beta_x\alpha_x + \beta_y\alpha_y\right)}, \tag{4.77}$$

$$\tilde{u}_z = G_{u_p} + G_q. \tag{4.78}$$

Note, the above control law is singular if the deputy crosses the focal line ($\hat{e}_3$), that is, $\tilde{x} = \tilde{y} = 0$. In most cases, this does not present a significant issue, however, because once the deputy is on the surface of the paraboloid this condition is never met. This singularity can only occur while the deputy is being driven onto the surface during the injection phase. To circumvent this difficulty, it is only necessary to allow the vehicle to coast away from this point before reactivating the controller.

However, some missions, or for certain phases of a particular mission, an alternate formulation may be necessary. One such formulation that removes this singularity, is presented at the end of this chapter.

In implementing Equations (4.76)-(4.78) in the EPHEM model, the integration of each vehicle proceeds separately in an Earth centered inertial frame (I). The relative state of the deputy, $(\bar{\rho}_I, {}^I\dot{\bar{\rho}}_I)$, with respect to the chief is computed from these Earth centered states. These quantities are then transformed into the focal frame (E) via $\bar{\rho}_E = {}^E C^I \bar{\rho}_I$ and ${}^E\dot{\bar{\rho}}_E = {}^E C^{II}\dot{\bar{\rho}}_I$, where $\bar{\rho}_E = (\tilde{x}, \tilde{y}, \tilde{z})$ and ${}^E\dot{\bar{\rho}}_E = (\dot{\tilde{x}}, \dot{\tilde{y}}, \dot{\tilde{z}})$. The results of this transformation are substituted into Equations (4.61)-(4.66) to determine the values of the quantities to be tracked as well as the necessary control accelerations, as computed from Equations (4.76)-(4.78).

To demonstrate the application of this approach, consider the nominal sample scenario previously introduced and plotted in Figure 4.16. An injection error is introduced such that the initial relative state of the deputy, with respect to the chief spacecraft, is characterized by $\bar{r} = \left(4.6\hat{X} + 4.3\hat{Y} + 6.934\hat{Z}\right)$ km with a relative velocity defined by $\dot{\bar{r}} = 0.05\hat{X} - 0.05\hat{Y} - 0.05\hat{Z}$ m/sec. This particular initial state is arbitrarily selected to facilitate the visualization process. For any arbitrary initial state, the controller should drive the vehicles in the formation to the initial configuration, then reconfigure at the appropriate time. Once deployed, this evolution is to proceed along the surface of the paraboloid. Application of this controller results in the trajectory illustrated in Figure 4.17. The resulting path is decomposed into three segments. The segment highlighted in orange represents the injection phase as well as the initial orbit phase, for $u_p = 200$ m. The green segment denotes the reconfiguration phase, characterized by $\dot{u}_p = 300$ meters/day. The last segment, in blue, is the final phase associated with $u_p = 500$ m. The thrust profile associated with this solution appears in Figure 4.18. Comparing Figure 4.16 to Figure 4.18, it is clear that the OFL controller converges to the nominal control except for the initial correction that is necessary for injection into the nominal configuration. The thrust levels range from 25mN during injection to 1-2 mN for orbit maintenance.

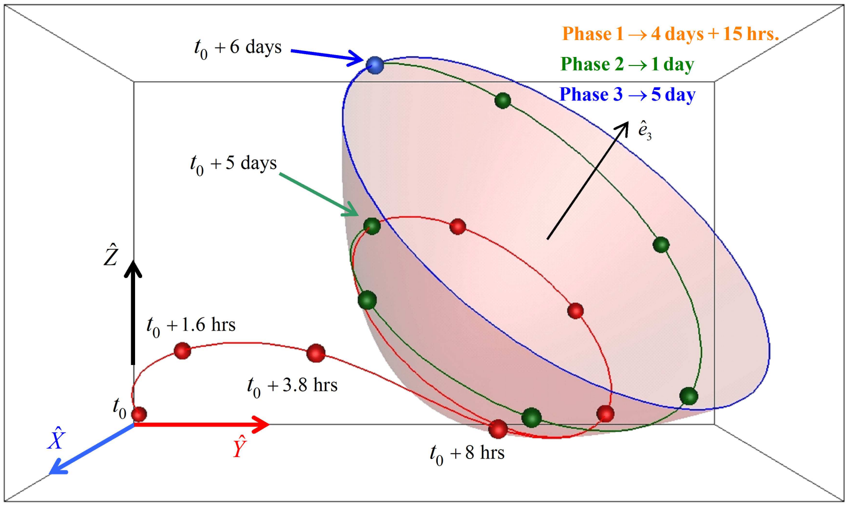

Figure 4.17. OFL Controlled Parabolic Formation

Note that the maximum thrust amplitude will vary according to the response frequency that is specified. Also, though both the nominal and actual thrust profiles, appear to converge onto constant segments, there is an oscillation on the order of 0.003 mN during the orbit phase at $u_p = 200$ (last part of Phase 1) m and $u_p = 500$ m (Phase 3).

4.5.2 Applications to MAXIM

Parabolic configurations represent one possible formation keeping approach for missions like MAXIM [48, 49] and TPF [50]. During the science collection phase of these missions, as presently envisioned, the relative position of the vehicles in the formation must be maintained to within high levels of accuracy, potentially on the order of 10^{-6} μm for MAXIM. Achieving these levels of accuracy requires at least nearly continuous control, particularly near the libration points where the dynamical response is extremely sensitive to small perturbations.

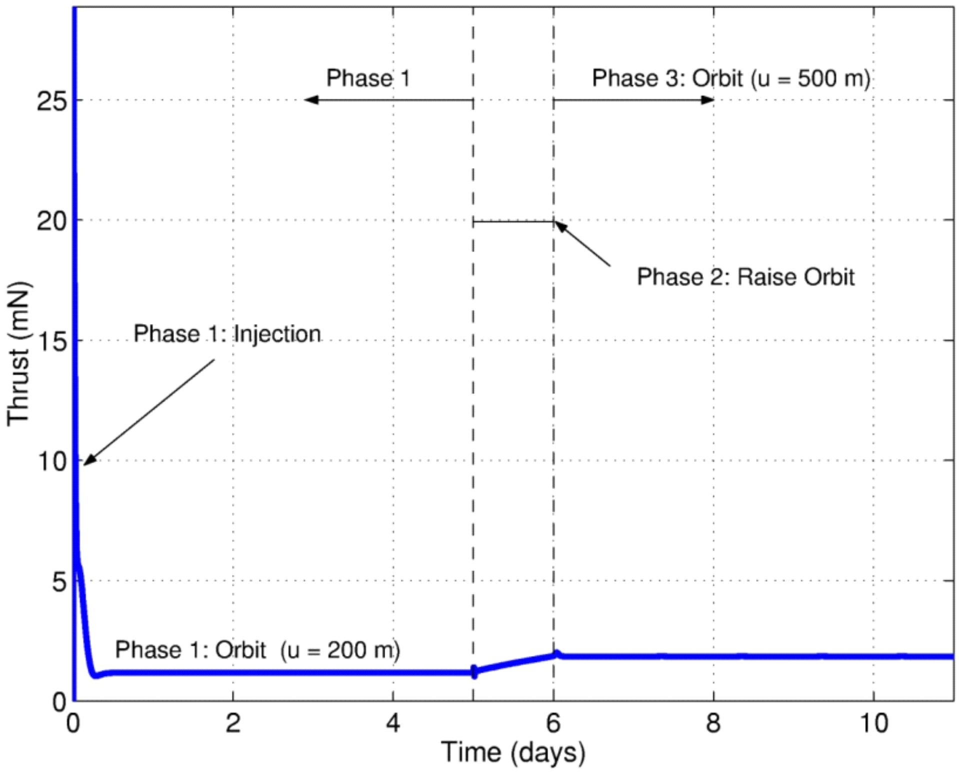

Figure 4.18. Thrust Profile for OFL Controlled Parabolic Formation

As presently formulated, the control law presented in Equations (4.76)-(4.78) may or may not be applicable to all phases of a given mission. For instance, the preliminary design for the MAXIM Pathfinder mission [48, 49] consists of two phases, pictorially represented in Figure 4.19. During the initial phase, the formation consists of two vehicles, the detector and the hub spacecraft. For modeling purposes, the hub spacecraft is defined as the chief vehicle while the detector represents the deputy. The chief-deputy line, in this case, is controlled to remain aligned with the target (i.e., some predetermined point in space). The nominal distance between the chief and deputy vehicles is specified as 200 km.

Although the hub spacecraft, during phase one, appears as a single vehicle, it is in fact a conglomerate of seven vehicles. During the second phase, also illustrated in Figure 4.19, six of these vehicles, termed free flyers, separate from the hub, the central vehicle in the conglomerate.

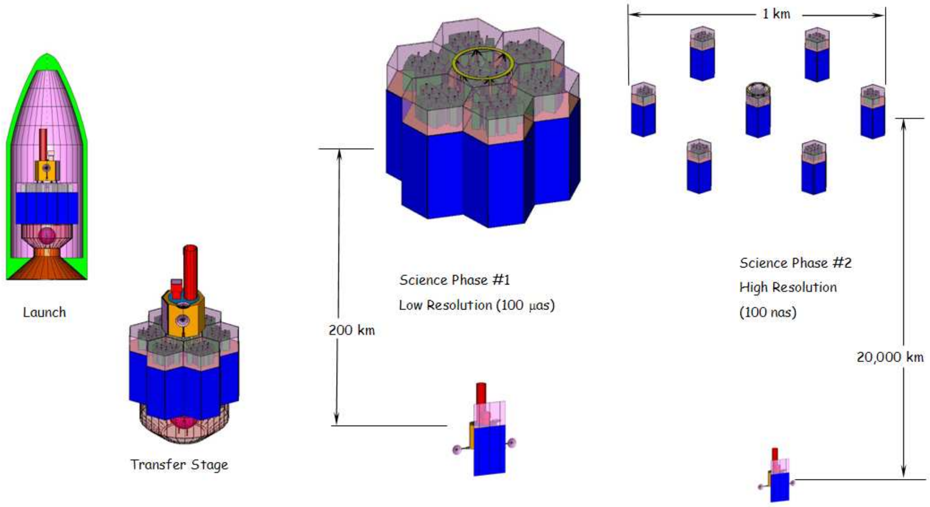

Figure 4.19. MAXIM Pathfinder Preliminary Design: Mission Sequence

Then, the free flyers are reconfigured to maintain some pre-specified position relative to the hub. Hence, a total of seven deputies (one detector and six free flyers) are commanded to follow the chief spacecraft (hub) as it evolves along its nominal path. The controlled formation evolution during phase two is best visualized from Figure 4.20. In the present interpretation of the nominal mission, the chief spacecraft (hub) evolves along a "halo"-like Lissajous trajectory near L_2, as determined in the EPHEM model. The detector spacecraft is nominally positioned 20,000 km behind the hub and along the line of sight. Finally, the six free flyers are located 500 meters away and evenly distributed around the hub on a plane perpendicular to the line of sight.

Since the transition from phase one to phase two places all the deputy vehicles close to or on the line of sight, the control law in Equations (4.76)-(4.78) is immediately singular. Certainly, if the hub spacecraft is defined as the chief vehicle, formation keeping for the detector cannot rely on the parabolic formulation. That is because the nominal position of the detector is along the line of sight to the target. However, the free flyers can take advantage of this formulation once they have separated from the hub. The transition from phase one to phase two can be accomplished, however, with a simpler IFL approach that is suitable for all stages of the mission.

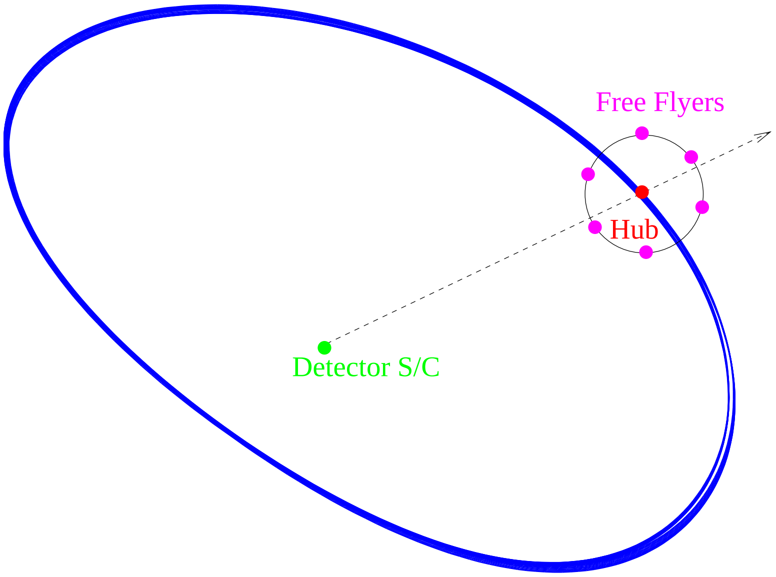

Figure 4.20. Sample Evolution of MAXIM Formation

To formulate a more appropriate control law, let $\hat{w}$ denote the line of sight measured from the hub (chief) to the target. Then, $\hat{u} = \hat{Z} \times \hat{w}/||\hat{Z} \times \hat{w}||$ and $\hat{v} = \hat{w} \times \hat{u}$. In this frame, the position vector from the hub to the i^{th} deputy vehicle, either one of the six free flyers or the detector, is specified as $\bar{r}^{HD_i} = \tilde{x}_i\hat{w} + \tilde{y}_i\hat{u} + \tilde{z}_i\hat{v}$. Let ρ_i denote the nominal distance from the hub to i^{th} deputy. Furthermore, let ν_i and ϵ_i represent the azimuth and elevation of the i^{th} deputy relative to the $\hat{u}$-$\hat{v}$ plane, as defined in Figure 4.21.

Consistent with Equation (2.25), the relative equations of motion for the i^{th} deputy may be specified as

$$ {}^{I}\ddot{\bar{r}}_{I}^{HD_i} = \Delta\bar{f}^{(D_i)} + \bar{u}_{D_i}(t). \tag{4.79}$$

An IFL control law may then be developed to target either $(\tilde{x}^o, \tilde{y}^\circ, \tilde{z}^\circ)$, or $(\rho^\circ, \nu^\circ, \epsilon^\circ)$, where the superscript "$\circ$" denotes evaluation along the nominal path.

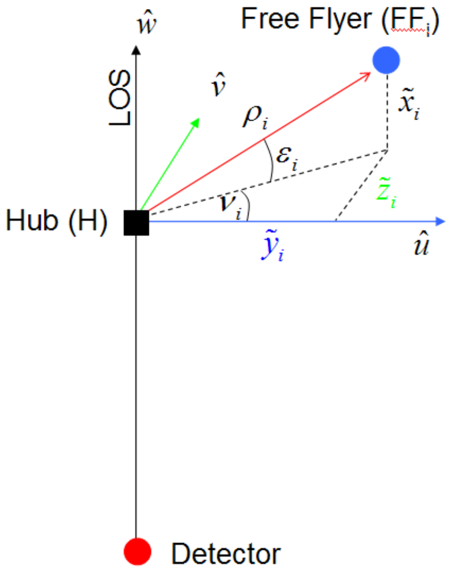

Figure 4.21. MAXIM Preliminary Design: Relative Coordinate System

MAXIM: IFL Method 1

For each deputy vehicle, a critically damped state error response is achieved by specifying

$$\bar{u}_{D_i}(t) = -\Delta\bar{f}^{(D_i)} +^I C^U \left(-2\omega_n \left({}^U\dot{\bar{r}}_U^{HD_i} - \dot{\bar{r}}_U^\circ\right) - \omega_n^2 \left(\bar{r}_U^{HD_i} - \bar{r}_U^\circ\right)\right), \tag{4.80}$$

where ${}^I C^U$ represents the transformation matrix between the U-frame, defined by $\hat{w}$, $\hat{u}$, and $\hat{v}$, and the ephemeris inertial frame, I. Also note that $\bar{r}_U^\circ$ and $\dot{\bar{r}}_U^\circ$ are the nominal position and velocity vectors in terms of U-frame coordinates. It is important to note that, in this form of the IFL approach, each position variable is controlled independently. Hence, it is possible for the deputy spacecraft to follow an almost straight line to the nominal position. This is precisely the type of motion that the parabolic formulation sought to prevent to minimize the probability of collisions. However, as previously determined, this formulation is not suitable for MAXIM's transition from phase one to phase two.

It is also important to note that, once the free flyers separate from the hub, it is possible to simply let them drift away from the hub, naturally, and, once a certain distance is achieved, the parabolic control law previously determined may be safely implemented. Still, an IFL approach is better suited for the detector spacecraft since the associated nominal position lies along the line of sight.

MAXIM: IFL Method 2

An IFL control law may also be formulated to achieve some nominal response in ρ, ν, and ϵ instead. Ultimately, the general form of the control law in Equation (4.80) does not actually change, only the terms in this expression are affected. To illustrate this, let the radial and angular position of the deputy spacecraft, relative to the U-frame, be specified by

$$\rho_i = \sqrt{\tilde{x}_i^2 + \tilde{y}_i^2 + \tilde{z}_i^2}, \tag{4.81}$$

$$\nu_i = tan^{-1}\left(\frac{\tilde{z}_i}{\tilde{y}_i}\right), \tag{4.82}$$

$$\epsilon_i = tan^{-1}\left(\frac{\tilde{x}_i}{\sqrt{\tilde{y}_i^2 + \tilde{z}_i^2}}\right), \tag{4.83}$$

while the associated rates are determined as

$$\dot{\rho}_i = \frac{\bar{r}_U^{HD_i} \cdot {}^U\dot{\bar{r}}_U^{HD_i}}{\rho_i}, \tag{4.84}$$

$$\dot{\nu}_i = \frac{\dot{\tilde{z}}_i\tilde{y}_i - \dot{\tilde{y}}_i\tilde{z}_i}{\tilde{y}_i^2 + \tilde{z}_i^2}, \tag{4.85}$$

$$\dot{\epsilon}_i = \frac{\dot{\tilde{x}}_i\left(\tilde{y}_i^2 + \tilde{z}_i^2\right) - \left(\tilde{y}_i\dot{\tilde{y}}_i + \tilde{z}_i\dot{\tilde{z}}_i\right)\tilde{x}_i}{\left(\dot{\tilde{x}}_i\left(\tilde{y}_i^2 + \tilde{z}_i^2\right) - \left(\tilde{y}_i\dot{\tilde{y}}_i + \tilde{z}_i\dot{\tilde{z}}_i\right)\tilde{x}_i\right)\sqrt{\tilde{y}_i^2 + \tilde{z}_i^2}}. \tag{4.86}$$

Let the radial and angular accelerations be specified to follow a critically damped error response characterized by

$$\ddot{\rho}_i = \ddot{\rho}_i^\circ - 2\omega_n\left(\dot{\rho}_i - \dot{\rho}_i^\circ\right) - \omega_n^2\left(\rho_i - \rho_i^\circ\right), \tag{4.87}$$

$$\ddot{\epsilon}_i = \ddot{\epsilon}_i^\circ - 2\omega_n\left(\dot{\epsilon}_i - \dot{\epsilon}_i^\circ\right) - \omega_n^2\left(\epsilon_i - \epsilon_i^\circ\right), \tag{4.88}$$

$$\ddot{\nu}_i = \ddot{\nu}_i^\circ - 2\omega_n\left(\dot{\nu}_i - \dot{\nu}_i^\circ\right) - \omega_n^2\left(\nu_i - \nu_i^\circ\right). \tag{4.89}$$

If the nominal motion of the deputies is one fixed relative to the U-frame, then $\ddot{\rho}_i^\circ = 0$ and $\ddot{\nu}_i^\circ = \ddot{\epsilon}_i^\circ = 0$. Similarly, $\dot{\rho}_i^\circ = 0$ and $\dot{\nu}_i^\circ = \dot{\epsilon}_i^\circ = 0$. The cartesian accelerations, in terms of U-frame coordinates, associated with these radial and angular accelerations are subsequently identified as

$$\begin{aligned} \ddot{\tilde{y}}_i &= \ddot{\rho}_i C_{\epsilon_i} C_{\nu_i} - 2\dot{\rho}_i \dot{\epsilon}_i S_{\epsilon_i} C_{\nu_i} - 2\dot{\rho}_i \dot{\nu}_i C_{\epsilon_i} S_{\nu_i} - \rho_i \dot{\epsilon}_i^2 C_{\epsilon_i} C_{\nu_i} - \rho_i \ddot{\epsilon}_i S_{\epsilon_i} C_{\nu_i} \\ &+ 2\rho_i \dot{\epsilon}_i \dot{\nu}_i S_{\epsilon_i} S_{\nu_i} - \rho_i \dot{\nu}_i^2 C_{\epsilon_i} C_{\nu_i} - \rho_i \ddot{\nu}_i C_{\epsilon_i} S_{\nu_i}, \end{aligned} \tag{4.90}$$

$$\begin{aligned} \ddot{\tilde{z}}_i &= \ddot{\rho}_i C_{\epsilon_i} S_{\nu_i} - 2\dot{\rho}_i \dot{\epsilon}_i S_{\epsilon_i} S_{\nu_i} + 2\dot{\rho}_i \dot{\nu}_i C_{\epsilon_i} C_{\nu_i} - \rho_i \dot{\epsilon}_i^2 C_{\epsilon_i} S_{\nu_i} - \rho_i \ddot{\epsilon}_i S_{\epsilon_i} S_{\nu_i} \\ &- 2\rho_i \dot{\epsilon}_i \dot{\nu}_i S_{\epsilon_i} C_{\nu_i} - \rho_i \dot{\nu}_i^2 C_{\epsilon_i} S_{\nu_i} + \rho_i \ddot{\nu}_i C_{\epsilon_i} C_{\nu_i}, \end{aligned} \tag{4.91}$$

$$\ddot{\tilde{x}}_i = \ddot{\rho}_i S_{\epsilon_i} + 2\dot{\rho}_i \dot{\epsilon}_i C_{\epsilon_i} - \rho_i \dot{\epsilon}_i^2 S_{\epsilon_i} + \rho_i \ddot{\epsilon}_i C_{\epsilon_i}, \tag{4.92}$$

where $C_{\epsilon_i} = cos(\epsilon_i)$, $S_{\epsilon_i} = sin(\epsilon_i)$, $C_{\nu_i} = cos(\nu_i)$, and $S_{\nu_i} = sin(\nu_i)$. Substitution of Equations (4.87)-(4.89) into Equations (4.90)-(4.92) leads to a relation between the desired nominal values, ρ_i°, ν_i°, and ϵ_i°, and the actual state response. The resulting expression may subsequently be transformed into the ephemeris inertial frame, using ${}^{I}C^{U}$, and substituted into Equation (4.79) to determine the control input that achieves the desired dynamical response. Again, both methods described here accomplish essentially the same goal but the dynamical constraints are specified based on a different set of variables.

Example 1: Thruster On/Off Sequence

One of the constraints imposed on MAXIM, as presently envisioned, specifies that the thrusters should not be in operation during the science collection phase. For phase two, this may last for up to 100,000 seconds (27.8 hours) at a time, over a total observation period of three weeks. More specifically, the thrusters are deactivated for 27.8 hours, then reactivated to return the vehicles to the nominal path. Once all the vehicles have returned to their appropriate positions, the thrusters are once again turned off for 27.8 hours. For a particular target, this cycle may be repeated as necessary over a period of three weeks.

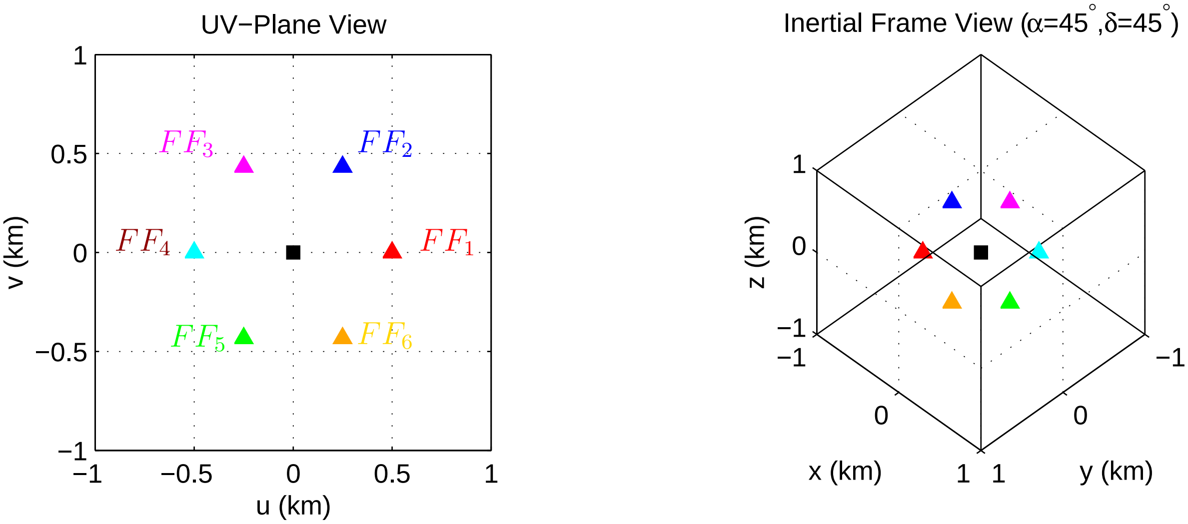

Figure 4.22. MAXIM Configuration: Free Flyer Distribution Relative to Hub

Suppose that the first IFL method described above is employed for formation keeping. Due to the highly sensitive nature of the dynamics near the libration points it is necessary to determine how far the vehicles will drift from the nominal path while the thrusters are inactive. To illustrate this, assume that, during phase two, the MAXIM formation is investigating a target located at $\alpha = 45°$ and $\delta = 45°$ relative to the ephemeris inertial frame. The nominal distribution of the free flyers is further assumed to be specified by $\nu_1 = 0°$, $\nu_2 = 60°$, $\nu_3 = 120°$, $\nu_4 = 180°$, $\nu_5 = 240°$, $\nu_6 = 300°$, $\rho_i = 500$ m and $\epsilon_i = 0°$ for $i = 1, \ldots, 6$ This particular arrangement is illustrated in Figure 4.22. If the thrusters are initially active, and are later turned off for 100,000 seconds, Figures 4.23-4.24 illustrate the drift of the detector and each free flyer from their specified nominal positions. In Figure 4.23, the radial drift is computed as $||\bar{r}^{HD_i} - \bar{r}_i^\circ||$. The angular drifts in Figure 4.24 are simply the difference between the actual and desired angular positions of each deputy, $\nu_i - \nu_i^\circ$ and $\epsilon_i - \epsilon_i^\circ$. The thrust magnitude applied by each spacecraft before and after the thruster off sequence is illustrated in Figure 4.25.

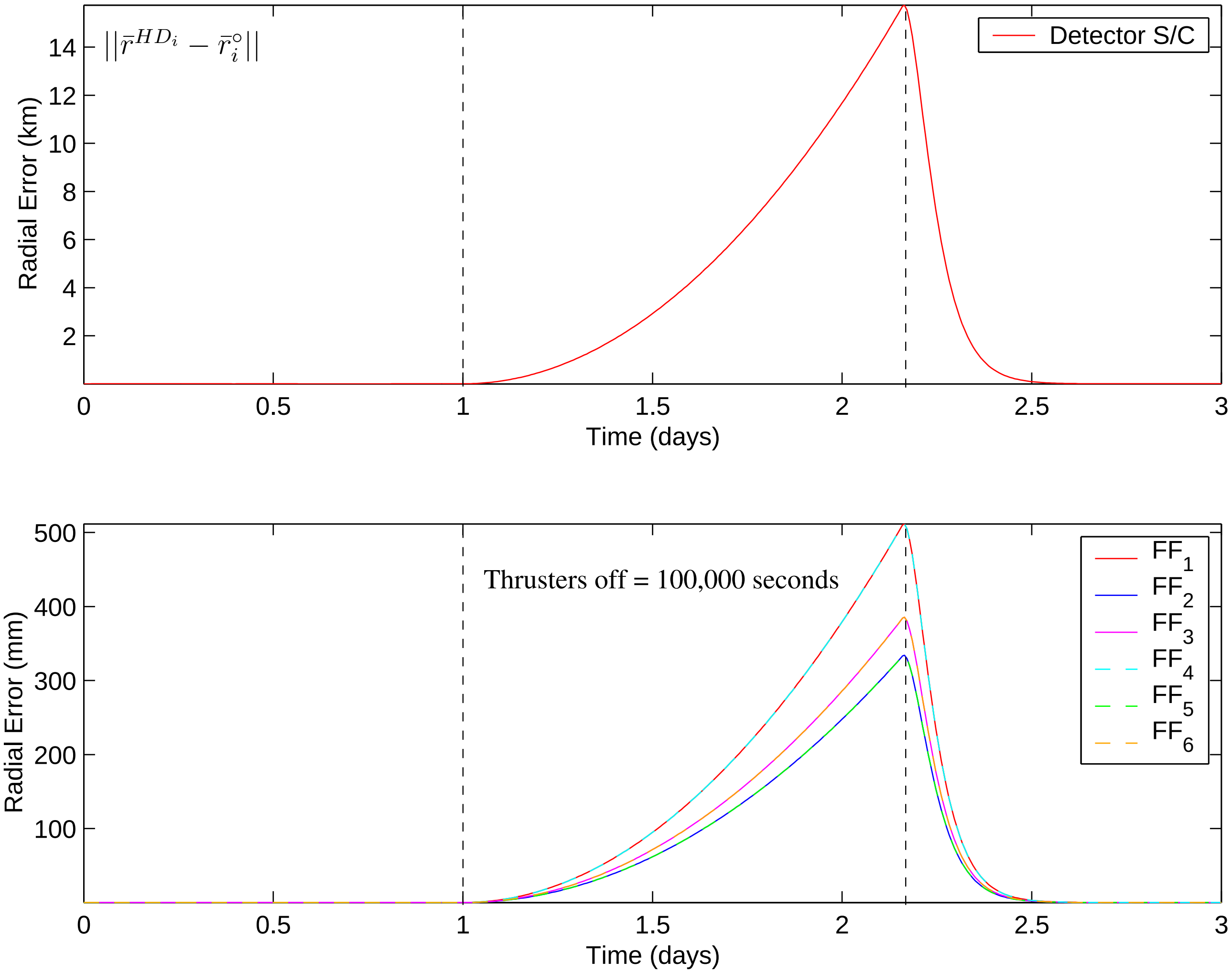

Figure 4.23. Radial Drift During Thrusters Off Sequence

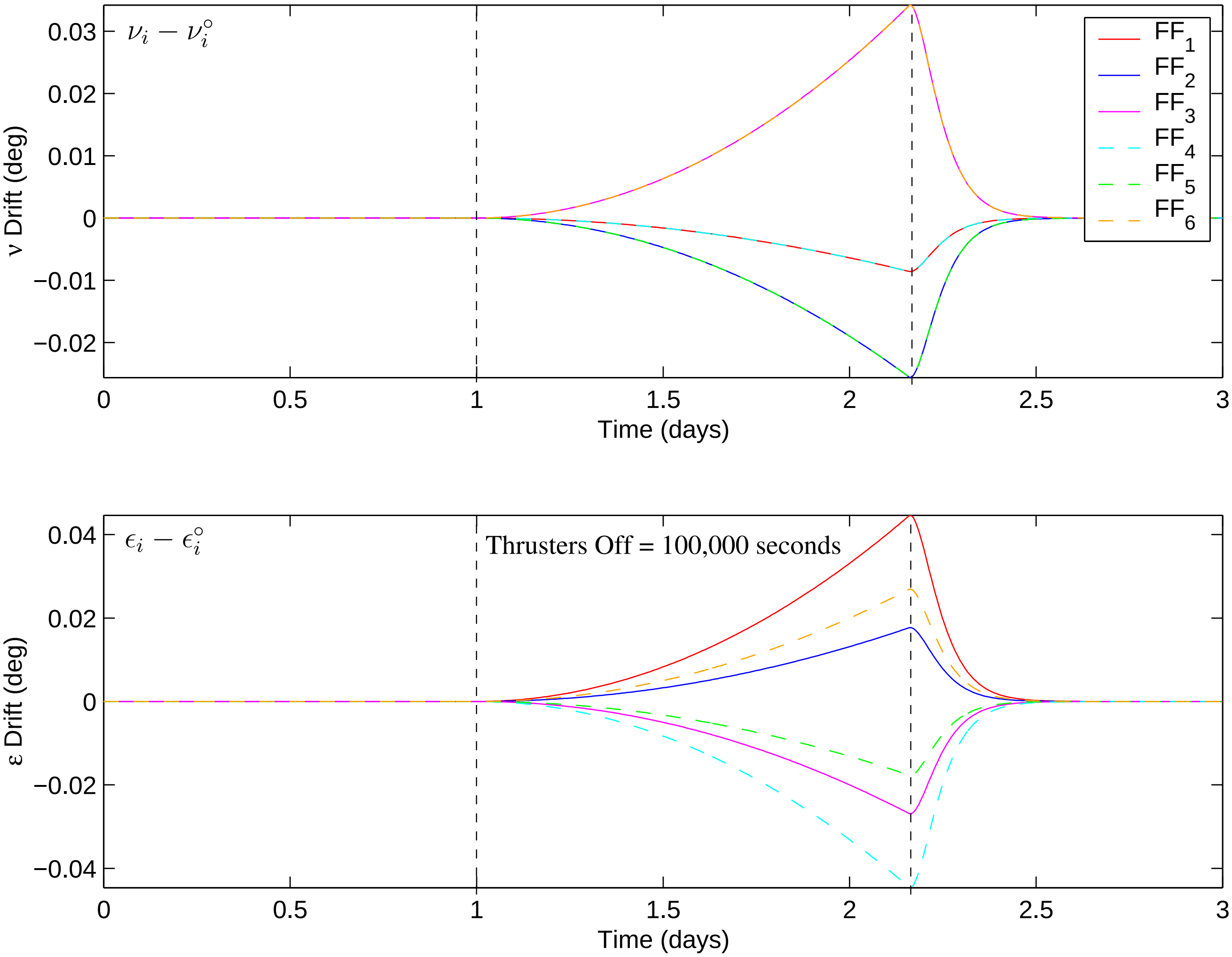

Figure 4.24. Angular Drift During Thrusters Off Sequence

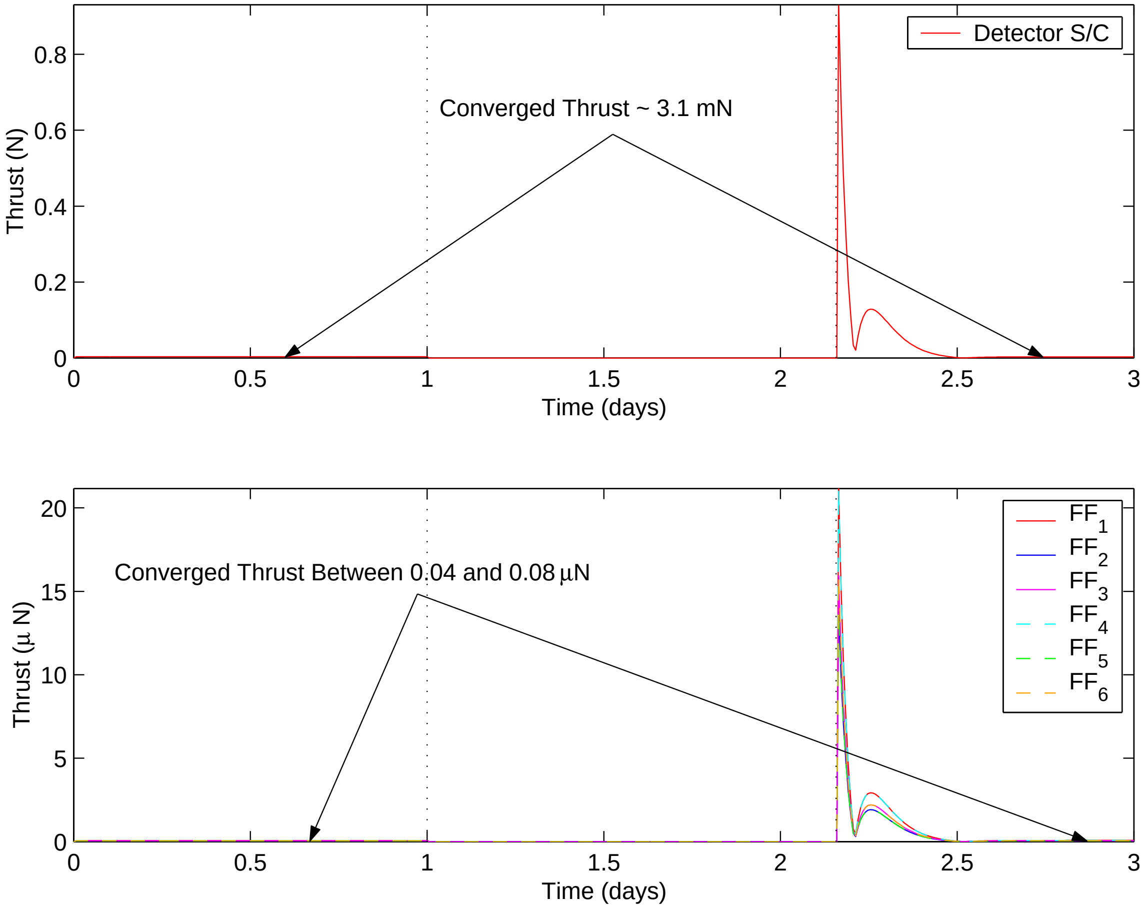

Figure 4.25. Thrust Profile for Sample Thruster On/Off Sequence

It is apparent, from Figure 4.23, that deactivation of the thrusters during a period of 100,000 seconds allows the vehicles to quickly drift beyond the acceptable tolerance range. This is particularly true for the detector spacecraft. In this particular example, the detector drifts by almost 15 km during the coast segment. Although the free flyer drift is below 600 mm, this is still well above the presently specified tolerances of μm.

Example 2: Formation Reconfigurations

In addition to thruster on/off sequences, frequent reconfigurations are expected over the lifetime of the mission. To illustrate the thrust requirements associated with reconfigurations suppose that, during phase two, the MAXIM formation is observing a target characterized by $\alpha = 0°$ and $\delta = 0°$. This is equivalent to a target that is aligned with the inertial X-axis in the ephemeris coordinate system. For simplicity, assume that the thrusters can be operated continuously. Let the new target be aligned with the inertial Y-axis, hence $\alpha = 90°$ and $\delta = 0°$. For phase two, the current requirements stipulate a reconfiguration time of one week [51]. That is, in one week all the vehicles in the formation must be at their respective nominal positions relative to the chief spacecraft. The initial and final target orientations are illustrated in Figures 4.26-4.27. Figure 4.26 illustrates the reconfiguration of the detector relative to the hub. Figure 4.27, then, illustrates the initial and target orientation of the free flyers in both the U-frame and the I-frame. Note that the position of the deputies in the U-frame is not affected, only the orientation of the formation in the ephemeris inertial frame, I, has changed. The thrust profile associated with this particular configuration is plotted in Figure 4.28. If the response time is reduced the thrust requirements for all the vehicles increase. However, the increase is most significant for the detector since it is located 20,000 km aft of the hub.

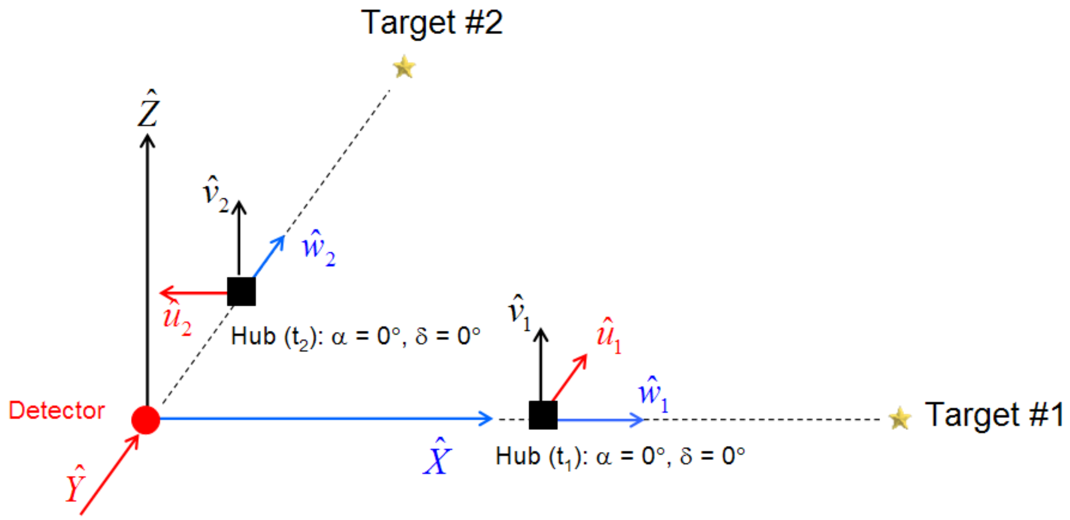

Figure 4.26. Sample Reconfiguration of MAXIM Formation

In the previous example, where a thruster on/off sequence is considered, the response time is only a few hours. In this case, the non-dimensional response frequency, originally set to $\omega_n = 1250$, is adjusted to yield a slower response time, $\omega_n = 38.2012$, because reconfiguring the detector, 20,000 km away, within a few hours results in significantly larger thrust inputs.

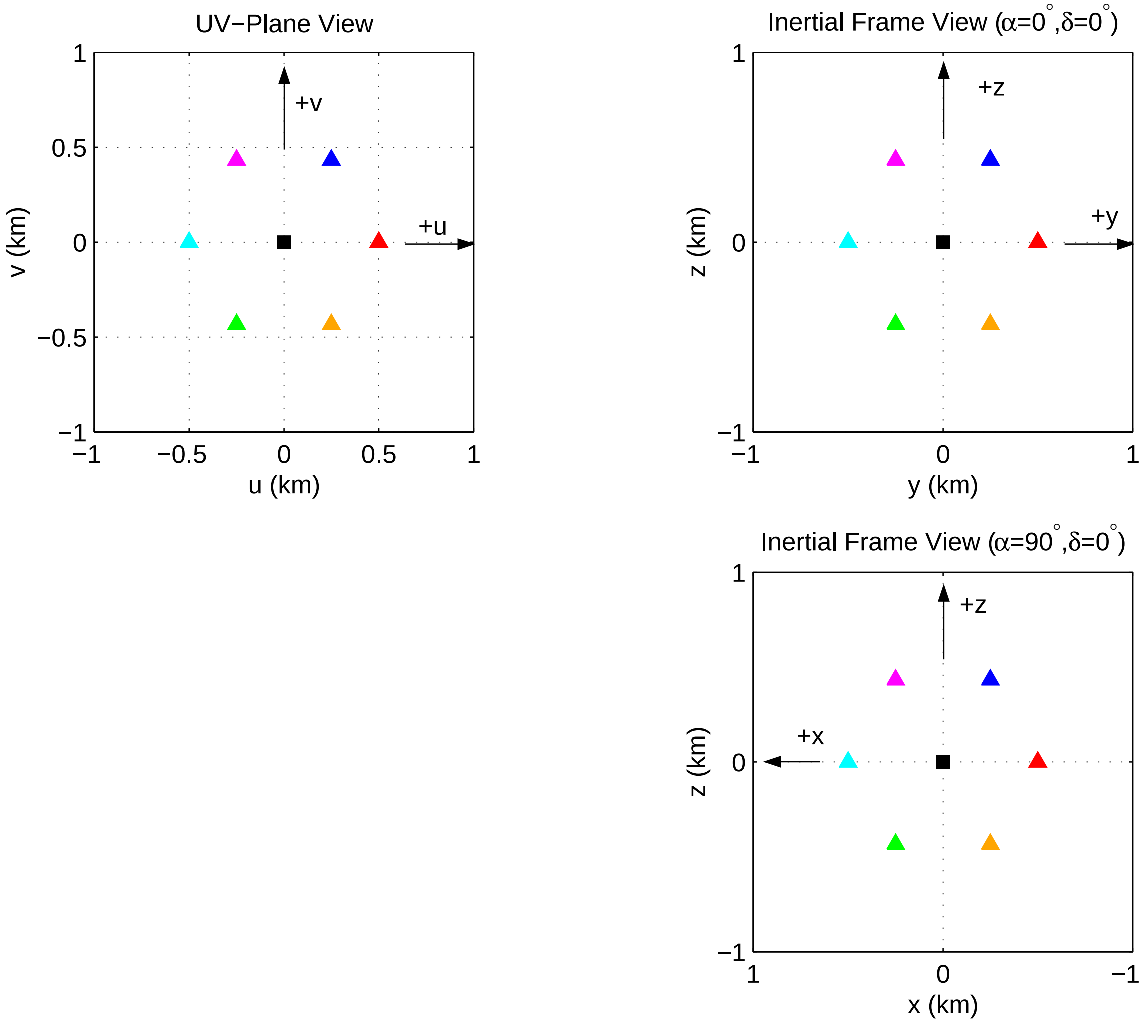

Figure 4.27. Initial and Target Orientations of Sample Formation

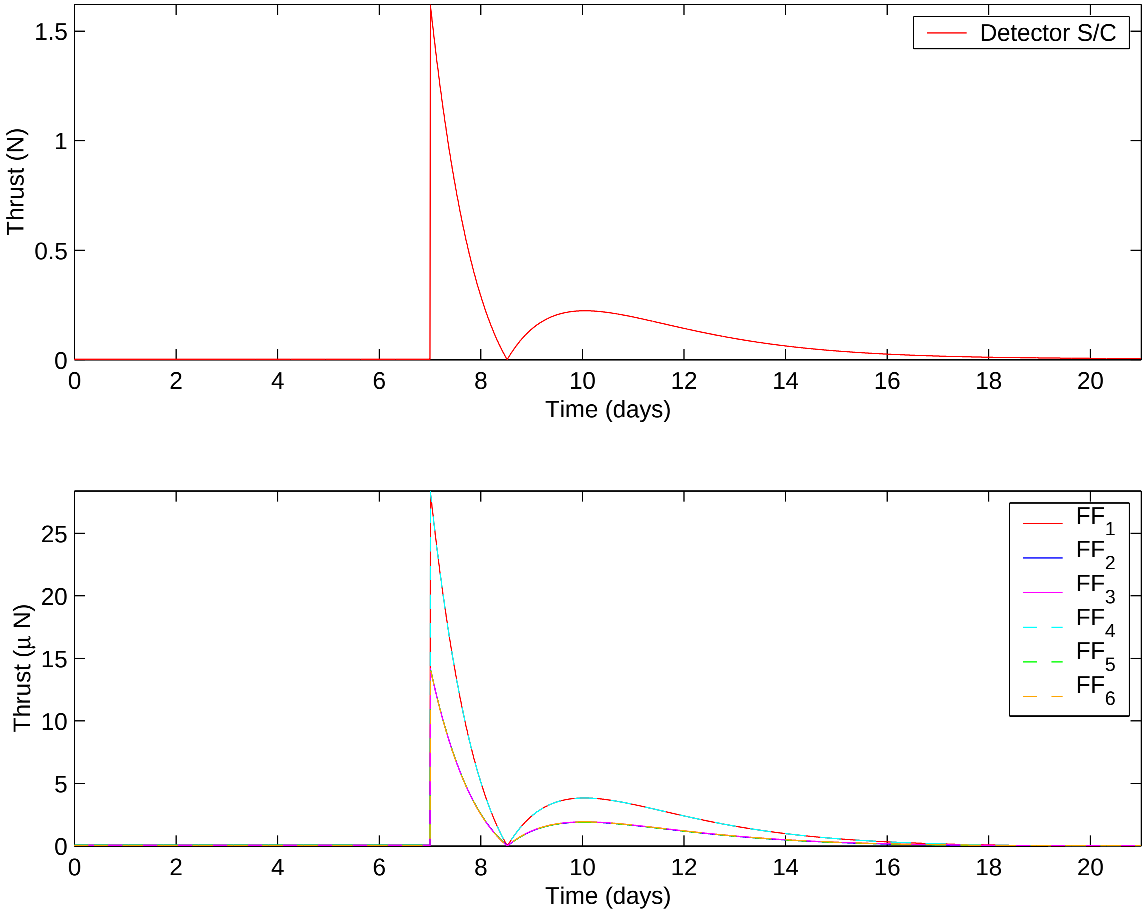

Figure 4.28. Thrust Profile for Sample Reconfiguration During Phase 2

5. Non-Natural Formations: Impulsive Control

In this study, four different discrete control strategies are also considered for formation keeping. All of these rely on knowledge of the linearized dynamics associated with the reference orbit, but incorporate the nonlinear response of the vehicle. In this case, the reference orbit is the path of the chief spacecraft, assumed to evolve along a 2×10^5 km “halo” like Lissajous trajectory, as determined in the EPHEM model. The deputy dynamics, then, are modeled as a perturbation relative to the reference orbit. The success of a particular control strategy depends, in part, on the nominal motion that is required of the deputy.

The first method employs a sample set of natural formations, discussed in Chapter 2, as starting solutions for a two-level corrector with end state constraints. Naturally, the effectiveness of a differential corrections process depends on (a) the quality of the initial guess and (b) the geometry of the local phase space. If the constraints are not consistent with the dynamical flow in the vicinity of the reference solution, the corrector may experience difficulties converging onto a solution. In this particular set of examples, the specified constraints are equivalent to imposing periodicity in the EPHEM model.

A second scheme involves a simple targeter approach that is applied to non-natural formations in the EPHEM model. In this case, the specified target corresponds to either a fixed relative state or a fixed radial distance between the vehicles in the formation. In a simple targeter scheme, the goal is to ensure that the specified constraints, at the end of each segment, are met as closely as the dynamics will allow. However, this type of formulation does not offer any control over the deviations incurred between maneuvers. For a fixed end state targeter, the deviation from the nominal state along the length of each segment can be significant.

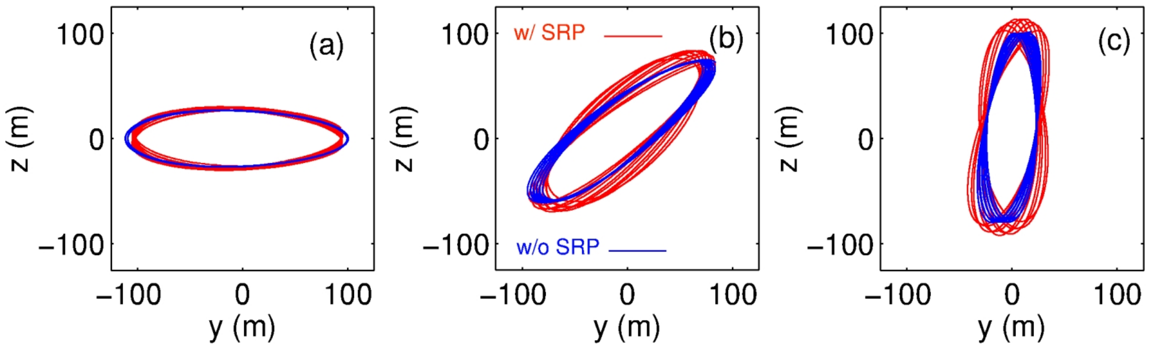

Figure 5.1. Natural Formations in the Ephemeris Model – Impact of SRP

To address this issue, an impulsive nonlinear optimal control methodology is devised that minimizes the error along the length of each segment rather than just at the end of the segment. A more "global" approach is also presented, using the same mathematical model, to minimize the error over the duration of the mission rather than at the end of each segment.

5.1 Two-Level Corrector with End State Constraints

Recall, from Chapter 3, that a variety of nearly periodic and slowly expanding natural formations exist in the rotating frame of the primaries, as defined in the CR3BP. A representative sample of these types of solutions is illustrated in Figure 3.7. The trajectories in Figure 3.7 are easily transitioned into the EPHEM model via a two-level differential corrections process [40]. Some examples of such relative motions, as determined in the EPHEM model, appear in Figure 5.1. As deduced from this figure, the relative path is clearly not periodic, but as an initial guess, it is sufficiently close to periodic if the effects of SRP are small. In this case, a differential corrector with end point constraints, developed by Wilson and Howell [52], is applied to enforce periodicity through a series impulsive maneuvers.

Consider the first two revolutions (without SRP) in Figure 5.1(b) and identify this trajectory segment as $\Gamma(T_1)$, where T_1 represents the approximate period. Let $\bar{x}_i(t_0) = \bar{x}(t_0)$ and $\bar{x}_e(t_m) = \bar{x}(t_m)$ denote the initial and final states along $\Gamma(T_1)$, respectively, and let $\bar{x}_k = \bar{x}(t_k)$, for $k = 1, \ldots, m-1$, denote a discrete set of interior states such that $t_0 < t_k < t_m$. Since $\Gamma(T_1)$ is nearly periodic, replace the final state, at time t_m, with the initial state such that $\bar{x}_e(t_m) = \bar{x}_i(t_0)$. This set of $m+1$ patch states serves as an initial guess to the differential corrector developed by Wilson and Howell [52]. In the first level of this process, each trajectory segment is integrated from $t_k \rightarrow t_k + 1$, for $k = 0, \ldots, m-1$. A simple differential corrections process seeks to achieve position continuity while allowing a maneuver at each patch state, $\Delta V(t_k)$. The next level of the corrector allows the position of each patch state, $\bar{r}(t_k)$, to “float” seeking to reduce the interior maneuvers and meet the end point constraint.

Once the differential corrections process converges on a solution, the resulting patch states are shifted forward in time such that $t_k = t_k + T_1$, for $k = 0, \ldots, m$. This new set of patch states is then differentially corrected, as before, to enforce periodicity over the new time interval in the EPHEM model. The resulting trajectory is represented by $\Gamma(T_2)$. Since the initial and final states are always fixed, the individual trajectory arcs, $\Gamma(T_q)$, can later be patched together for position continuity over N revolutions. The velocity discontinuities at the interior nodes, $\bar{v}_e(T_q)$, the intersection of $\Gamma(T_q)$ and $\Gamma(T_{q+1})$, represent impulsive maneuvers. Once the desired number of revolutions is achieved, the patch states along each arc can be merged into one set of patch points and differentially corrected simultaneously. This time, a maneuver is allowed at the connecting nodes between each $\Gamma(T_q)$. A sample solution, over six revolutions, is plotted in Figure 5.2 and is generated by applying two impulsive maneuvers ranging in size from 2.5 m/sec to 5 m/sec at the end of the second and fourth revolutions. Note that periodicity, in this case, is enforced in the P1P2ROT frame and one period encompasses two revolutions along the orbit.

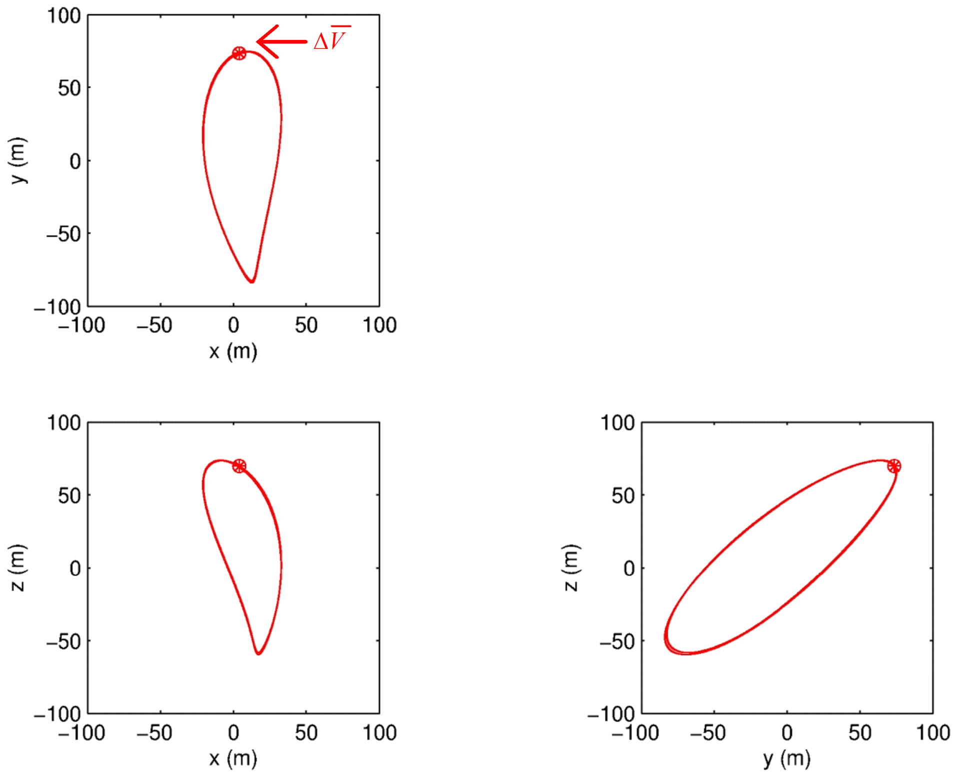

Figure 5.2. Controlled Periodic Orbit in the P1P2ROT Frame (EPHEM w/o SRP)

A similar approach can be applied to the nearly vertical trajectory in Figure 5.1(c) to obtain vertical periodic relative orbits; the result is plotted in Figure 5.3. This particular approach works very well if periodicity is enforced in the rotating frame as demonstrated in Figures 5.2 and 5.3, as opposed to the inertial frame. Relative to an observer fixed in the rotating frame, these solutions appear to be sufficiently close to periodic and are, subsequently, a suitable initial guess for the differential corrector. However, the associated inertial perspectives that appear in Figure 5.4, are quite different. These trajectory arcs do not represent a sufficiently accurate initial guess if periodicity is required in the inertial frame. The natural geometry of the solution is such that the inertial and rotating views of the same trajectory are quite different. Of course, the Earth is at a different location in its orbit every time a revolution is completed, as opposed to a perspective originating in the rotating frame.

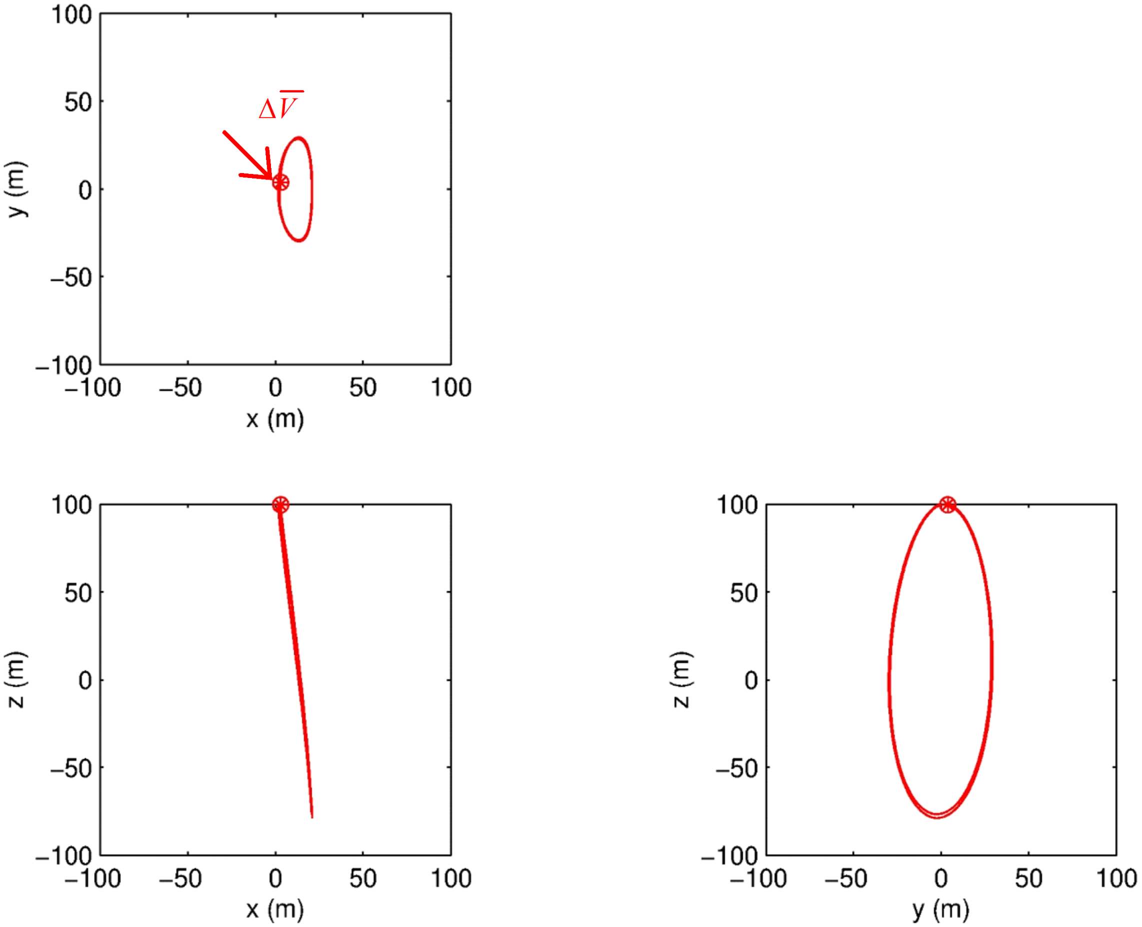

Figure 5.3. Controlled Vertical Orbit in the P1P2ROT Frame (EPHEM w/o SRP)

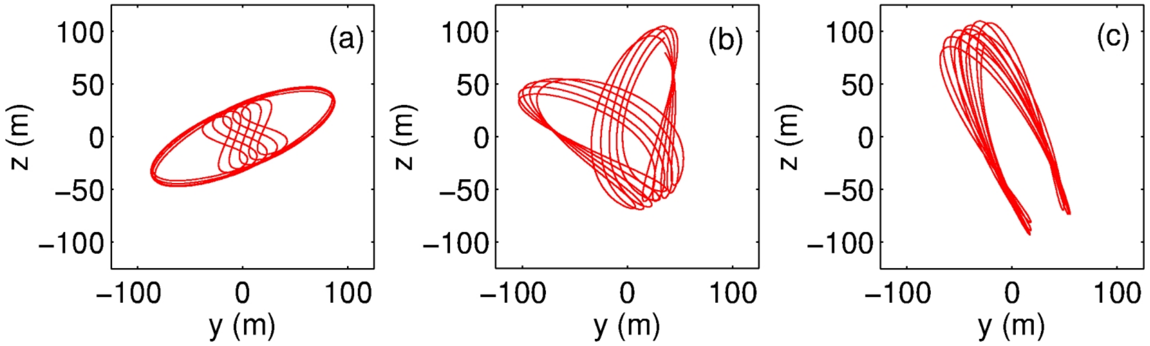

Figure 5.4. Natural Formations in the Ephemeris Model (w/ SRP)
Inertial Frame Perspective of Figures 5.2-5.3

5.2 Targeting a Nominal Relative State

Consider a formation of two spacecraft separated by 100 km, constrained to remain aligned with the inertial y-axis $(\hat{Y})$ at all times. In the absence of any external perturbations, a continuous control approach via IFL requires 0.3348 m/sec of total ΔV over a period of 180 days. How much will the formation diverge if the control input is discretized over a period of hours, or even days? Consider the general form of the solution to the linear system,

$$\begin{bmatrix} \delta\bar{r}_{k+1} \\ \delta\bar{v}_{k+1}^{-} \end{bmatrix} = \Phi\left(t_{k+1}, t_k\right) \begin{bmatrix} \delta\bar{r}_{k} \\ \delta\bar{v}_{k}^{+} \end{bmatrix} = \begin{bmatrix} A_k & B_k \\ C_k & D_k \end{bmatrix} \begin{bmatrix} \delta\bar{r}_{k} \\ \delta\bar{v}_{k}^{-} + \Delta\bar{V}_k \end{bmatrix}, \tag{5.1}$$

where $\Phi\left(t_{k+1}, t_k\right)$ denotes the state transition matrix, for the k^{th} segment, associated with the nominal Lissajous orbit along which the chief spacecraft is assumed to evolve. The symbol δ denotes a perturbation relative to the nominal Lissajous trajectory, the superscript "+" or "−" signifies the beginning or end of a segment at time t_k, respectively, and $\Delta\bar{V}_k$ represents an impulsive maneuver applied at t_k. Controlling the position of the deputy spacecraft relative to the chief to a constant vector, as observed in the inertial frame, is equivalent to targeting a particular constant perturbation $\delta\bar{r}_{k+1}$ relative to the inertial frame.

An impulsive maneuver of the form

$$\Delta\bar{V}_k = B_k^{-1}\left(\delta\bar{r}_{k+1} - A_k\delta\bar{r}_k\right) - \delta\bar{v}_k^-, \tag{5.2}$$

will accomplish the goal in the linear system. In the nonlinear system, however, the above solution must be differentially corrected to identify the precise maneuver that meets the end state constraint to within the specified tolerance levels, as discussed by Howell and Barden [26–28].

To illustrate the range of effectiveness of the targeter scheme, consider a formation characterized by a 10 meter separation between the chief and deputy spacecraft. In particular, let the nominal formation be defined by $\bar{\rho} = (10\text{ m})\,\hat{Y}$ and $\dot{\bar{\rho}} = \bar{0}$. As is apparent in Figure 5.5, the maximum deviation achieved between maneuvers is significantly smaller, dropping below one centimeter, for maneuvers scheduled at least every 2 days. The maneuver history for each of the examples in Figure 5.5 is plotted in Figure 5.6. Note that the magnitude of the individual maneuvers is extremely small, consistent with the natural sensitivity to small changes in this region of space. Hence, the error introduced in any attempt to physically implement such a small maneuver may offset the benefits.

The results in Figure 5.5 also raise another issue. The maximum error incurred between maneuvers, for a fixed maneuver schedule, depends on the nominal relative distance. Hence, formations characterized by larger nominal separations require maneuvers that are more closely scheduled. It is then necessary to determine an appropriate maneuver frequency such as to maintain the error below an acceptable threshold. The necessary maneuver frequency may be identified from Figure 5.7. As observed from this figure, formation separations of up to 50 meters can be achieved to within a centimeter at all times, if a maneuver is performed once a day. If that interval is doubled to once every two days, then the maximum relative separation that is possible drops to 15 meters.

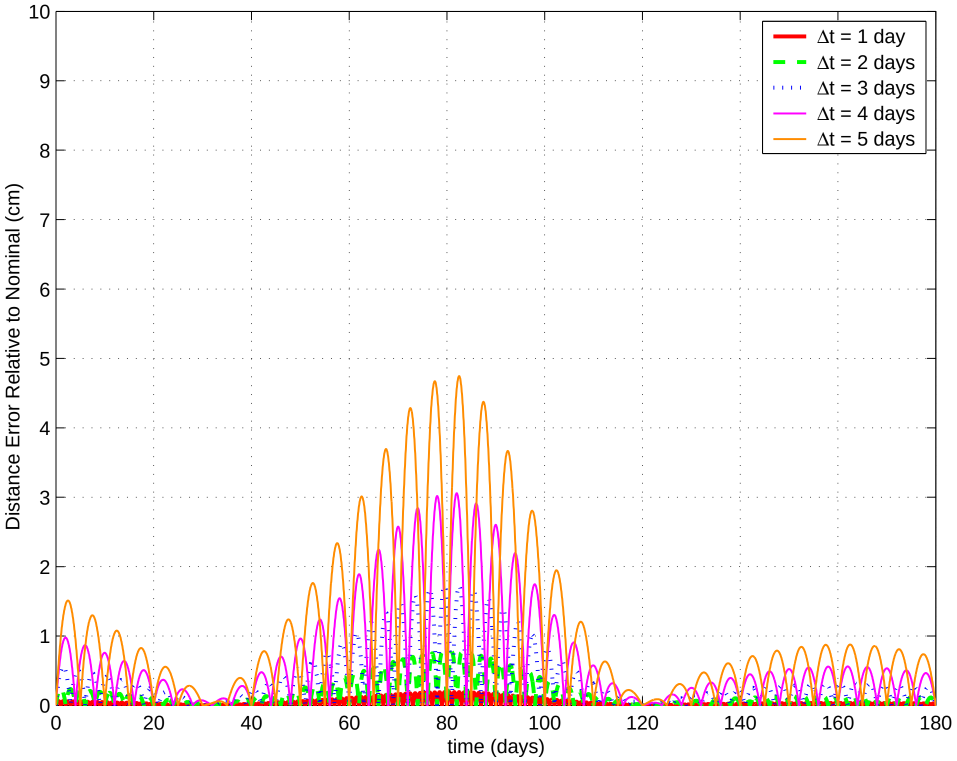

Figure 5.5. Magnitude of Relative Position Error via Simple Targeter Approach

The results in Figure 5.7 further suggest that, if sub-millimeter accuracy is necessary for a particular formation, nominal separations on the order of kilometers do require nearly continuous control in order to maintain the relative state error within acceptable levels. Also note that, as the maneuvers become more closely spaced they also decrease in size. The magnitude of the maneuvers along the curves in Figure 5.6 is already extremely small (10^{-6} m/sec). So, for continuous or discrete control, highly precise formation keeping, for small relative separations, may represent a challenge, in terms of hardware and implementation, at least, for this particular type of nominal configuration.

Allowing the solution to drift until the maneuver is sufficiently large to implement seems intuitive, however, this is not a feasible alternative in this regime. The highly sensitive natural flow in this region of space is constantly acting against these non-natural configurations.

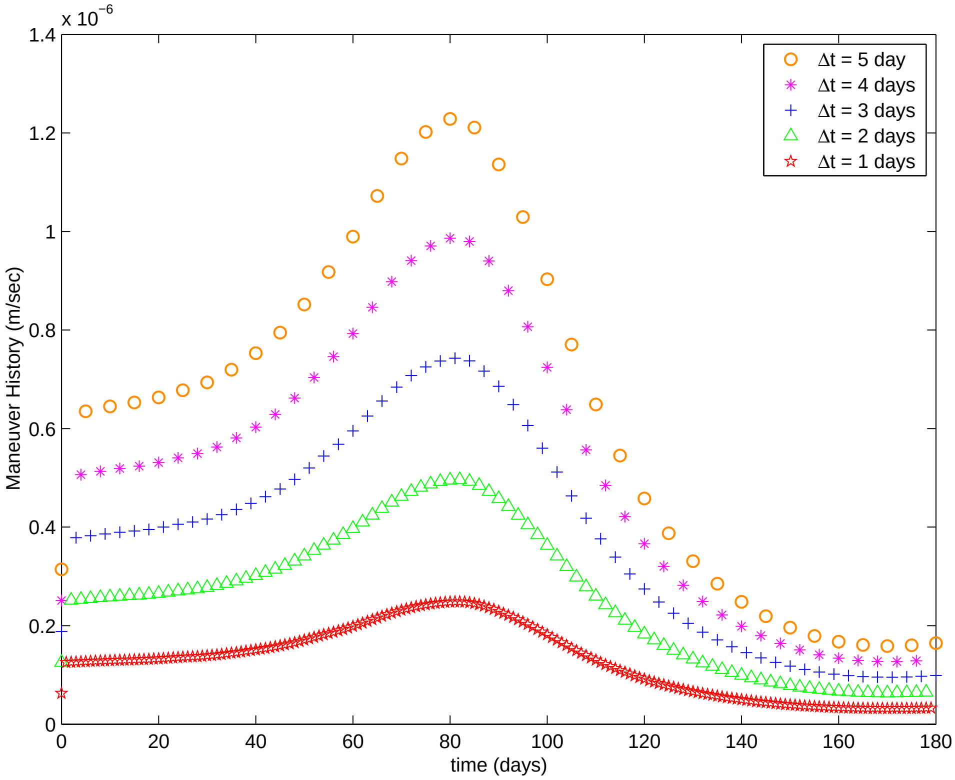

Figure 5.6. Targeter Maneuver Scheme

Hence, regardless of how small the maneuvers may "appear", if they are not implemented accurately, the relative error quickly grows above the sub-millimeter range. This violates the tight formation keeping constraints presently envisioned for some of the proposed space-based interferometers.

5.3 Targeting Radial Distance and Rate

Rather than the complete six-dimensional state vector, the number of targets is reduced, and greater flexibility is introduced, if functions of the states are constrained. Useful quantities here are the radial distance and/or radial rate between the deputy and chief vehicles. Recall that $\bar{x}_d(t)$ denotes the six-dimensional state of the deputy spacecraft relative to the chief.

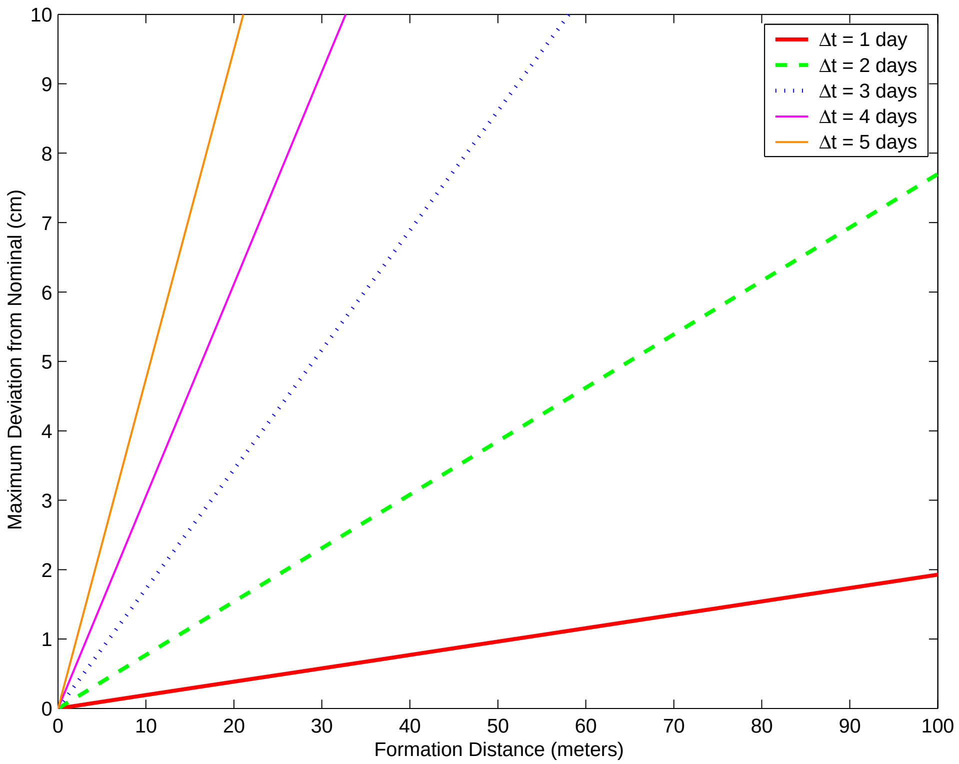

Figure 5.7. Maximum Relative Distance Error vs. Nominal Separation

This state may either be in inertial or rotating coordinates. Let the position elements of $\bar{x}_d(t)$ be denoted by $\bar{r}$ while the relative velocity is denoted as $\dot{\bar{r}}$. The radial distance and radial rates, then, are simply

$$r = \sqrt{\bar{r}^T\bar{r}}\ , \tag{5.3}$$

$$\dot{r} = \frac{\bar{r}^T\dot{\bar{r}}}{r}. \tag{5.4}$$

Let $\bar{g}^\circ = [r^\circ, \dot{r}^\circ]$ represent the desired range and range rate between the chief and deputy vehicles. Relative to this reference solution, a first order approximation of these quantities may be determined as

$$\bar{g} = \bar{g}^o + \frac{\partial \bar{g}}{\partial \bar{x}_d}(0)\delta\bar{x}_d(0). \tag{5.5}$$

Equation (5.5) can be expressed as a function of the state transition matrix associated with the chief spacecraft,

$$\bar{g} - \bar{g}^\circ = \frac{\partial \bar{g}}{\partial \bar{x}_d}(t)\frac{\partial \bar{x}_d(t)}{\partial \bar{x}_d(0)} = \frac{\partial \bar{g}}{\partial \bar{x}_d}(t)\Phi(t,t_0), \tag{5.6}$$

where

$$\frac{\partial \bar{g}}{\partial \bar{x}_d} = \begin{bmatrix} \frac{\partial r}{\partial \bar{r}} & \frac{\partial r}{\partial \dot{\bar{r}}} \\ \frac{\partial \dot{r}}{\partial \bar{r}} & \frac{\partial \dot{r}}{\partial \dot{\bar{r}}} \end{bmatrix}. \tag{5.7}$$

The partials in Equation (5.7) are easily determined as

$$\frac{\partial r}{\partial \bar{r}} = \left(\frac{\bar{r}}{r}\right)^T = \hat{r}^T, \tag{5.8}$$

$$\frac{\partial r}{\partial \dot{\bar{r}}} = \bar{0}^T, \tag{5.9}$$

$$\frac{\partial \dot{r}}{\partial \bar{r}} = \left(\frac{\dot{\bar{r}} - \dot{r}\hat{r}}{r}\right)^T, \tag{5.10}$$

$$\frac{\partial \dot{r}}{\partial \dot{\bar{r}}} = \hat{r}^T. \tag{5.11}$$

Let M define the state relationship matrix such that,

$$M = \frac{\partial \bar{g}}{\partial \bar{x}_d}(t)\,\Phi\,(t,t_0) = \begin{bmatrix} M_1 & M_2 \end{bmatrix}, \tag{5.12}$$

where M_1 and M_2 are 2×3 matrices. Since the initial position, $\bar{r}\,(0) = \bar{r}_0$, is fixed, the associated variation, $\delta\bar{r}_0$, is zero. The velocity variation, then, can be determined from the minimum norm solution,

$$\delta\dot{\bar{r}}_0 = M_2^T \left(M_2 M_2^T\right)^{-1} \left(\bar{g}\,(t) - \bar{g}^\circ\,(t)\right). \tag{5.13}$$

Note that if the objective is control of only radial distance, then M_1 and M_2 are 1×3 matrices. Clearly, there are an infinite number of solutions that satisfy Equation (5.6). At any given time, solutions consistent with the constraints for radial distance and rate may or may not be contained within this solution space. The minimum norm approach seeks to identify the smallest maneuver that can achieve the desired goal at the end of each trajectory segment.

To demonstrate the effectiveness of this targeter, consider the following example. Let the initial state of the deputy, relative to the chief spacecraft, be defined by $\bar{r}_0 = (5000 \text{ km})\ \hat{z}$ and $\dot{\bar{r}}_0 = \bar{0}$. Define the nominal range as 5000 km from the chief vehicle. Figure 5.8 includes three curves, each a time history for range, over 180 days, corresponding to one of three different correctors. The red curve is associated with the state corrector discussed in the previous section. That is, the target state, at the end of each trajectory segment, is defined $\bar{r}^\circ = \bar{r}_0$ and $\dot{\bar{r}}^\circ = \bar{0}$. The blue trajectory, then, corresponds to the range error if only the radial distance and radial rate are constrained, for maneuvers determined from Equation (5.13). If, instead, the range rate is free, and only the radial distance is constrained, the magenta curve in Figure 5.8 demonstrates how the range error evolves over the duration of the mission. Note that the differential corrector, in this third case, is essentially the same as that described by Equation (5.13) except that the last row of M_2 is removed. Hence, the minimum norm solution is sought from one equation with three unknowns. The impulsive maneuver scheme associated with the results in Figure 5.8 appear in Figure 5.9. The size of the maneuvers and the total costs appear similar, but the excursions from the nominal are notably different, as observed from Figure 5.8. Since the overall error is significantly larger for the corrector that targets only range, the associated maneuver scheme is not included in Figure 5.9 and subsequent analysis.

In any impulsive scheme, the path of the deputy will diverge from the desired nominal between maneuvers. An important observation, deduced from Figure 5.8, is that the degree of divergence depends on the nominal constraints imposed at the end of each trajectory segment. If minimizing the radial distance error over the length of each segment is desired, the range and range rate corrector offers a clear advantage over the other two correction schemes. Naturally, if maintaining the deputy at a constant distance and orientation, relative to the chief vehicle, is required to achieve the science goals of a particular mission, this type of corrections scheme is not adequate. This is best visualized in Figure 5.10. The transparent blue sphere in this Figure represents the nominal radial distance constraint.

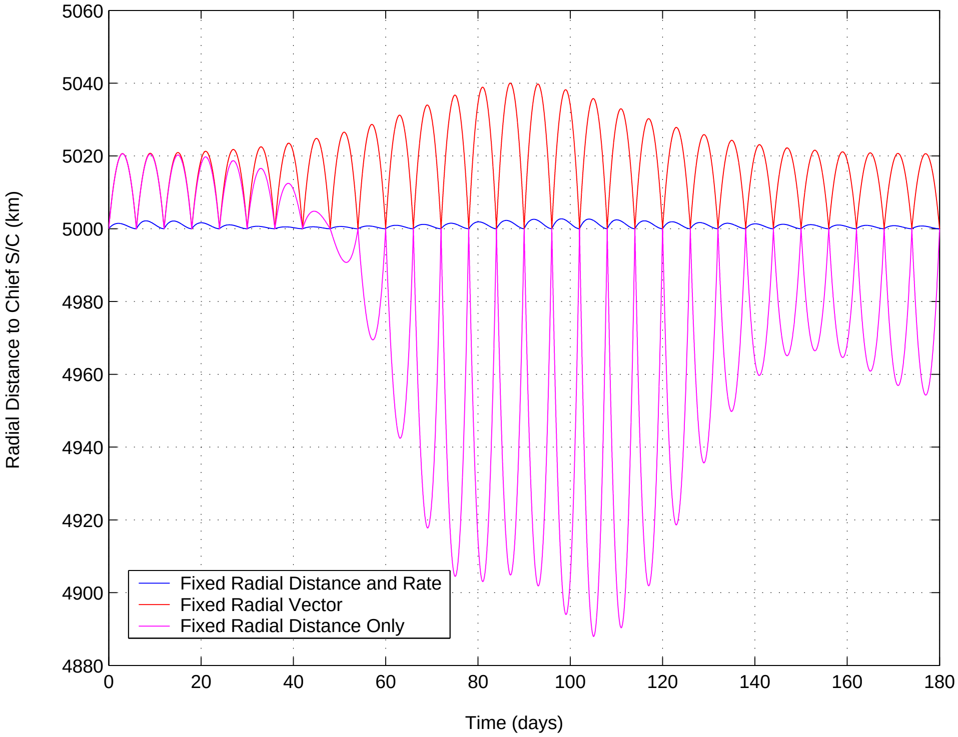

Figure 5.8. Magnitude of Relative Position Error - Radial vs. State Targeter

The chief spacecraft is at the origin of this sphere. Now, nominally, at the end of each trajectory segment, the deputy is constrained to lie on this sphere and to approach this end point tangentially, $\dot{r} = 0$. Clearly, the natural dynamics allow for a radial distance that is very close to the nominal over the entire duration of the mission. However, in doing so, the deputy path is free to move anywhere along the nominal sphere.

The results and observations noted here are applicable regardless of the frame – inertial or rotating – in which the differential corrector is implemented, in either the CR3BP or EPHEM models. Of course, care must be exercised during the numerical implementation of any differential corrections process. In this case, inverting $(M_2 M_2^T)$ may lead to convergence difficulties in the corrections process, particularly over some trajectory segments, if the smaller singular value of M_2 approaches zero. So, it is best to delay the next maneuver until a more opportune time.

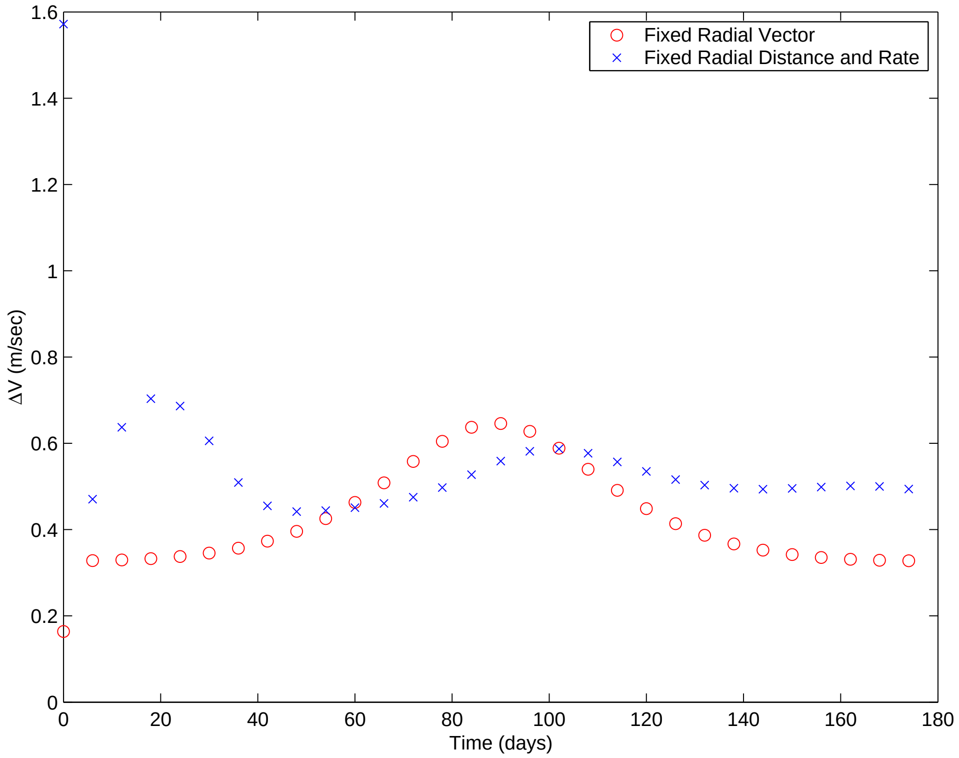

Figure 5.9. Maneuver History - Radial vs. State Targeter

Note that, as presently envisioned, formations like MAXIM or TPF cannot benefit from this particular control approach because the nominal state for each deputy is completely specified. However, the results of this investigation are not exclusive to fixed state configurations or precision formation keeping. Hence, other types of missions may benefit from this particular methodology.

5.4 Discrete Optimal Control

If continuous operation of the thrusters is not a feasible option for a particular mission, there are two additional alternatives. One of these options is the more traditional impulsive control approach.

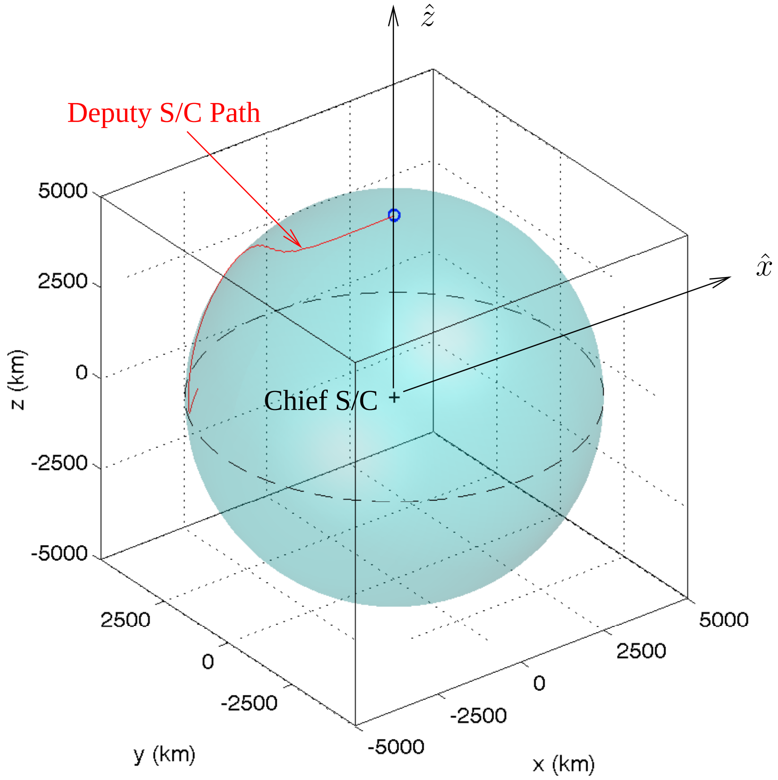

Figure 5.10. Deputy S/C Path - Radial vs. State Targeter

It is also possible to allocate some thruster on/off time. The following discussion presents this problem from an optimal control perspective. Consider a discrete nonlinear map,

$$\bar{x}\left(t_{i+1}\right) = F\left[\bar{x}\left(t_i\right), \bar{u}\left(t_i\right), t_i\right] \tag{5.14}$$

subject to

$$\bar{x}\left(t_0\right) = \bar{x}_0. \tag{5.15}$$

Note that this map is directly related to the original nonlinear equations of motion through a simple integration over the segment defined by $t \in [t_i, t_{i+1})$,

$$\bar{x}\left(t_{i+1}\right) = \bar{x}\left(t_i\right) + \int_{t_i}^{t_{i+1}} \bar{f}\left(t, \bar{x}\left(t\right), \bar{u}\left(t\right)\right) dt. \tag{5.16}$$

In the above representation, the entire trajectory, from $t \in [t_0, t_N)$, is divided into $N - 1$ segments and N nodes.

The control options include application of an impulsive input at the start of each segment or application of constant thrust over the length of each segment. Considering these alternatives, let J denote a scalar cost function of the states and inputs at each node along the trajectory. The goal, then, is to identify the sequence of control inputs that will minimize

$$J = \phi\left(\bar{x}\left(t_N\right)\right) + \sum_{i=0}^{N-1} L\left[\bar{x}\left(t_i\right), \bar{u}\left(t_i\right), t_i\right]. \tag{5.17}$$

The cost function consists of two parts; one is a function of the end state while the other is a function of the path itself. In Equation (5.17), $\phi\left(\bar{x}\left(t_N\right)\right)$ represents the term that depends only on the end state. Under the summation, then, is some scalar function of the states and inputs at each node preceding the end point. Let $\bar{\lambda}\left(t_i\right)$ represent a Lagrange multiplier associated with time t_i. Also, for notational simplicity, let $\bar{x}_i = \bar{x}\left(t_i\right)$, $\bar{u}_i = \bar{u}\left(t_i\right)$, $L_i = L\left(t_i, \bar{x}_i, \bar{u}_i\right)$, $\bar{F}_i = \bar{F}\left(t_i, \bar{x}_i, \bar{u}_i\right)$, and $\bar{\lambda}_i = \bar{\lambda}\left(t_i\right)$. Using these definitions, the cost function in Equation (5.17) can be augmented by (a) the nonlinear map in Equation (5.14) and (b) the initial state constraint in Equation (5.15) through a sequence of Lagrange multipliers such that,

$$\begin{aligned} J &= \phi\left(\bar{x}_N\right) + \bar{\lambda}^T\left(0\right)\left[\bar{x}_0 - \bar{x}\left(t_0\right)\right] \\ &+ \left(\sum_{i=0}^{N-1} L\left(t_i, \bar{x}_i, \bar{u}_i\right) + \bar{\lambda}_{i+1}^T\left[\bar{F}\left(t_i, \bar{x}_i, \bar{u}_i\right) - \bar{x}_{i+1}\right]\right). \end{aligned} \tag{5.18}$$

In the above expression, let the Hamiltonian ($H_i = H\left(t_i, \bar{x}_i, \bar{u}_i\right)$) at the i^{th} node be defined as

$$H_i = L_i + \bar{\lambda}_{i+1}^T \bar{F}_i. \tag{5.19}$$

Using this definition, and after properly adjusting the summation indices, the cost function may be rewritten in terms of the Hamiltonian as follows,

$$J = \phi\left(\bar{x}_N\right) - \bar{\lambda}_N^T \bar{x}_N + \bar{\lambda}_0^T \bar{x}_0 + \sum_{i=0}^{N-1}\left(H_i - \bar{\lambda}_i^T \bar{x}_i\right). \tag{5.20}$$

As detailed by Bryson [53], the first variation of J leads to the following optimality conditions,

$$\bar{\lambda}_i^T = \frac{\partial H_i}{\partial \bar{x}_i} = \frac{\partial L_i}{\partial \bar{x}_i} + \bar{\lambda}_{i+1}^T \frac{\partial \bar{F}_i}{\partial \bar{x}_i}, \tag{5.21}$$

$$\bar{\lambda}_N^T = \frac{\partial \phi\left(\bar{x}_N\right)}{\partial \bar{x}_N}, \tag{5.22}$$

$$\frac{\partial H_i}{\partial \bar{u}_i} = \frac{\partial L_i}{\partial \bar{u}_i} + \bar{\lambda}_{i+1}^T \frac{\partial \bar{F}_i}{\partial \bar{u}_i} = \bar{0}, \tag{5.23}$$

where $i = 0, 1, \ldots, N-1$. For numerical implementation, it is most convenient to rewrite the cost function in terms of an augmented state vector $\tilde{x} = [\bar{x}, x_{n+1}]$ where

$$x_{n+1}\left(t_{i+1}\right) = x_{n+1}\left(t_i\right) + L\left[t_i, \bar{x}_i, \bar{u}_i\right] \tag{5.24}$$

and $\bar{x} \in \mathrm{R}^n$ denotes the original state vector. It is clear, then, that

$$x_{n+1}\left(t_N\right) = \sum_{i=0}^{N-1} L\left[t_i, \bar{x}_i, \bar{u}_i\right]. \tag{5.25}$$

Now, the cost function J is reduced to

$$J = \tilde{\phi}\left(\tilde{x}_N\right), \tag{5.26}$$

where

$$\tilde{\phi} = \phi\left(\bar{x}_N\right) + x_{n+1}\left(t_N\right). \tag{5.27}$$

Let $\tilde{\lambda}$ represent the augmented co-state vector and $\tilde{F}\left(t_i, \tilde{x}_i, \bar{u}_i\right)$ denote the augmented nonlinear map,

$$\tilde{x}_{i+1} = \tilde{F}\left(t_i, \tilde{x}_i, \bar{u}_i\right) = \begin{bmatrix} \bar{F}\left(t_i, \bar{x}_i, \bar{u}_i\right) \\ x_{n+1}\left(t_i\right) + L\left[t_i, \bar{x}_i, \bar{u}_i\right] \end{bmatrix}. \tag{5.28}$$

The optimality conditions, for this augmented system, are given by

$$\tilde{\lambda}_N^T = \frac{\partial \tilde{\phi}\left(\tilde{x}_N\right)}{\partial \tilde{x}_N}, \tag{5.29}$$

$$\tilde{\lambda}_i^T = \tilde{\lambda}_{i+1}^T \frac{\partial \tilde{F}_i}{\partial \tilde{x}_i}, \tag{5.30}$$

$$\frac{\partial \tilde{H}_i}{\partial \bar{u}_i} = \tilde{\lambda}_{i+1}^T \frac{\partial \tilde{F}_i}{\partial \bar{u}_i}. \tag{5.31}$$

The numerical process to compute a solution is then summarized from the following steps,

1. Input $\bar{x}_0$ and some initial guess for the control sequence $\bar{u}_i$.
2. Sequence the augmented state equations in Equation (5.28) forward from t_0 to t_N.
3. Evaluate $\tilde{\lambda}_N^T$ from Equation (5.29).
4. Sequence the co-state equations in Equation (5.30) backwards from t_N to t_0 and evaluate Equation (5.31).
5. Use Equation (5.31) to update the control input vector ($k > 0 \rightarrow$ minimize, $k < 0 \rightarrow$ maximize);

$$\bar{u}_i = \bar{u}_i + \Delta\bar{u}_i = \bar{u}_i - k\left(\frac{\partial H}{\partial \bar{u}_i}\right). \tag{5.32}$$

6. If $\sqrt{\frac{1}{N}\sum\limits_{i=0}^{N-1}\left|\Delta\bar{u}_i\right|^2} < \varepsilon$, the process has converged on an optimal solution. Otherwise, repeat steps 2-6 until convergence is achieved.

The detailed procedure shifts a functional optimization problem into a parameter optimization problem. Naturally, for a dynamical system as complex as the n-body gravitational model, this type of algorithm applied on a nearly continuous control problem is not feasible because there are too many variables to optimize. However, in a discrete problem, this becomes a more reasonable alternative. Of course, the feasibility of this algorithm depends on the availability of an explicit map such as that defined in Equation (5.28). Since no analytical solution is available in the nonlinear CR3BP or the EPHEM model, the discretization must be implemented numerically. That is, the nonlinear map in Equation (5.28) must be numerically integrated SIMULTANEOUSLY with the gradients in Equations (5.30)-(5.31).

In the formation keeping problem, the path dependent term in the cost function, apparent in Equation (5.25), is formulated as an integral of some nonlinear function of the error relative to the nominal solution. That is,

$$x_{n+1}\left(t_N\right) = \sum_{i=0}^{N-1} \int_{t_i}^{t_{i+1}} \tilde{L}\left[t, \bar{x}, \bar{u}\right] dt. \tag{5.33}$$

The goal of this particular formulation is to minimize the overall error over the length of the mission, or segment, rather than just the end state error. For this type of system, the partial derivatives are easily determined from knowledge of the linear system dynamics. Let

$$\dot{\tilde{x}} = \tilde{f}\left(t, \tilde{x}, \tilde{u}\right) = \begin{bmatrix} \bar{f}\left(t, \bar{x}, \bar{u}\right) \\ \tilde{L}\left(t, \bar{x}, \bar{u}\right) \end{bmatrix}, \tag{5.34}$$

represent the augmented state equations to be numerically integrated. This system is subject to initial conditions of the form

$$\tilde{x}\left(0\right) = \begin{bmatrix} \bar{x}_0 \\ 0 \end{bmatrix}. \tag{5.35}$$

Linearization of the system in Equation (5.34) yields

$$\delta\dot{\tilde{x}}\left(t\right) = \tilde{A}\left(t\right)\delta\tilde{x}\left(t\right) + \tilde{B}\left(t\right)\delta\bar{u}\left(t\right), \tag{5.36}$$

where

$$\tilde{A}\left(t\right) = \begin{bmatrix} \frac{\partial \bar{f}}{\partial \bar{x}} & \frac{\partial \bar{f}}{\partial x_{n+1}} \\ \frac{\partial \tilde{L}}{\partial \bar{x}} & \frac{\partial \tilde{L}}{\partial x_{n+1}} \end{bmatrix} = \begin{bmatrix} A\left(t\right) & 0 \\ \frac{\partial \tilde{L}}{\partial \bar{x}} & 0 \end{bmatrix}, \tag{5.37}$$

and

$$\tilde{B} = \begin{bmatrix} 0_3 \\ I_3 \\ 0 \end{bmatrix}. \tag{5.38}$$

The solution to the linear system in Equation (5.36) is known to be of the form,

$$\delta\tilde{x}_{i+1}^{-} = \tilde{\Phi}\left(t_{i+1}, t_i\right)\delta\tilde{x}_i^{+} + \int\limits_{t_i}^{t_{i+1}} \tilde{\Phi}\left(t, \tau\right)\tilde{B}\left(\tau\right)\delta\bar{u}\left(\tau\right)d\tau, \tag{5.39}$$

where $\tilde{\Phi}\left(t_{i+1}, t_i\right)$ is the state transition matrix, for the i^{th} segment, in the augmented nonlinear system. This matrix is determined by numerically integrating

$$\dot{\tilde{\Phi}}\left(t, t_i\right) = \tilde{A}\left(t\right)\tilde{\Phi}\left(t, t_i\right), \tag{5.40}$$

subject to $\tilde{\Phi}\left(t_i, t_i\right) = I_{(n+1)}$. In Equation (5.39), the superscript '+' denotes initial conditions at the start of a numerically integrated segment while the '$-$' represents the numerically integrated state at the end of a segment. As previously discussed, there are two ways to implement a discrete control approach; impulsive control or constant thrust arcs. The choice of control methodology determines how the control gradient in Equation (5.31) is computed. Of course, the partial derivative in Equation (5.30) is simply the state transition matrix,

$$\frac{\partial\tilde{F}_i}{\partial\tilde{x}_i} = \tilde{\Phi}\left(t_i, t_{i-1}\right), \tag{5.41}$$

regardless of the control methodology implemented.

5.4.1 Impulsive Control

If an impulsive control algorithm is sought, the integral term in Equation (5.39) vanishes and the resulting solution can be rewritten as follows,

$$\begin{aligned} \partial\tilde{x}_{i+1}^{-} &= \tilde{\Phi}\left(t_{i+1}, t_i\right)\delta\tilde{x}_i^{+}, \\ &= \tilde{\Phi}\left(t_{i+1}, t_i\right)\left(\delta\tilde{x}_i^{-} + \tilde{B}\Delta\bar{V}_i\right), \\ &= \tilde{\Phi}\left(t_{i+1}, t_i\right)\delta\tilde{x}_i^{-} + \tilde{\Phi}\left(t_{i+1}, t_i\right)\tilde{B}\Delta\bar{V}_i. \end{aligned} \tag{5.42}$$

The control input, in this case, is denoted by an impulsive maneuver ($\Delta\bar{V}_i$).

Equation (5.42) implies that the end state of the previous segment, after applying an impulsive maneuver, becomes the initial state at the beginning of the next segment. Note, from Equation (5.42), that

$$\frac{\partial \tilde{F}}{\partial \bar{u}_i} = \tilde{\Phi}\left(t_{i+1}, t_i\right) \tilde{B}. \tag{5.43}$$

The partial derivatives in Equations (5.41) and (5.43) are employed in evaluating the optimality conditions in Equations (5.30) and (5.31).

5.4.2 Constant Thrust Arcs

If, instead, constant thrusting over the length of each segment is desired, the determination of the control gradient, numerically, requires some additional consideration. In this case, the control input under the integral in Equation (5.39) is constant. Thus, the solution to the linear system is given by

$$\partial \tilde{x}_{i+1}^{-} = \tilde{\Phi}\left(t_{i+1}, t_i\right) \delta \tilde{x}_i^{+} + \left[\int_{t_i}^{t_{i+1}} \tilde{\Phi}\left(t, \tau\right) \tilde{B}\left(\tau\right) d\tau\right] \delta \bar{u}_i. \tag{5.44}$$

Note that this expression may also be written as follows,

$$\partial \tilde{x}_{i+1}^{-} = \left(\frac{\partial \tilde{F}_i}{\partial \tilde{x}_i}\right) \delta \tilde{x}_i^{+} + \left(\frac{\partial \tilde{F}_i}{\partial \bar{u}_i}\right) \delta \bar{u}_i, \tag{5.45}$$

where

$$\frac{\partial \tilde{F}_i}{\partial \tilde{x}_i} = \tilde{\Phi}\left(t_{i+1}, t_i\right), \tag{5.46}$$

and

$$\frac{\partial \tilde{F}_i}{\partial \bar{u}_i} = \int_{t_i}^{t_{i+1}} \tilde{\Phi}\left(t, \tau\right) \tilde{B}\left(\tau\right) d\tau. \tag{5.47}$$

The matrix $\tilde{\Phi}\left(t, \tau\right)$ is not actually available directly from the numerical integration. However, it can be computed at each instant in time based on the properties of the state transition matrix,

$$\tilde{\Phi}\left(t, t_i\right) = \tilde{\Phi}\left(t, \tau\right) \tilde{\Phi}\left(\tau, t_i\right). \tag{5.48}$$

From Equation (5.48), it is apparent that

$$\tilde{\Phi}\left(t,\tau\right)=\tilde{\Phi}\left(t,t_i\right)\tilde{\Phi}\left(\tau,t_i\right)^{-1}. \tag{5.49}$$

Substitution of Equation (5.49) into (5.47) reveals that the control gradient may be determined as

$$\frac{\partial\tilde{F}_i}{\partial\bar{u}_i}=\tilde{\Phi}\left(t,t_i\right)\int\limits_{t_i}^{t}\tilde{\Phi}\left(\tau,t_i\right)^{-1}\tilde{B}\left(\tau\right)d\tau. \tag{5.50}$$

Thus, solving the optimal control problem for constant thrusting requires that Equations (5.34) and (5.40) be numerically integrated along with

$$\dot{\tilde{\Phi}}^{*}\left(t,t_i\right)=\tilde{\Phi}\left(t,t_i\right)^{-1}\tilde{B}\left(t\right). \tag{5.51}$$

In the above expression, $\tilde{\Phi}^{*}$ is an $(n+1)\times 3$ matrix subject to $\tilde{\Phi}^{*}\left(t_i,t_i\right)=0$.

5.4.3 Application of Impulsive Optimal Control to Formation Keeping

Let the path dependent term, in Equation (5.33), be characterized by

$$\tilde{L}=\frac{1}{2}\left(\bar{x}-\bar{x}^{\circ}\right)^{T}Q\left(\bar{x}-\bar{x}^{\circ}\right), \tag{5.52}$$

where Q represents the state error weighting matrix and $\bar{x}^{\circ}$ denotes the nominal state vector of the deputy with respect to the chief spacecraft. Furthermore, let the end state term of the cost function be defined as

$$\tilde{\phi}\left(t_N\right)=\frac{1}{2}\left(\bar{x}_N-\bar{x}_N^{\circ}\right)^{T}W\left(\bar{x}_N-\bar{x}_N^{\circ}\right)+x_{n+1}\left(t_N\right), \tag{5.53}$$

where W represents the end state weighting matrix and $\bar{x}_N^{\circ}$ is the nominal state of the deputy at the END of the mission. Both Q and W are symmetric positive definite matrices. Given these definitions, the boundary condition for the co-state vector is

$$\tilde{\lambda}_N^{T}=\frac{\partial\tilde{\phi}_N}{\partial\tilde{x}_N}=\begin{bmatrix}\left(\bar{x}_N-\bar{x}_N^{\circ}\right)^{T}W & 1\end{bmatrix}, \tag{5.54}$$

and the linear system matrix is given by

$$\tilde{A}\left(t\right)=\begin{bmatrix}A\left(t\right) & 0\\ \left(\bar{x}-\bar{x}^{\circ}\right)^{T}Q & 0\end{bmatrix}. \tag{5.55}$$

Now, a truly optimal approach requires that the control input at each node be optimized simultaneously. In the CR3BP or EPHEM models, this can prove to be computationally inefficient since no analytical solution is available. Thus, for every iteration of the optimizer, particularly for gradient based methods, each segment may require multiple integrations. This is further complicated by the fact that a particular mission trajectory potentially includes many nodes. Since there are three control variables per node, that is a total of $3\,(N-1)$ parameters for optimization. One may infer, from this observation, that a nearly continuous optimal approach can be extremely numerically intensive due to the increased number of nodes.

5.4.4 Numerical Solution Approach

In the following examples, the optimization problem is approached from two different perspectives. In the "global" approach the control sequence is optimized across all segments simultaneously. Note that the term "global" is used loosely and it is NOT meant to imply that the resulting solution is itself globally optimal. As previously mentioned, the Euler-Lagrange optimality conditions are based on the calculus of variations. Hence, any optimal solution that is identified through this approach exists in the vicinity of the initial guess and, thus, represents a local optimal. No further conclusions can be drawn about the overall optimality of the solution based on this approach. An alternative to this "global" methodology is the "segment-by-segment" approach. In this case, each segment is optimized individually and sequentially.

It is important to note that the goal of this investigation is NOT the identification of the most efficient numerical solution process. Rather, the examples presented here are intended to demonstrate that the theory developed in this section leads to a local optimal solution in the nonlinear model. To validate the theoretical development, the actual numerical identification of the local optimal solution is based on the large-scale method [54, 55] available in MATLAB through the function *fminunc*.

This particular method attempts to find a minimum of a scalar function, J, of several variables, $\bar{u}_{in}$, based on some initial estimate and analytically available gradients, $H_{\bar{u}_{in}}$. The cost functions defined in this section are scalar and, as previously mentioned, depend on $3(N-1)$ control input variables, 3 variables per node. To solve the optimal control problem numerically, the control vector, and the associated gradient at every node, are each reshaped into a single vector with $3(N-1)$ components such that $\bar{u}_{in}(3(j-1)+1:3(j-1)+3) = [u_x(t_{j-1}), u_y(t_{j-1}), u_z(t_{j-1})]$ and $H_{\bar{u}_{in}}(3(j-1)+1:3(j-1)+3) = [H_{u_x}(t_{j-1}), H_{u_y}(t_{j-1}), H_{u_z}(t_{j-1})]$ for $j = 1, \ldots, N$. In this case $H_{u_x} = \frac{\partial H}{\partial u_x}$, $H_{u_y} = \frac{\partial H}{\partial u_y}$, and $H_{u_z} = \frac{\partial H}{\partial u_z}$. For simplicity, the solutions presented here are determined in the CR3BP.

Depending on the numerical solution process selected, the “segment-by-segment” approach may lead to vast improvements in computation speed for a small sacrifice in overall optimality. To illustrate the level of improvement, suppose the optimizer seeks to minimize the state error over the duration of the mission, that is, 180 days for the examples presented here. A “segment-by-segment” approach may require 20 minutes to identify the local optimal solution, if the initial guess is based on the state corrector previously presented. The “global” approach, may require days to identify a local optimal solution that is only slightly better than the one identified through the “segment-by-segment” approach. Of course, the actual computation times will vary according to the optimizer selected and the computing platform. The results presented in this section are based on computations performed within MATLAB, in the CR3BP, using *fminunc*. All computations are performed on a Linux-based dual processor (2 × 1.8 GHz Intel Xeon) computer with 1-gigabyte of available memory.

The time required to numerically identify the local optimal is significantly affected by the sensitivity of the dynamical regime near the libration points. That is, seemingly minuscule changes in the control inputs can lead to significant changes in the path of the deputy. In the “global” approach, this sensitivity is compounded since the method attempts to optimize all $3(N-1)$ inputs simultaneously.

In essence, the dynamical sensitivity of the model forces the optimizer to seek a solution following a sequence of extremely small steps. This is not surprising since the small changes implemented at the beginning of the mission can lead to significant changes at the end of the mission.

It is also important to note that the tolerance levels required to establish a solution as optimal should not exceed 10^{-10}, assuming the solution is determined in terms of non-dimensional state variables. For the numerical integration of each segment, the tolerance level should not exceed 10^{-12} in the CR3BP. Larger tolerances may lead to incorrect results in the CR3BP. It is important to remember that, regardless of the choice of optimizer, this dynamical sensitivity is always present. Furthermore, in future studies, it may be possible to expedite the determination of the optimal solution by selecting an alternate scaling for the state variables.

Numerical Example - Minimize State Error

Consider a mission that requires the deputy spacecraft to maintain a complete state, relative to the chief, characterized by $\bar{r} = (50\text{ m})\,\hat{z}$ and $\dot{\bar{r}} = \bar{0}$. Let the state error weighting matrix be defined as $Q = diag(1 \times 10^{12}, 1 \times 10^{12}, 1 \times 10^{12}, 1 \times 10^{6}, 1 \times 10^{6}, 1 \times 10^{6})$. The time history of the radial error for various end state weightings is plotted in Figure 5.11. The dashed red curve represents the solution determined from a standard state corrector, where the maneuvers are computed from Equation (5.2). The blue curve is associated with the optimal control without end point weighting, $W = 0$. Note that the response in blue alternates in amplitude. That is because the end state error is not constrained in this particular solution. Hence, the optimal path is allowed to overshoot the nominal as long as the overall segment error is minimized. The intermediate green curve is generated when some end point weighting is incorporated into the solution process, i.e., $W = 1 \times 10^{-2} Q$.

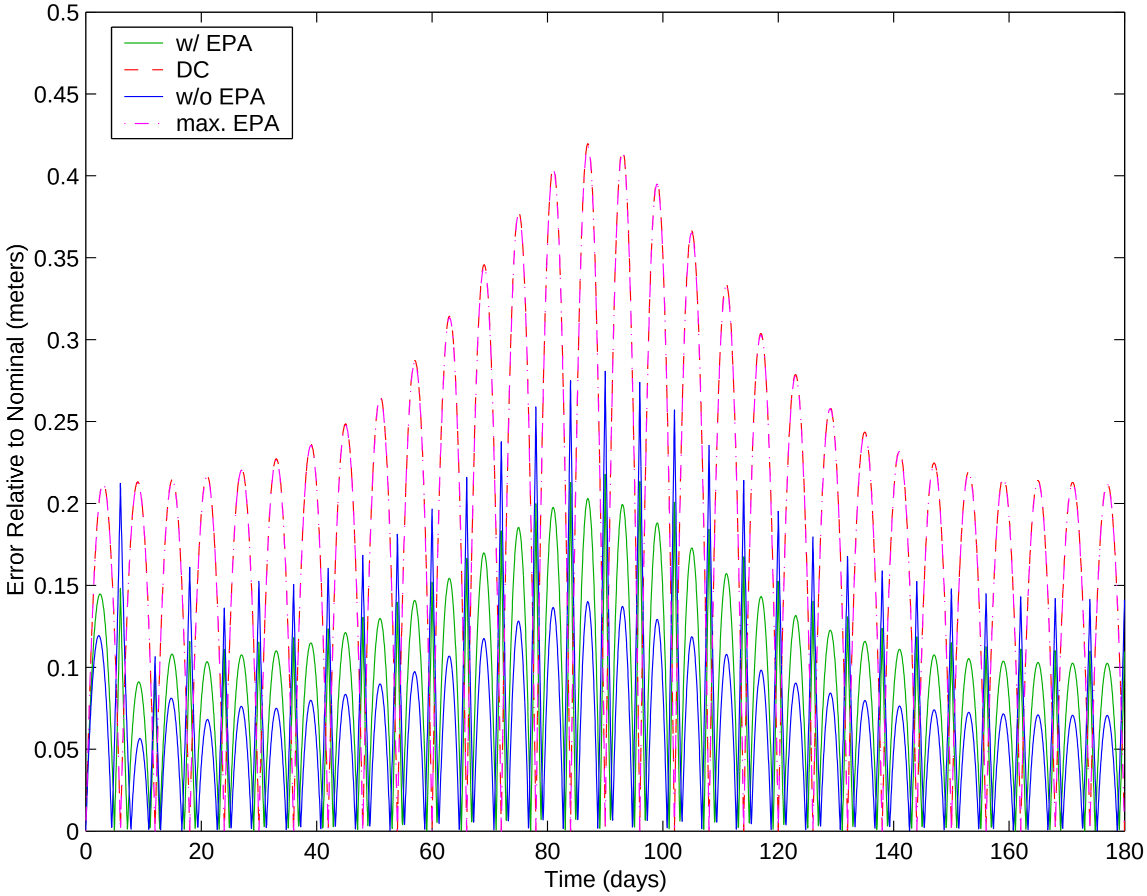

Figure 5.11. Comparison of State Corrector vs. Optimal Impulsive Controller for a 50 m Formation Near an L_2 Halo Orbit (CR3BP)

If the end point weighting is increased, the optimal solution, identified as the magenta curve in Figure 5.11, eventually converges on the initial guess. That is, the response computed from the state differential corrector. This is not surprising since, in this case, the initial guess already satisfies the end state constraint. The red and magenta curves may be difficult to discern from this figure since they are essentially equal. However, they both incur the largest deviations relative to the nominal path.

The optimal solution curves presented in Figure 5.11 are associated with the segment-by-segment approach previously described. The segment-by-segment method is most computationally efficient when the trajectory is divided into many nodes over long periods of time. It is also possible, however, to determine the optimal maneuver scheme based on a "global" approach. In this case, all maneuvers are simultaneously optimized over the length of the mission. The efficiency of these two methods, for a 180 day mission, is contrasted in Figures 5.12-5.13.

For a nominal path characterized by $\bar{r}^{\circ}(t) = 5000\hat{z}$, the radial error response is presented in Figure 5.12. The results obtained via a state differential corrector, the segment-by-segment method, and the global approach are represented as three separate curves in Figure 5.12. The value of the scalar cost function, as a function of time, appears in Figure 5.13. Note that the only value of interest on this figure is the final value, $x_{n+1}(t_f)$. It is apparent, from Figure 5.13, that over long mission durations, the segment-by-segment approach is almost as effective as the global method. Although, numerically, the global approach still proves to be the true optimal solution. Either approach appears well suited in terms of reducing the overall error relative to the nominal, as deduced from Figure 5.12. The most interesting and revealing information obtained from the application of these methodologies, comes from the optimal maneuver schedule in Figure 5.14. Three plots are presented in this figure. Let ΔV° denote the maneuver history associated with the state corrector, used as an initial guess in solving the optimal control problem. Figure 5.14 depicts the difference between the optimal maneuver history and ΔV° in mm/sec.

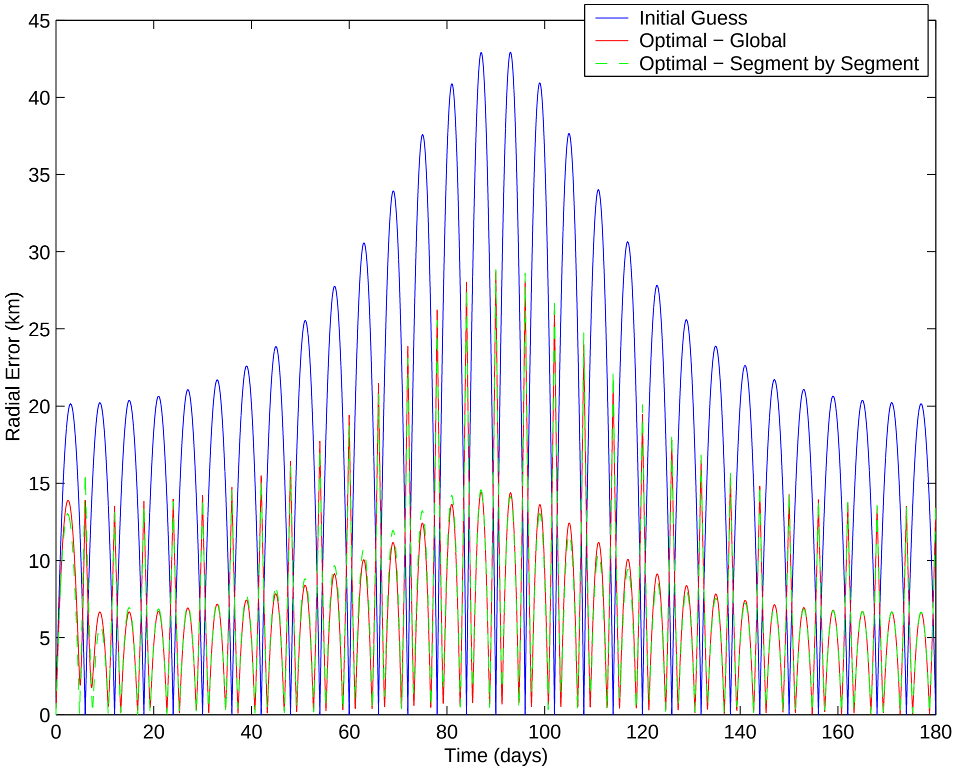

Figure 5.12. Radial Error Response – Global vs. Segment-by-Segment Approach Applied to a 5000 km Formation Near an L_2 Halo Orbit (CR3BP)

The maneuver histories associated with both the global and the segment-by-segment methods are plotted in terms of the x-, y-, and z- components of the resulting ΔV time history. Given the highly sensitive nature of this dynamical regime, a formation that requires a nominal separation of 5000 km is very susceptible to small changes in the control inputs. This is particularly true as the time between maneuvers is increased. A small input results in significant change at the end of each segment. In this case, these small changes – on the order of mm/sec – reduce the overall error by almost 10 km 90 days into the mission. This particular time interval is associated with the point along the halo orbit that is closest to the xy-plane. It is also worth noting that, the global approach, in this case, is extremely computationally intensive and requires more than one day of processing time to generate a solution.

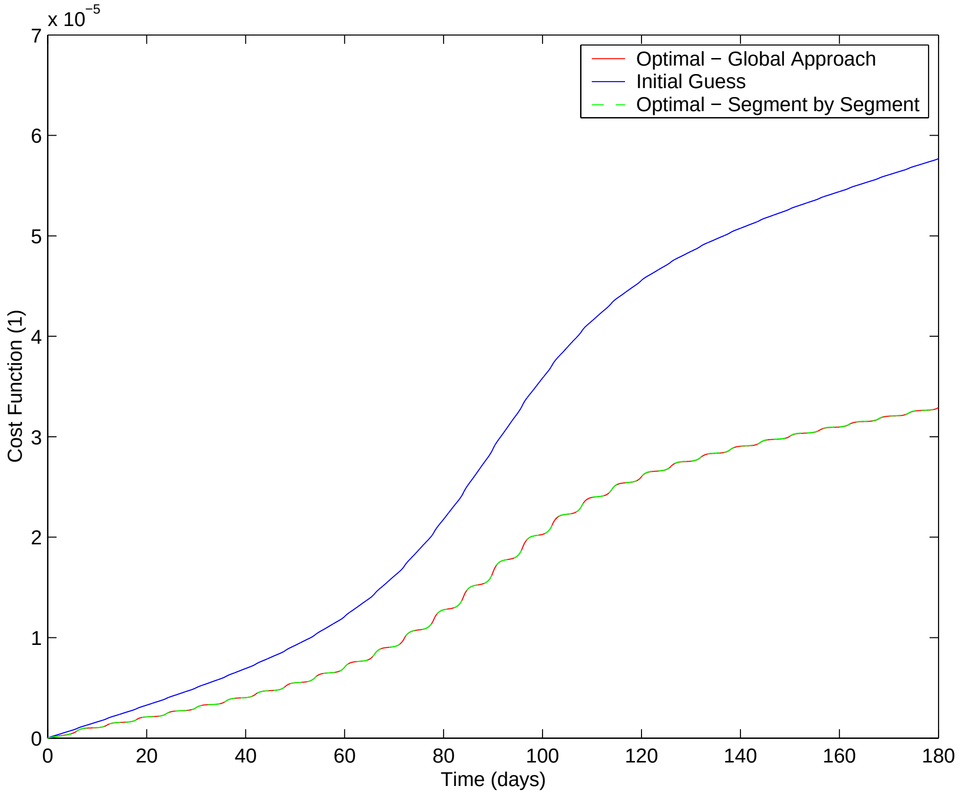

Figure 5.13. Cost Function – Global vs. Segment-by-Segment Approach Applied to a 5000 km Formation Near an L_2 Halo Orbit (CR3BP)

The segment-by-segment approach, on the other hand, is successful within minutes. Since the results from the two methodologies are comparable it appears that the segment-by-segment method represents a reasonable alternative to the global approach.

5.4.5 Numerical Example - Minimize Range and Range Rate Error

Missions like MAXIM and TPF require that the deputies in the formation track some pre-specified state vector. However, for other missions, it may be sufficient to maintain the deputy at a constant relative distance from the chief vehicle. The radial targeter presented in this chapter proves to be most effective in accomplishing such a task.

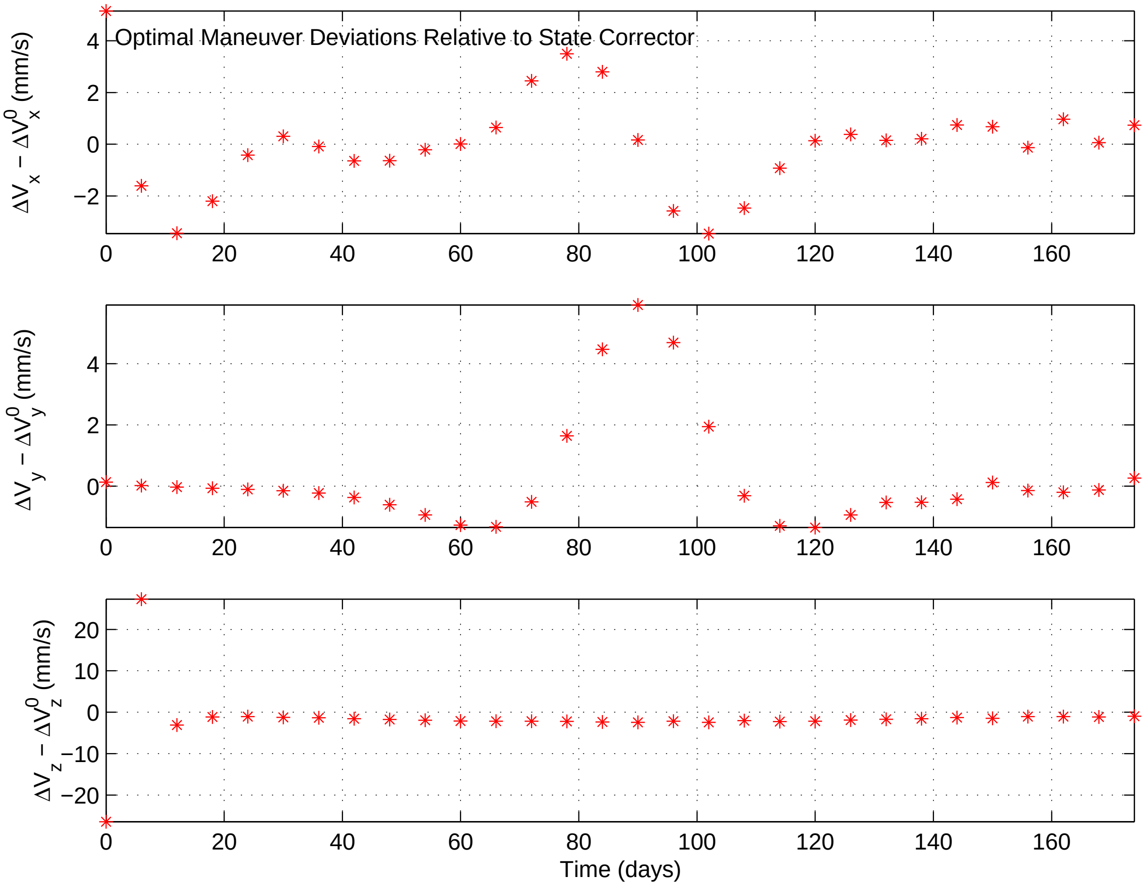

Figure 5.14. Maneuver Scheme – Global vs. Segment-by-Segment Approach Applied to a 5000 km Formation Near an L_2 Halo Orbit (CR3BP)

In contrast to the state corrector, the deviations from the specified nominal radial distance are minimal in comparison to the deviations incurred by the state targeter. The solution obtained from the radial targeter can also serve as an initial guess to the optimal impulsive control scheme described here. In this case, the cost function can be expressed as

$$\tilde{L} = \frac{1}{2} q \left(r - r^{\circ}\right)^2 . \tag{5.56}$$

The goal of the optimal control law, associated with the above definition, is to minimize the range error between the deputy and chief vehicles over the duration of the mission. Note that the weighing factor q is actually necessary – for the examples considered here – because the initial guess, from the radial corrector, is very close to the optimal solution, as is apparent in Figure 5.15. In this figure, the radial distance between the chief and deputy vehicle is plotted over a period of 180 days. Three curves are depicted. The dash-dot red curve represents the initial guess for the optimizer. The dashed green curve is the optimal solution associated with the "segment-by-segment" approach. Finally, the solid blue line represents the optimal solution determined from the "global" approach. Although there is visible improvement between the initial guess and the optimal solutions, it is not as significant as that determined in the previous section for state tracking example. Recall that, in the previous example, a 5000 km formation incurred an error of up to 40 km between maneuvers via the corrector scheme. In the present example, the radial corrector leads to errors under 3 km for a nominal 5000 km separation.

In tracking the radial distance, although the "segment-by-segment" and "global" methods lead to similar solutions, the "global" approach leads to the true optimal, as deduced from Figure 5.16. In this figure, the final value of the cost function represents the quantity that is actually optimized, $x_{n+1}(t_N)$. It is evident, from Figure 5.16, that the "optimal" exhibits only marginal improvement over the solution determined with the radial corrector. The optimal maneuver history associated with the path in Figure 5.15 is plotted in Figure 5.17.

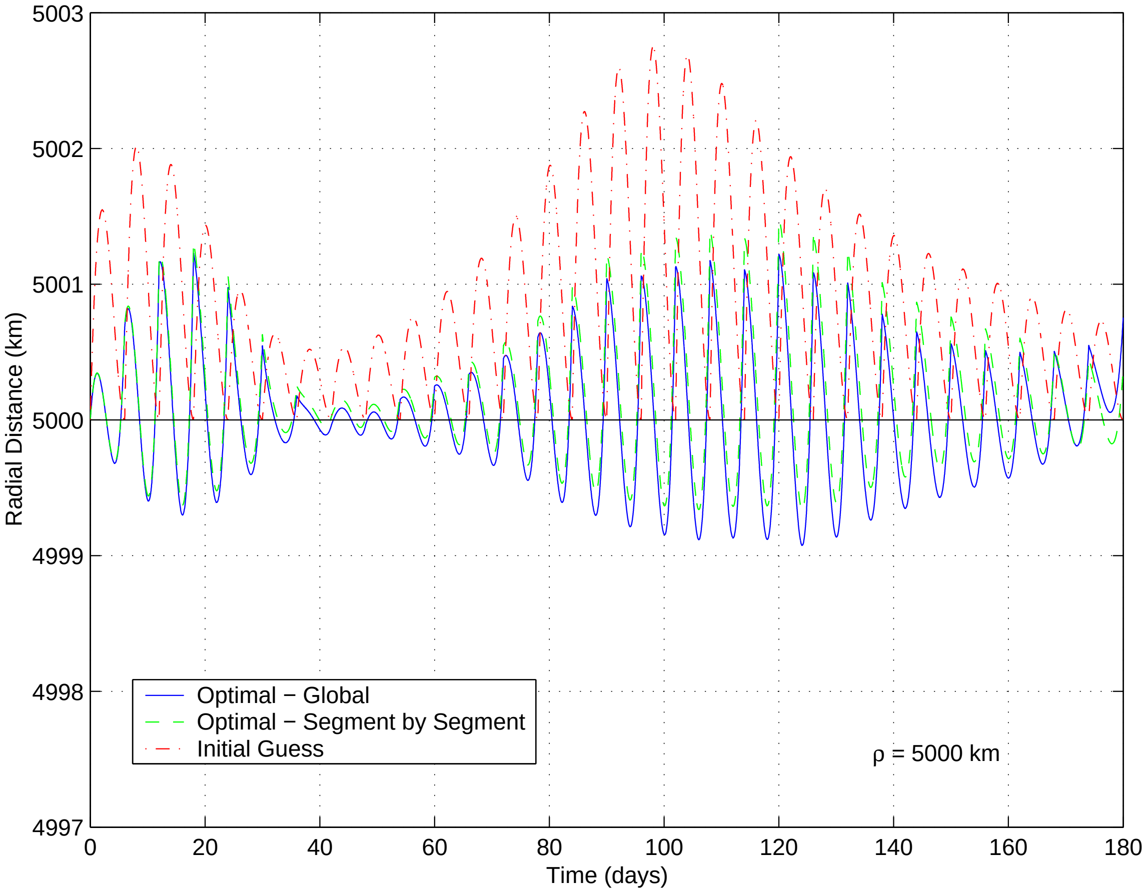

Figure 5.15. “Global” Optimal Solution for Radial Tracking

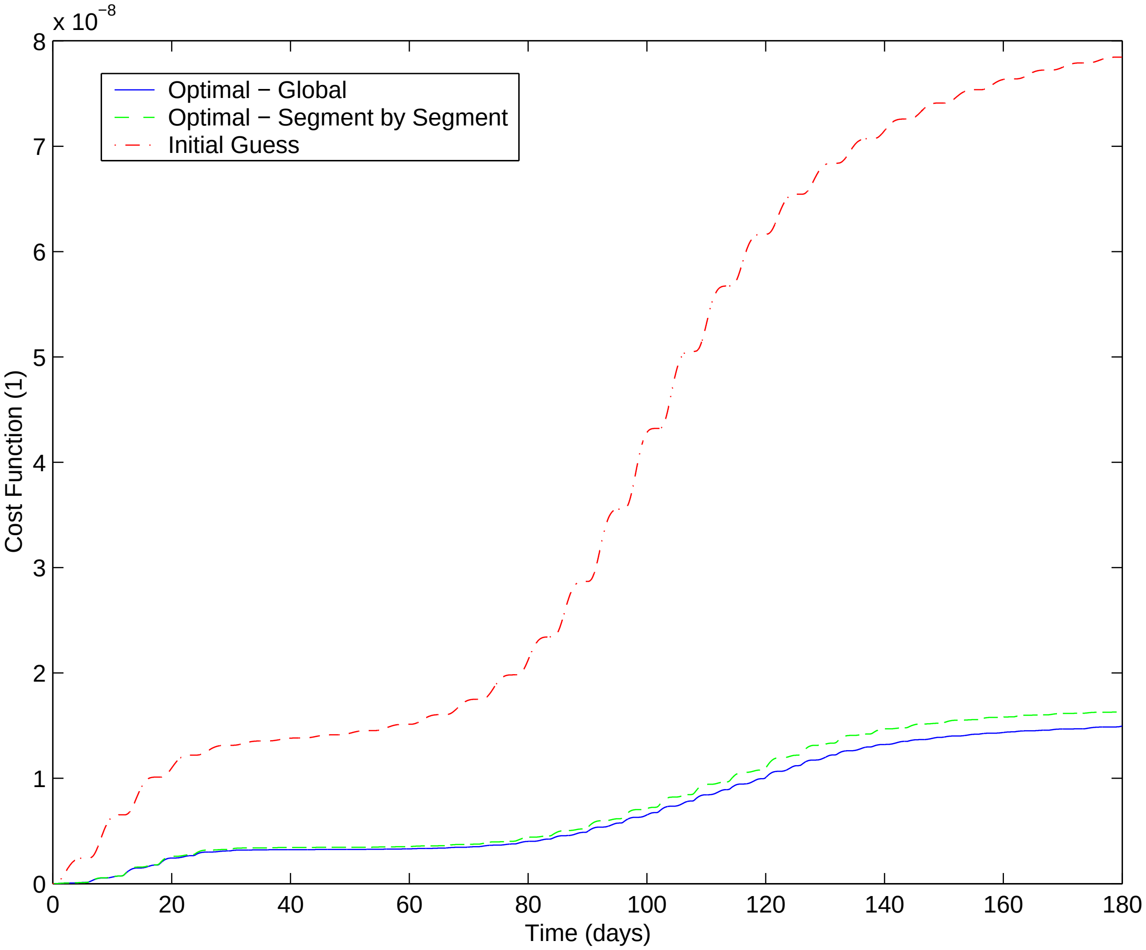

Figure 5.16. Cost Functional (Non-Dimensional) for Radial Tracking Example

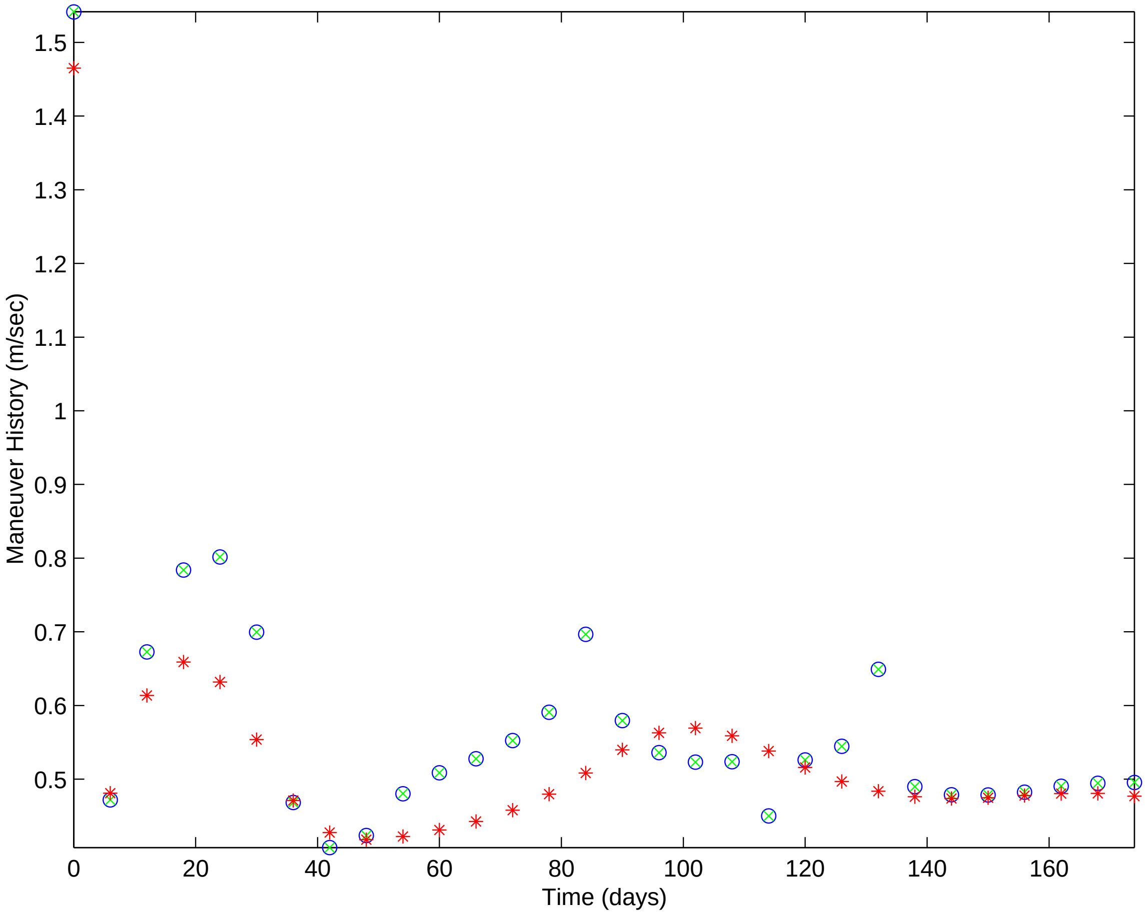

Figure 5.17. Maneuver History for Radial Tracking Example

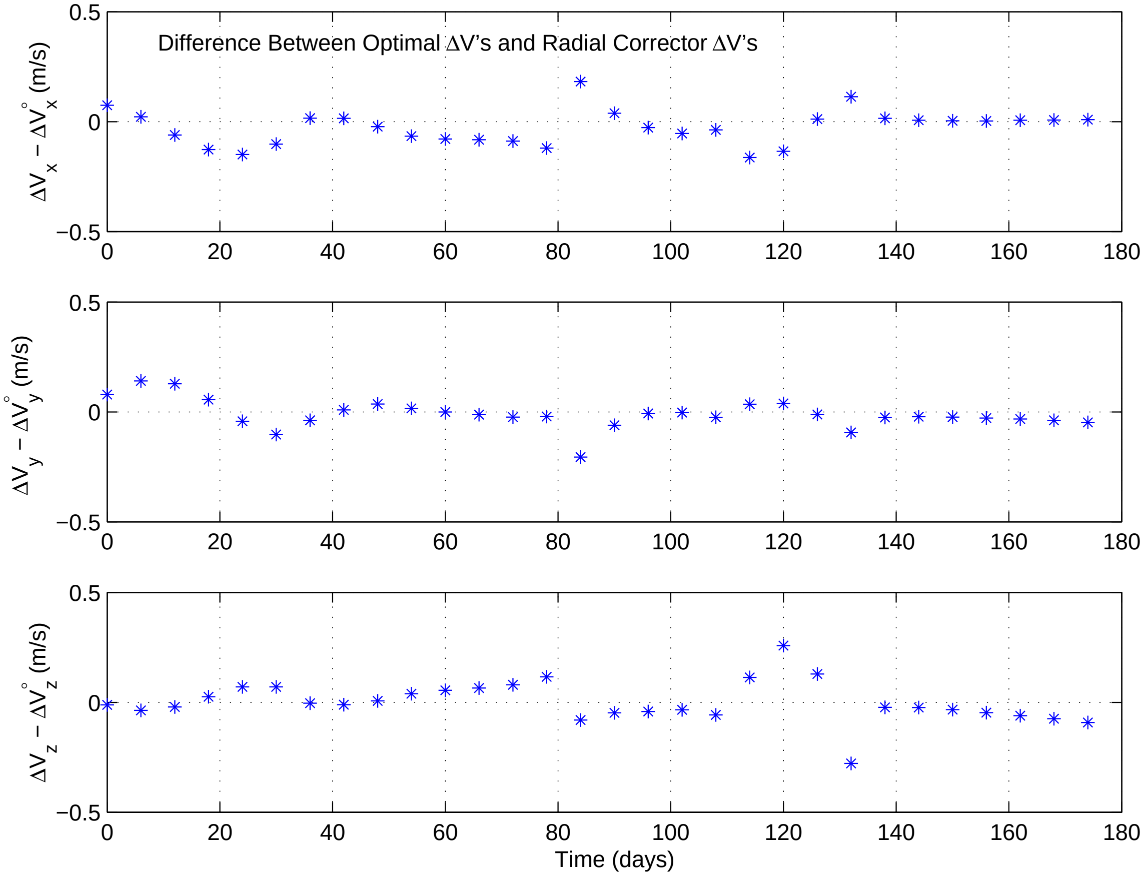

Figure 5.18. Maneuver Comparison to Radial Corrector Results

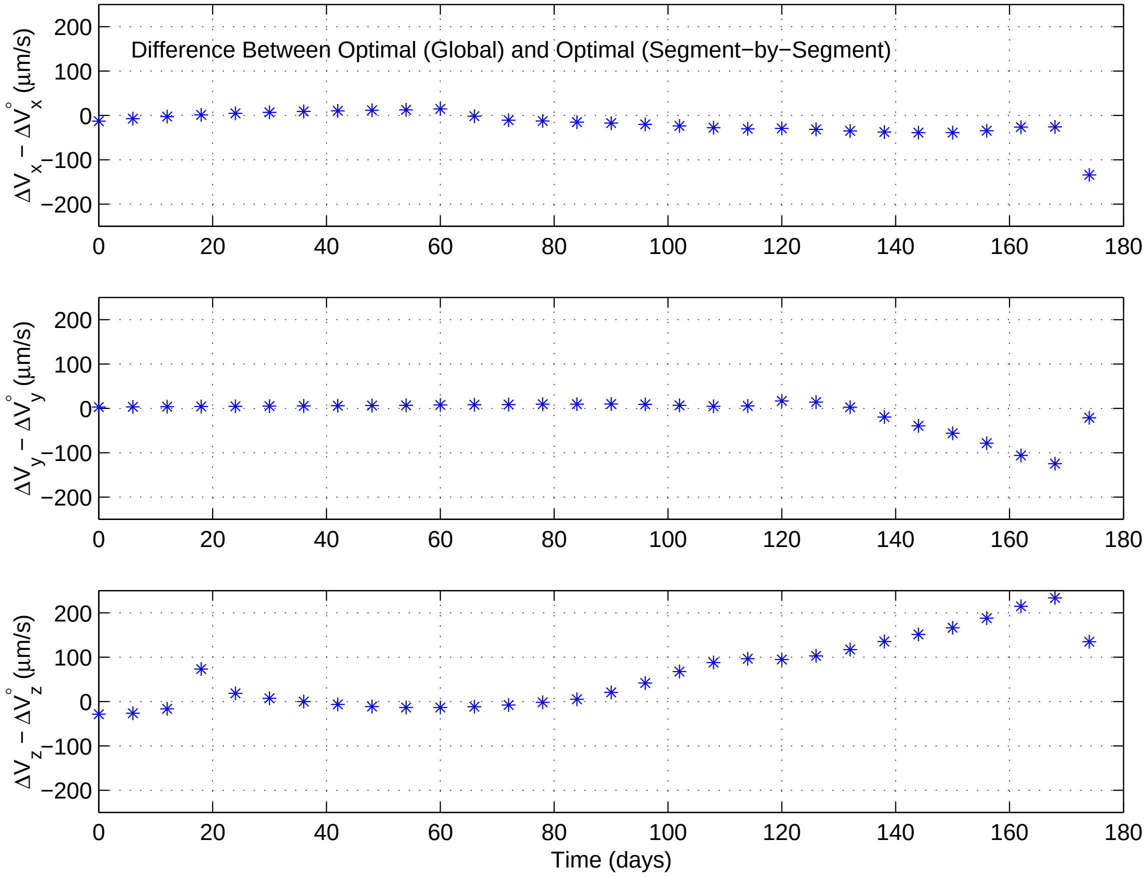

Figure 5.19. “Segment-by-Segment” vs “Global” Approach Optimal Maneuver Comparison

Although the difference between the maneuvers determined with the radial corrector and the optimal control law are visible, as further demonstrated in Figure 5.18, the two optimal approaches converged onto similar solutions. Figure 5.19 highlights the difference between the control inputs as determined from the "segment-by-segment" and "global" methods. These differences are only on the order of 10^{-6} m/sec and, yet, such small inputs are enough to generate a visible difference in the optimal solution, as observed in Figure 5.15. The differences in the optimal path are most visible near the end of the mission. Another indication of the dynamical sensitivity of the model.

Recall that the goal of the radial corrector is to minimize the range error at the end of each segment rather than over the duration of the mission. Since the optimal solution is so close to the initial guess, in this case, if no weighing q is present the numerical process will assume that the optimal has been achieved without ever actually computing an optimal control effort. The weighting depends on the nominal relative separation between the vehicles. For instance, a 5000 km nominal radial distance requires a weighting – in the non-dimensional equations – of 1×10^8 while a 50 m formation requires a weighting on the order of 1×10^{12}. This further validates the observation that an alternate scaling of the state variables may, at a later time, prove to be beneficial in reducing the time required to identify an optimal solution. Such re-scaling may also allow for larger tolerances during the optimization process.

6. Concluding Remarks

Some of the currently proposed formation flight missions, like TPF and MAXIM, impose many constraints on the dynamical evolution of the nominal configuration. The tolerances imposed on these constraints are extremely small, on the order of microns in position or micro-arcseconds in orientation for missions like MAXIM. As demonstrated in this study, these constraints are not consistent with the natural flow near the libration points. Hence, if highly precise formation keeping is necessary, at least nearly continuous control must be applied. An added constraints of some missions, like MAXIM, specify that the thrusters must be deactivated during the science collection phase. As demonstrated in this study, deactivating the thrusters for the MAXIM configuration can quickly drive the vehicles outside of the required position tolerances within minutes.

Since the region near the libration points is inherently unstable, as well as sensitive, the natural unforced response drives the vehicles away from the nominal path rapidly. This high sensitivity to small perturbations may or may not be beneficial depending on the goal of the mission. For a single spacecraft scenario, such as ISEE-3 [56], Genesis, or Map, this sensitivity is advantageous within the context of vehicle maintenance, that is, a small correction is sufficient to maintain the spacecraft in the vicinity of the reference path. However, unlike formation flight missions such as MAXIM and TPF, none of these single spacecraft missions seek to enforce the reference solution to within microns. The difference here is that the reference motion is defined in terms of the relative dynamics of multiple vehicles.

Tight formation specifications is one of the most difficult aspects of formation flight near the libration points. For instance, often the corrections (continuous or discrete) necessary may be too small and subsequently undeliverable by the on-board propulsion system.

However, if these corrections are not applied, the prescribed tolerances may not be satisfied. Even if the required propulsive technology becomes available, physically implementing these minuscule thrust levels can introduce errors that may be on the same order of magnitude as the nominal thrust. This is a potentially significant problem given the dynamical sensitivity to small perturbations that is characteristic of this regime. In addition, continuous thruster operation may not always represent a desirable option for a particular mission. The thrusters can interfere with the science phase of a mission. In this case, any formation keeping strategies must rely on discrete control to allow for thruster on/off sequences. However, it is important to note that any discrete approach precludes precise formation keeping if the specified tolerances are too small, as is the case for MAXIM.

In light of these mission constraints, the initial phase of this investigation seeks to develop, first, a more complete understanding of the natural formation dynamics. A Floquet analysis leads to a dynamical systems approach to identify natural nominal configurations as well as the associated stable manifolds for deployment. Based on this understanding, it is clear that space based interferometry missions, as presently envisioned, require nominal configurations that are not consistent with these natural dynamics. Hence, continuous control methods represent a significant aspect of this investigation.

Linear optimal control and nonlinear feedback linearization methods are successfully applied to a wide variety of nominal configurations. An interesting result, derived from this analysis, is that the LQR and Input Feedback Linearization methods can yield almost identical solutions. This is a significant result because the IFL approach greatly simplifies the numerical analysis in the EPHEM model. The results of this investigation further indicate that precise formation keeping may be possible, for certain types of configurations, if continuous thrusting represents a feasible option.

Configurations that require the relative state of the deputy spacecraft to remain fixed inertially, for instance, can lead to prohibitively small thrust levels if the nominal relative separation is less than 1 km. On the other hand, if the mission constraints allow the deputy vehicle to orbit the chief spacecraft, forcing the rotation rate to a constant value can drive the formation keeping costs into a more reasonable range.

Of course, in the event that continuous thruster operation is not possible, impulsive control is also investigated. The focus, initially, is on a targeter approach to formation keeping. Basically, the deputy spacecraft trajectory is divided into segments. Then, impulsive maneuvers are applied at the beginning of each segment to ensure that the end state is consistent with the desired nominal path. As the maneuvers become more closely spaced, the results of this approach converge onto the continuous control results determined in the initial phase of this study. The analysis presented here reveals that, a state targeter can lead to large deviations from the nominal path in-between maneuvers. A radial targeter, on the other hand, offers added dynamical flexibility and greatly reduces these deviations.

In addition to the approach of a basic targeter, a discrete optimal control scheme is devised here, in the full nonlinear model. The goal of this control law is to minimize the deviation from the nominal path during the thruster downtime, rather than at the end of each segment. The numerical solution process employs the targeter solution as an initial guess to an optimizer. This optimal control law offers great improvement over the targeter approach if the goal is to maintain a fixed relative state. However, if the goal is to enforce a constant radial distance, regardless of the spatial orientation of the deputy, the optimal solution is actually very close to the solution determined from the radial corrector.

After careful examination of a variety of formation keeping methodologies, the following conclusions are summarized from the analysis presented here:

- If precise formation keeping is required for a particular mission, at least nearly continuous thrusting must be available. That is, assuming that the relative state of the vehicles must be controlled to within extremely small tolerance levels, potentially in the sub-millimeter range.

- The nominal thrust levels may fall below the currently deliverable limits, depending on the nominal motion specified. In this case, precise formation keeping may not be possible near the libration points due to the highly sensitive nature of the dynamical flow.

- Thruster on/off sequences, such as those specified by MAXIM, preclude precise formation keeping if the tolerances are too small. That is, for instance, if the relative position of each vehicle must be controlled to within sub-millimeter accuracy.

- If the deputy vehicles are allowed to orbit the chief spacecraft at some fixed rotation rate, the nominal thrust required for formation keeping can increase to more reasonable levels. However, this also precludes thruster on/off sequences. Inducing a rotation rate can increase the tangential velocity of the deputy significantly. Hence, if the thrusters are deactivated the deputy will quickly diverge from its nominal path.

- As presently envisioned, space based interferometry requires that the state vector of each vehicle be controlled to within extremely small tolerances. This type of motion is inconsistent with the natural flow near the libration points. If, however, precise navigation is sufficient to accomplish the interferometry goals [57], natural formations may prove to be very beneficial.

- Through station keeping maneuvers, natural motions can be forced to follow non-natural paths, but only to some extent. The success of this approach depends on the non-natural motion that is specified.

6.1 Recommended Future Efforts

There are many aspects of this analysis that should be further addressed to enhance our present understanding of formation keeping near the libration points. The following list represents a summary of some of the areas that branch off from the present investigation.

- Optimal control, subject to bounded thrust inputs, is one of the most significant areas. This also includes the numerical methods associated with solving the optimal control problem in this highly nonlinear and sensitive problem.

- Of course, an added degree of complexity is introduced to this analysis if modeling and measurement uncertainties, as well as maneuver implementation errors, are introduced into the problem. This is particularly true for formations that seek to enforce relative vehicle positions within sub-millimeter accuracy. Hence, the sensitivity of any formation keeping strategy to these sources of error must ultimately be addressed as well. In the future, the results of such analysis may reshape how space based interferometry is accomplished.

- The actual implementation of any control scheme for multi-vehicle formations must also address collision avoidance between vehicles in the formation. This particular item should be included in the controller design as a penalty to be minimized.

- Further exploration of the natural formation dynamics may also prove valuable for certain types of formation flight missions. A blending of methodologies between the natural formations and the non-natural formation control, also presents many interesting prospects.

LIST OF REFERENCES

LIST OF REFERENCES

[1] EO-1 Overview. http://eo1.gsfc.nasa.gov/overview/eo1Overview.html.

[2] Techsat-21 Program Overview. http://www.vs.afrl.af.mil/TechProgs/TechSat21.

[3] R. H. Vassar and R. B. Sherwood. Formationkeeping for a Pair of Satellites in a Circular Orbit. *Journal of Guidance, Control, and Dynamics*, 8:235–242, March-April 1985.

[4] D. C. Redding, N. J. Adams, and E. T. Kubiak. Linear-Quadratic Stationkeeping for the STS Orbiter. *Journal of Guidance, Control, and Dynamics*, 12:248–255, March-April 1989.

[5] Y. Ulybyshev. Long-Term Formation Keeping of Satellite Constellation Using Linear Quadratic Controller. *Journal of Guidance, Control, and Dynamics*, 21(1):109–115, January-February 1998.

[6] V. Kapila, A. G. Sparks, J. M. Buffington, and Q. Yan. Spacecraft Formation Flying: Dynamics and Control. *Journal of Guidance, Control, and Dynamics*, 23(3):561–563, May-June 2000.

[7] A. G. Sparks. Satellite Formationkeeping Control in the Presence of Gravity Perturbations. In *Proceedings of the American Control Conference*, volume 2, Chicago, Illinois, June 2000.

[8] R. K. Yedevalli and A. G. Sparks. Satellite Formation Flying Control Design Based on Hybrid Control System Stability Analysis. In *Proceedings of the American Control Conference*, volume 3, Chicago, Illinois, June 2000.

[9] D. J. Irvin Jr. and D. R. Jacques. Linear vs. Nonlinear Control Techniques for the Reconfiguration of Satellite Formations. In *Proceedings of the AIAA Guidance, Navigation, and Control Conference and Exhibit*, Montreal, Canada, August 2001. AIAA Paper 2001-4089.

[10] D. T. Stansbery and J. R. Cloutier. Nonlinear Control of Satellite Formation Flight. In *Proceedings of the AIAA Guidance, Navigation, and Control Conference and Exhibit*, Denver, Colorado, August 2000. AIAA Paper 2000-4436.

[11] S. R. Vadali, S. S. Vaddi, K. Naik, and K. T. Alfriend. Control of Satellite Formations. In *Proceedings of the AIAA Guidance, Navigation, and Control Conference and Exhibit*, Montreal, Canada, August 2001. AIAA Paper 2001-4028.

[12] S. R. Starin, R. K. Yedavalli, and A. G. Sparks. Spacecraft Formation Flying Maneuvers Using Linear Quadratic Regulation with No Radial Axis Inputs. In *Proceedings of the AIAA Guidance, Navigation, and Control Conference and Exhibit*, Montreal, Canada, August 2001. AIAA Paper 2001-4029.

[13] C. Sabol, R. Burns, and C. McLaughlin. Satellite Formation Flying Design and Evolution. *Journal of Spacecraft and Rockets*, 38(2):270–278, April 2001.

[14] C. C. Chao, J. E. Pollard, and S. W. Janson. Dynamics and Control of Cluster Orbits for Distributed Space Missions. In *Proceedings of the AAS/AIAA Spaceflight Mechanics Meeting*, Breckenridge, Colorado, February 1999. AAS Paper 99-126.

[15] H. Schaub and K. T. Alfriend. Impulsive Spacecraft Formation Flying Control to Establish Specific Mean Orbit Elements. *Journal of Guidance, Control, and Dynamics*, 24(4):739–745, July-August 2001.

[16] Z. Tan, P. M. Bainum, and A. Strong. The Implementation of Maintaining Constant Distance Between Satellites in Elliptic Orbits. *Advances in the Astronautical Sciences*, 105:667–683, 2000.

[17] Z. Wang, F. Khorrami, and W. Grossman. Robust Adaptive Control of Satellite Formationkeeping for a Pair of Satellites. In *Proceedings of the American Control Conference*, volume 2, Chicago, Illinois, June 2000.

[18] M. S. de Queiroz, V. Kapila, and Q. Yan. Adaptive Nonlinear Control of Multiple S/C Formation Flying. *Journal of Guidance, Control, and Dynamics*, 23(3):385–390, May-June 2000.

[19] Q. Yan, G. Yang, V. Kapila, and M. S. de Queiroz. Nonlinear Dynamics and Output Feedback Control of Multiple Spacecraft in Elliptic Orbits. In *Proceedings of the American Control Conference*, volume 2, Chicago, Illinois, June 2000.

[20] D. J. Scheeres and N. X. Vinh. Dynamics and Control of Relative Motion in an Unstable Orbit. In *Proceedings of the AAS/AIAA Astrodynamics Specialists Conference*, Denver, Colorado, August 2000. AIAA Paper 2000-4135.

[21] P. Gurfil and N. J. Kasdin. Dynamics and Control of Spacecraft Formation Flying in Three-Body Trajectories. In *Proceedings of the AIAA Guidance, Navigation, and Control Conference and Exhibit*, Montreal, Canada, August 2001. AIAA Paper 2001-4026.

[22] P. Gurfil, M. Idan, and N. J. Kasdin. Adaptive Neural Control of Deep-Space Formation Flying. In *Proceedings of the American Control Conference*, volume 4, pages 2842–2847, Anchorage, Alaska, May 2002.

[23] N. H. Hamilton. Formation Flying Satellite Control Around the L_2 Sun-Earth Libration Point. Master's thesis, George Washington University, Washington, District of Columbia, December 2001.

[24] D. Folta, J. R. Carpenter, and C. Wagner. Formation Flying with Decentralized Control in Libration Point Orbits. In *International Symposium: Spaceflight Dynamics*, Biarritz, France, June 2000.

[25] B. T. Barden and K. C. Howell. Fundamental Motions Near Collinear Libration Points and Their Transitions. *Journal of the Astronautical Sciences*, 46(4):361–378, 1998.

[26] B. T. Barden and K. C. Howell. Formation Flying in the Vicinity of Libration Point Orbits. *Advances in Astronautical Sciences*, 99(2):969–988, 1998.

[27] B. T. Barden and K. C. Howell. Dynamical Issues Associated with Relative Configurations of Multiple Spacecraft Near the Sun-Earth/Moon L_1 Point. In *Proceedings of the AAS/AIAA Astrodynamics Specialists Conference*, Girdwood, Alaska, August 1999. AAS Paper 99-450.

[28] K. C. Howell and B. T. Barden. Trajectory Design and Stationkeeping for Multiple Spacecraft in Formation Near the Sun-Earth L_1 Point. In *Proceedings of the 50th IAF International Astronautical Congress*, Amsterdam, Netherlands, October 1999. IAF/IAA Paper 99-A707.

[29] G. Gómez, M. Lo, J. Masdemont, and K. Museth. Simulation of Formation Flight Near Lagrange Points for the TPF Mission. In *Proceedings of the AAS/AIAA Astrodynamics Specialists Conference*, Quebec, Canada, July-August 2001. AAS Paper 01-305.

[30] K. C. Howell and T. Keeter. Station-Keeping Strategies for Libration Point Orbits - Target Point and Floquet Mode Approaches. *Advances in the Astronautical Sciences*, 89(2):1377–1396, 1995.

[31] G. Gómez, K. C. Howell, J. Masdemont, and C. Simó. Station-keeping Strategies for Translunar Libration Point Orbits. *Advances in the Astronautical Sciences*, 99(2):949–967, 1998.

[32] K. C. Howell and B. G. Marchand. Control Strategies for Formation Flight in the Vicinity of the Libration Points. In *Proceedings of the AIAA/AAS Space Flight Mechanics Conference*, Ponce, Puerto Rico, February 2003. AAS Paper 03-113.

[33] B. G. Marchand and K. C. Howell. Formation Flight Near L_1 and L_2 in the Sun-Earth/Moon Ephemeris System Including Solar Radiation Pressure. In *Proceedings of the AAS/AIAA Astrodynamics Specialists Conference*, Big Sky, Montana, August 2003. AAS Paper No. 03-596.

[34] K. C. Howell and B. G. Marchand. Design and Control of Formations Near the Libration Points of the Sun-Earth/Moon Ephemeris System. In *Proceedings of the Space Flight Mechanics Symposium – Goddard Space Flight Center*, Greenbelt, Maryland, October 2003.

[35] R. J. Luquette and R. M. Sanner. A Non-Linear Approach to Spacecraft Formation Control in the Vicinity of a Collinear Libration Point. In *Proceedings of the AAS/AIAA Astrodynamics Specialists Conference*, pages 437–445, Quebec, Canada, July-August 2001.

[36] Earth Observing 1 (EO-1) Pulsed Plasma Thruster - Project Description. http://space-power.grc.nasa.gov/ppo/projects/eo1/eo1-ppt.html.

[37] J. Mueller. Thruster Options for Microspacecraft: A Review and Evaluation of Existing Hardware and Emerging Technologies. In *Proceedings of the 33rd AIAA/ASME/SAE/ASEE Joint Propulsion Conference & Exhibit*, Seattle, Washington, July 1997. AIAA Paper No. 97-3058.

[38] A. D. Gonzales and R. P. Baker. Microchip Laser Propulsion for Small Satellites. In *Proceedings of the 37th AIAA/ ASME/ SAE/ ASEE Joint Propulsion Conference and Exhibit*, Salt Lake City, Utah, July 2001. AIAA Paper No. 2001-3789.

[39] C. Phipps and J. Luke. Diode Laser-Driven Microthrusters - A New Departure for Micropropulsion. *AIAA Journal*, 40(2):310–318, February 2002.

[40] K. C. Howell and H. J. Pernicka. Numerical Determination of Lissajous Trajectories in the Restricted Three-Body Problem. *Celestial Mechanics*, 41(1-4):107–124, 1987/88.

[41] D. L. Richardson. Analytic Construction of Periodic Orbits About the Collinear Points. *Celestial Mechanics*, 22(3):241–253, October 1980.

[42] D. L. Richardson and N. D. Cary. A Uniformly Valid Solution for Motion about the Interior Libration Point of the Perturbed Elliptic-Restricted Problem. In *Proceedings of the AAS/AIAA Astrodynamics Specialists Conference*, Nassau, Bahamas, July 1975. AAS Paper No. 75-021.

[43] C. R. McInnes. *Solar Sailing: Technology, Dynamics and Mission Applications.* Praxis Publishing Ltd, United Kingdom, 1999.

[44] M. Corless. Control in the Presence of Actuator Lower Bounds. Private Communication, 2004.

[45] A. E. Bryson and Y. Ho. *Applied Optimal Control: Optimization, Estimation, and Control.* Hemisphere Pub. Corp., New York, 1975.

[46] J. E. Slotine and W. Li. *Applied Nonlinear Control.* Prentice Hall, New Jersey, 1991.

[47] G. Chen, J. Fang, Y. Hong, and H. Qin. *Introduction to Chaos Control and Anti-Control*, volume 40 of *Advanced Topics in Nonlinear Control Systems: World Scientific Series on Nonlinear Science. Series A.* World Scientific Publishing, New Jersey, 2001.

[48] A. F. Shipley, W. C. Cash, and M. K. Joy. Grazing Incidence Optics for X-ray Interferometry. In *X-Ray Optics, Instruments, and Missions III*, volume 4012 of *Proceedings of the SPIE*, pages 456–466, July 2000. Provided by the NASA Astrophysics Data System.

[49] A. F. Shipley, W. C. Cash, K. C. Gendreau, and D. J. Gallagher. Maxim Interferometer Tolerances and Tradeoffs. In *X-Ray and Gamma-Ray Telescopes and Instruments for Astronomy*, volume 4851 of *Proceedings of the SPIE*, pages 568–577, March 2003. Provided by the NASA Astrophysics Data System.

[50] C. A. Beichman, N. J. Woolf, and C. A. Lindensmith. *The Terrestrial Planet Finder (TPF): a NASA Origins Program to Search for Habitable Planets.* JPL publication 99-003. National Aeronautics and Space Administration ; Jet Propulsion Laboratory, California Institute of Technology, Washington, District of Columbia, May 1999.

[51] K. C. Gendreau, W. C. Cash, A. F. Shipley, and N. White. Maxim Pathfinder X-Ray Interferometry Mission. In *X-Ray and Gamma-Ray Telescopes and Instruments for Astronomy*, volume 4851 of *Proceedings of the SPIE*, pages 353–364, March 2003.

[52] R. S. Wilson and K. C. Howell. Trajectory Design in the Sun-Earth-Moon System Using Multiple Lunar Gravity Assists. *Journal of Spacecraft and Rockets*, 35(2):191–198, March-April 1998.

[53] A. E. Bryson. *Dynamic Optimization.* Addison-Wesley Publishing, first edition, June 1999.

[54] T. F. Coleman and Y. Li. On the Convergence of Reflective Newton Methods for Large-Scale Nonlinear Minimization Subject to Bounds. *Mathematical Programming*, 67(2):189–224, 1994.

[55] T. F. Coleman and Y. Li. An Interior Trust Region Approach for Nonlinear Minimization Subject to Bounds. *SIAM Journal on Optimization*, 6:418–445, 1996.

[56] R. W. Farquhar. The Flight of ISEE-3/ICE - Origins, Mission History, and a Legacy. In *AIAA/AAS Astrodynamics Specialist Conference and Exhibit*, Boston, Massachusetts, August 1998. AIAA Paper 98-4464.

[57] L. D. Millard and D. C. Hyland. Symplifying Control of Interferometric Imaging Satellite Formations: Benefits of Novel Optical Architechtures. In *Proceedings of the AAS/AIAA Astrodynamics Specialists Conference*, Big Sky, Montana, August 2003. AAS Paper No. 03-547.

VITA

VITA

Belinda Marchand Power was born in San Juan, Puerto Rico on June 10, 1974 to Yolanda Power Garcia and Carlos Marchand Rosado. She graduated from University Gardens High School in May of 1992 and immediately began her undergraduate degree at Purdue University the following August. Upon completing her Bachelor of Science in Aeronanutical and Astronanutical Engineering (BSAAE) degree, in May of 1997, Belinda chose to continue her studies at Purdue University and completed a Master of Science in Aeronautical and Astronautical Engineering (MSAAE) degree in December of 2000. She then continued her graduate studies in pursuit of a Doctoral degree. Belinda will begin a post-doctoral appointment at Purdue University in the Fall of 2004 while also acting as Visiting Professor.